TÜRKİYE CUMHURİYETİ
ADANA ALPARSLAN TÜRKEŞ SCIENCE AND TECHNOLOGY UNIVERSITY

GRADUATE SCHOOL
MECHANICAL ENGINEERING DEPARTMENT

DYNAMIC BEHAVIOR OF HEMP BASED COMPOSITE STRUCTURES

AYKUT ÇETİN

Ph.D.

ADANA 2025

TÜRKİYE CUMHURİYETİ
ADANA ALPARSLAN TÜRKEŞ SCIENCE AND TECHNOLOGY UNIVERSITY

GRADUATE SCHOOL
MECHANICAL ENGINEERING DEPARTMENT

DYNAMIC BEHAVIOR OF HEMP BASED COMPOSITE STRUCTURES

AYKUT ÇETİN

Ph.D.

THESIS ADVISOR
PROF. DR. HASAN KURTARAN

ADANA, 2025

CERTIFICATION OF APPROVAL

DYNAMIC BEHAVIOR OF HEMP BASED COMPOSITE STRUCTURES

This **Ph.D.** thesis, **completed under the conditions determined by the relevant regulations**, by **Aykut ÇETİN with student number** 19500103001 in **Adana Alparslan Türkeş Science and Technology University Institute of Graduate School** Mechanical Engineering **Department**, has been evaluated by the following academic committee, and approved in accordance with the relevant articles of the "Adana Alparslan Türkeş Science and Technology University Graduate Education Regulations".

Prof. Dr. Mustafa AKYOL

Institute of Graduate School Manager

Prof. Dr. Naime Filiz ÖZDİL

Head of the Department

Prof. Dr. Hasan KURTARAN

Academic Adivisor

Thesis Advisory Committee Members

Prof. Dr. Hasan KURTARAN

Adana Alparslan Türkeş Science and Technology University

Assoc. Prof. Dr. Ahmet Refah TORUN

Adana Alparslan Türkeş Science and Technology University

Assoc. Prof. Dr. Cem BOĞA

Adana Alparslan Türkeş Science and Technology University

Prof. Dr. Mustafa Kemal KÜLEKCİ

Tarsus University

Assoc. Prof. Dr. İlker SUGÖZÜ

Mersin University

Thesis Defence Date

29/07/2025

DECLARATION OF CONFORMITY

In this thesis study, which was prepared following the thesis writing rules of Adana Alparslan Türkeş Science and Technology University Institute of Graduate School, I declare that I provide all the information, documents, evaluations and results in accordance with scientific ethics and moral codes without resorting to any means or assistance that would be contrary to scientific ethics and traditions. I also declare that I refer to all of the articles I used in this study with appropriate references and accept all moral and legal consequences if a situation is found contrary to my statement regarding my work.

29/07/2025

[Signature]

Aykut ÇETİN

ÖZET

KENEVİR ESASLI KOMPOZİT YAPILARIN DİNAMİK DAVRANIŞI

Aykut ÇETİN
Doktora, Makine Mühendisliği Anabilim Dalı
Danışman: Prof. Dr. Hasan KURTARAN
Temmuz 2025, 151 sayfa

Bu çalışmada, kenevir esaslı lamine kompozit yapıların serbest titreşim davranışı hem nümerik modelleme hem de deneysel olarak araştırılmıştır. Çalışma, iki temel yapısal formu içermektedir: eğri kompozit kirişler ve lamine dikdörtgen plakalar. Çalışmanın temel amacı, saf ve hibrit kenevir elyaf takviyeli kompozitlerin dinamik performansını değerlendirmek ve kenevir elyaflarının, özellikle cam elyaf olmak üzere, geleneksel sentetik takviyelere sürdürülebilir bir alternatif olarak uygulanabilirliğini değerlendirmektir. Eğri kirişler ve lamine plakaların serbest titreşimine ait temel denklemler, Birinci Mertebe Kesme Deformasyon Teorisi (FSDT) çerçevesinde sanal iş ilkesi kullanılarak türetilmiştir. Büyük genlikli titreşim gösteren lamine plakalar için denklemler, doğrusal olmayan Green-Lagrange gerinim ifadelerine dayalı olarak formüle edilmiştir. Titreşim denklemlerindeki mekânsal türevler, Genelleştirilmiş Diferansiyel Kareleme (GDQ) yöntemiyle hesaplanmıştır. Mekanik özellikleri belirlemek amacıyla, kenevir, karbon ve cam lifi ile takviye edilmiş lamine numunelere tek eksenli çekme testleri uygulanmıştır. Çekme ve titreşim testi numuneleri, Vakum Destekli Reçine Transfer Kalıplama (VARTM) yöntemi kullanılarak üretilmiştir. Birinci mod doğal frekansları ve sönüm oranları, dokuz farklı kompozit kiriş için bir titreşim test düzeneği kullanılarak deneysel olarak ölçülmüştür. Geliştirilen nümerik modeller, deneysel veriler ve literatürdeki mevcut sonuçlarla karşılaştırılarak doğrulanmış; yüksek uyum göstermiş ve modellerin doğruluğu ile güvenilirliğini kanıtlamıştır. Doğrulama sonrasında, eğrilik oranı, boy/en oranı, tabaka dizilimi, sınır şartları ve hibrit lif konfigürasyonlarının doğal frekans üzerindeki etkisini incelemek üzere parametrik bir çalışma gerçekleştirilmiştir. Deneysel ve nümerik bulgular, doğal frekans performansı açısından en yüksek değerin saf karbon kompozitte elde edildiğini göstermiştir. Saf karbon kompozitleri takiben, belirli karbon/kenevir hibrit konfigürasyonları, karbon/cam hibrit konfigürasyonlarından daha yüksek doğal frekans

değerleri sergilemiştir. CHHHC (C: karbon, H: kenevir) ve CHCHC gibi tabaka dizilimleri, sınır şartlarından bağımsız olarak farklı konfigürasyonlarda karbon/cam hibritlerinden daha yüksek frekans değerleri göstermiştir. Genel olarak sonuçlar, dikkatli şekilde tasarlanmış kenevir esaslı hibrit laminatların yapısal uygulamalar için umut vadeden doğal frekans değerleri sunduğunu ortaya koymaktadır.

Anahtar Kelimeler: Doğrusal olmayan titreşim, genelleştirilmiş diferansiyel kareleme yöntemi, kenevir lifi, lamine eğri kirişler, lamine kompozit levha.

ABSTRACT

DYNAMIC BEHAVIOR OF HEMP BASED COMPOSITE STRUCTURES

Aykut ÇETİN
Ph.D., Department of Mechanical Engineering

Supervisor: Prof. Dr. Hasan KURTARAN
July 2025, 151 pages

This study investigated the free vibration behavior of hemp-based laminated composite structures through both numerical modeling and experimental investigation. The study includes two primary structural forms: curved composite beams and laminated rectangular plates. The main objective of the study was to assess the dynamic performance of pure and hybrid hemp fiber-reinforced composites and to evaluate the viability of hemp fibers as a sustainable alternative to conventional synthetic reinforcements, particularly glass fiber. The governing equations for the free vibration of curved beams and laminated plates were derived using the principle of virtual work within the framework of First-Order Shear Deformation Theory (FSDT). For laminated plates exhibiting large-amplitude vibrations, the equations were formulated based on nonlinear Green-Lagrange strain measures. Spatial derivatives in the vibration equations were computed using the Generalized Differential Quadrature (GDQ) method. To determine the mechanical properties, tensile tests were conducted on laminates reinforced with hemp, carbon, and glass fibers. Tensile and vibration test specimens were manufactured using the Vacuum-Assisted Resin Transfer Molding (VARTM) technique. First-mode natural frequencies and damping ratios were measured experimentally using a vibration test setup for nine different composite beams. The developed numerical models were validated through experimental testing and comparison with existing literature, showing a high degree of agreement and confirming the models' accuracy and reliability. After validation, a series of parametric studies was conducted to investigate the influence of curvature ratio, aspect ratio, stacking sequence, boundary conditions, and hybrid fiber configurations on the natural frequencies. The experimental and numerical findings revealed that, in terms of natural frequency performance, the pure carbon composite indicated the highest value. After pure carbon composites, a certain configuration of the carbon/hemp hybrid composites exhibited the highest natural frequency values, higher than the carbon/glass counterpart. CHHHC (C: carbon, H: hemp) and CHCHC stacking sequences consistently indicated higher frequency values than carbon/glass hybrid composites in various configurations, regardless of the boundary conditions. Overall, the results confirm that carefully configured hemp-based hybrid laminates offer promising frequency values for structural applications.

Keywords: Generalized differential quadrature method, hemp fiber, laminated composite plate, laminated curved beams, nonlinear vibration.

Dedication

To my precious family and my future wife Şule YÜCE.

ACKNOWLEDGEMENTS

First and foremost, I would like to express my deepest gratitude to my supervisor, Prof. Dr. Hasan KURTARAN, for his invaluable guidance, constructive feedback, and devoted intellectual support throughout my doctoral journey. His mentorship has been instrumental in broadening my academic vision and nurturing my passion for scientific inquiry. I am sincerely grateful for his trust and continuous encouragement at every stage of this study.

I would also like to extend my heartfelt thanks to Prof. Dr. Ahmet Sinan ÖKTEM and Assoc. Prof. Dr. Turaç FARSADİ, esteemed members of my thesis monitoring committee, for their constructive criticisms and insightful suggestions that significantly improved the quality and depth of my research.

My sincere appreciation goes to Assoc. Prof. Dr. Ahmet Refah TORUN for his unwavering support and guidance at every step of this academic journey, and to Assoc. Prof. Dr. Cem BOĞA for always being there to help and support me whenever I needed it.

I am profoundly thankful to my family for their endless love, patience, and encouragement. Their belief in me and their moral support have been the foundation of my perseverance and motivation throughout the years. They have always stood by my side in every challenge and every success.

I would also like to express my affection and gratitude to my beloved niece, Gökçe ÇETİN, who has brought so much joy and happiness into our lives since 2019. Her energy and smiles have been a constant source of joy during this demanding process.

And finally, I extend my deepest love and appreciation to Şule YÜCE, who has brought profound meaning and joy into my life. As the person who will be my future wife, her presence has been my greatest motivation and emotional support during the most intense periods of this thesis. She is the one who, for the first time, made me feel truly complete. I am truly grateful to walk this journey with her by my side.

TABLE OF CONTENTS

LIST OF FIGURES

LIST OF TABLES

LIST OF ABBREVIATIONS

NFRC	: Natural Fiber-Reinforced Composite
HFRC	: Hemp Fiber-Reinforced Composite
FEM	: Finite Element Method
GDQ	: Generalized Differential Quadrature
VARTM	: Vacuum-Assisted Resin Transfer Molding
RTM	: Resin Transfer Molding
FSDT	: First-Order Shear Deformation Theory
NFRHC	: Natural Fiber-Reinforced Hybrid Composite
DQM	: Differential Quadrature Method
DQ	: Differential Quadrature
FML	: Fiber Metal Laminated
HL	: Hand Layup
FFT	: Fast Fourier Transform

LIST OF SYMBOLS

u	: Displacement in x direction
v	: Displacement in y direction
w	: Displacement in z direction
θ_x	: Rotation around y axis
θ_y	: Rotation around x axis
E_1	: Longitudinal elastic modulus
E_2	: Transverse elastic modulus
v_{12}	: Poisson's ratio
G_{12}	: Shear modulus
ρ	: Density
ω_D	: Damped natural frequency
ω_n	: Undamped natural frequency
a / R	: Curvature ratio
a / b	: Aspect ratio
ω_L	: Linear natural frequency
ω_{NL}	: Nonlinear natural frequency
ω_{NL} / ω_L	: Frequency Ratio
$w_{\max} / h$	: Dimensionless amplitude

1. INTRODUCTION

Composite materials have become essential in modern engineering applications due to their high strength-to-weight ratio, stiffness, superior fatigue properties, resistance to corrosion, and design flexibility. Their design flexibility, through control of fiber orientation, stacking sequence, and hybrid configurations, makes them highly suitable for aerospace, automotive, marine, and structural engineering applications. Traditionally, synthetic fibers such as carbon, glass, and aramid have been the primary reinforcements due to their superior mechanical characteristics in composite structures. However, the high energy requirements during manufacturing, recycling challenges, and environmental impact of synthetic reinforcements have raised concerns regarding the long-term sustainability of these materials. In this context, natural fiber-reinforced composites (NFRCs) have emerged as a promising alternative due to their eco-friendly characteristics, biodegradability, low cost, lightweight nature, and adequate mechanical performance. Among the various plant-based fibers, hemp fiber has gained attention as a promising candidate owing to its fast growth cycle, high cellulose content, and comparatively high mechanical properties relative to other natural fibers. There are numerous studies in the literature investigating the mechanical properties of the NFRC and hemp fiber-reinforced composites (HFRCs). The dynamic performance of hemp fiber-reinforced laminates, especially their behavior under vibrational loading, has not been extensively studied in the existing literature. In practical applications, laminated composite components are frequently subjected to dynamic conditions where vibrations significantly impact fatigue life, serviceability, and acoustic performance. From a structural dynamics perspective, many laminated composite components, such as wings, hulls, blades, and curved frames, are frequently exposed to dynamic loading, operational vibrations, and external excitations. A thorough understanding of their free vibration behavior, including natural frequencies, is crucial for the optimization of design and the prevention of failure. Although the free vibration behavior of laminated composite plates and beams has been extensively studied, the majority of this research concentrates on synthetic fiber-reinforced composite structures. Moreover, curved geometries, which naturally present additional modeling and analytical challenges, are frequently simplified or overlooked. This study aims to fill these gaps by examining the free vibration behavior of hemp fiber-reinforced laminated composite structures through a combination of numerical modeling and experimental validation.

1.1. Statement of Problem

Despite its environmental benefits, hemp fiber, like other natural fibers, has certain limitations, including lower stiffness, reduced strength, and significant variability in physical properties when compared to synthetic fibers. To overcome these limitations, a promising strategy involves combining hemp fibers with high-performance synthetic fibers, such as carbon or glass, in a hybrid laminate structure. Through this method, the mechanical deficiencies of natural fibers can be compensated for by the superior properties of synthetic fibers, resulting in a balanced composite system that combines structural efficiency with environmental sustainability. Hybridization enables improved stiffness, strength, and vibrational stability, allowing hemp fiber to be integrated into more demanding structural applications. In practical composite applications, curved beams represent one of the most complex yet frequently encountered structural forms. However, despite their significance, the vibrational characteristics of laminated composite curved beams, particularly those reinforced with natural or hybrid fibers, have not been thoroughly investigated. In addition to curved beams, laminated rectangular composite plates are also widely used as structural elements subjected to free vibration. Most studies on the dynamic behavior of such plates are based on linear assumptions, which hold only for small deformations. However, in many practical scenarios, these structures undergo large amplitude vibrations, where geometric nonlinearities have a substantial impact on their dynamic response. In these situations, nonlinear vibration analysis is crucial to accurately capture amplitude-dependent frequency variations. There are various methods for analyzing the vibrational behavior of structural components numerically. Among them, the Finite Element Method (FEM) is a widely used numerical tool for modeling composite structures. However, accurately capturing dynamic responses with FEM often necessitates a large number of elements, which increases computational cost, complicates mesh generation, and poses convergence difficulties. In contrast, the Generalized Differential Quadrature (GDQ) method offers an efficient and highly accurate alternative. It can produce reliable results with considerably fewer grid points, thereby reducing computational effort. This advantage of GDQ can be quite useful, especially in a parametric study, such as the present one, where the vibration behavior of the structure under consideration needs to be computed repeatedly.

1.2. Research Objectives

This research focuses on examining the free vibration characteristics of hemp fiber-reinforced laminated composites in two structural forms: curved beams and flat plates. The analysis covers both pure and hybrid configurations, specifically including carbon/hemp, carbon/glass, and glass/hemp systems. The specific aims of the study can be stated as follows. To develop a GDQ-based numerical model for evaluating the in-plane free vibration behavior of composite curved beams. To develop a GDQ-based numerical model to determine the linear and nonlinear (large amplitude) free vibration behavior of laminated composite plates. After validating the numerical models, to conduct parametric studies to evaluate the influence of curvature ratio, aspect ratio, stacking sequence, boundary conditions, and hybridization on vibrational behavior. To determine the potential of hemp fiber as a sustainable substitute for traditional fibers, particularly glass fiber, in vibrational applications. By addressing these objectives, the thesis aims to contribute to the ongoing efforts toward sustainable and efficient composite design, demonstrating the potential of hemp fiber in dynamically sensitive structural applications.

1.3. Research Methodology

This research adopts both experimental and numerical methodologies for the investigation of the dynamic behavior of hemp-based laminated composite structures. The research methodologies of the present study can be outlined as follows:

- Fabricating the pure composite laminates reinforced with hemp, carbon, and glass fibers using the VARTM method and determining the mechanical properties of these laminates through uniaxial tensile tests.
- Developing a GDQ-based numerical model for evaluating the in-plane free vibration behavior of composite curved beams, including the effects of hybridization, curvature ratio, stacking sequence, and boundary conditions.

- Development of a GDQ-based numerical model to determine the large amplitude (nonlinear) free vibration behavior of laminated composite plates, including the effects of hybridization, aspect ratio, stacking sequence, and boundary conditions.
- Manufacturing vibration test specimens by the VARTM method and conducting experimental vibration tests on these specimens to determine their first-mode natural frequencies and damping ratios.
- Validation of the numerical models through comparison with both benchmark literature results and experimental measurements.
- Conducting a parametric study to evaluate the influence of curvature ratio, aspect ratio, stacking sequence, boundary conditions, and hybridization on the vibrational behavior of laminated composite structures.
- Comparison and discussion of experimental and numerical results for pure and hybrid composite configurations.

1.4. Organization of the Thesis

This thesis is organized into five main chapters:

Chapter 1 provides a comprehensive introduction to the research topic, presenting the motivation, problem definition, objectives, methodological approach, and overall thesis structure.

Chapter 2 outlines the theoretical foundations and a detailed literature review, covering composite materials, manufacturing techniques of composite materials, equations of curved beams and plates for laminated structures, and the numerical methods employed in the study.

Chapter 3 details the materials, fabrication techniques, experimental testing procedures, and numerical modeling strategies, offering a complete overview of the research methodology.

Chapter 4 presents and discusses the results of both numerical simulations and experimental studies, emphasizing comparisons, physical interpretations, and the implications of parametric analyses.

Chapter 5 concludes the study by summarizing the key findings and emphasizing the original contributions of the research.

2. THEORETICAL FOUNDATIONS AND LITERATURE REVIEW

2.1. Definition and General Properties of Composite Materials

A composite is a structural material made up of two or more different components that are combined on a macroscopic level and do not dissolve into each other [1]. In composite materials, one component is called the reinforcement element, while the other, which holds the reinforcement material, is known as the matrix. Reinforcement elements can come in the form of fibers, particles, or whiskers, while matrix materials can be metals, plastics, or ceramics. The reinforcement carries the load the composite is exposed to, providing stiffness and strength to the structure. Meanwhile, the matrix binds the reinforcement elements together, transfers the load to the fibers, protects them from environmental factors, and enables the transfer of localized stress from one fiber to another [2]. It’s also important to remember that the final properties of a composite are often superior to those of its components. The concept behind composites is not new; they've been used since the earliest days of human history [3].

2.2. Classification of Composite Materials

Based on the structure of the matrix and the reinforcing fillers, composites can be classified into different categories. Depending on the type of reinforcement, they fall into four groups: particle-reinforced composites, structural composites, fiber-reinforced composites, and nanocomposites [4]. From the matrix perspective, composites are divided into three types: ceramic matrix, metal matrix, and polymer matrix composites [5], [6].

2.2.1. Based on Reinforcement Type

Particle-reinforced composites consist of a matrix, like alloys or ceramics, and the particles embedded within it. These composites are generally isotropic, as the particles are randomly distributed throughout the matrix [7]. They offer advantages such as high strength, elevated operating temperatures, and resistance to oxidation. Some examples are aluminum particles mixed into rubber, silicon carbide blended with aluminum, and the combination of gravel and sand used in concrete.

Flake reinforcements are another common type within the matrix material, with glass, mica, aluminum, and silver being typical examples. These materials offer benefits like high out-of-plane flexural modulus, good strength, and low cost. However, they can be difficult to align, and the variety of usable materials is somewhat limited.

Fiber-reinforced composites are the most widely used type [8], [9]. They offer excellent strength and stiffness and are made by reinforcing matrices with either short (discontinuous) or long (continuous) fibers. Fibers are typically anisotropic and made from materials like glass, carbon, or aramid, while matrix materials can include metals such as aluminum or ceramics like calcium-alumino-silicate. Continuous fibers are either unidirectional or woven fabric layers, and these layers are stacked at different angles to create a multidirectional structure.

Nanocomposites are materials that include components at the nanometer scale (10^{-9} m). For a material to be classified as a nanocomposite, at least one of its components must be smaller than 100 nm. While advanced composites generally contain components on the micrometer scale (10^{-6} m), nanocomposites often exhibit superior properties [10]. However, in some cases, their toughness and impact resistance can be low.

2.2.2. Based on Matrix Type

Composite materials are classified based on their matrix material into four categories: ceramic, metal, and polymer matrix composites.

As the name suggests, metal matrix composites feature a metal as the matrix material. Common matrix metals include aluminum, titanium, and magnesium, while typical reinforcement fibers are made from materials like carbon and silicon carbide. Depending on design requirements, reinforcements are added to the metal matrix to enhance or sometimes adjust certain material properties. For example, incorporating fibers like silicon carbide can increase the metal's elastic stiffness and strength while reducing its thermal expansion and both thermal and electrical conductivity. Metal matrix composites offer several advantages: using low-density metals like aluminum and titanium can result in higher specific strength, while reinforcement with fibers such as graphite, which have low thermal expansion coefficients, helps achieve low thermal expansion and retain strength at high temperatures [11].

Ceramic matrix composites have a ceramic matrix, such as alumina, calcium aluminosilicate, or alumina silicate, reinforced with fibers like carbon or silicon carbide. Their advantages include hardness, high strength, resistance to high operating temperatures, a high elastic modulus, stiffness, and low density. However, ceramics generally suffer from low fracture toughness. To overcome this drawback, they are reinforced with fibers like silicon carbide or carbon, which help improve their fracture toughness [12].

Polymer matrix composites, made from polymers like epoxy, polyester, phenolic, acrylic, urethane, or polyamide and reinforced with fine fibers such as graphite, aramid, or boron, are among the most widely used types of composites. They offer several advantages, including high strength, low cost, and ease of manufacturing. These composites are generally divided into two categories: thermosets and thermoplastics. Thermoset polymers do not melt or dissolve after curing because their chains are bonded by strong covalent links. In contrast, thermoplastics can be reshaped under high temperatures and pressure due to their weaker van der Waals-type bonds. Examples of thermosets include epoxies, phenolics, polyesters, and polyamides, while common thermoplastics include polyethylene, polyether ether ketone, polystyrene, and polyphenylene sulfide [13], [14]. Polymer matrix materials and epoxy resin will be discussed in a further section thoroughly.

2.3. Fiber Reinforcement Materials

Fiber-reinforcement materials are generally classified into two main categories: synthetic and natural fiber-reinforced materials.

2.3.1. Synthetic Fiber Reinforcement Materials

The most commonly used synthetic fiber-reinforcement materials include glass, aramid, carbon, and boron fibers [15].

Glass fiber is produced by processing an amorphous material made from a mix of sand, limestone, and other oxide compounds. Its main chemical component is silica. By controlling its chemical composition and production process, a wide variety of glass fibers can be tailored for different applications. It offers advantages such as hardness, corrosion resistance, high strength, lightweight, and low cost. Because of these properties, glass fiber is the most commonly utilized fiber type in low-cost industrial applications.

Carbon fiber, also known as graphite fiber, is lightweight and offers high specific strength, excellent chemical resistance, low thermal expansion, and strong fatigue resistance. These characteristics make it a popular choice in aerospace applications. Its mechanical properties are influenced by the atomic arrangement of carbon chains and their similarity to the graphite crystal structure. The orientation of atomic bonds along the fiber direction is carefully controlled to enhance performance. Downsides include low impact resistance, high cost, and high electrical conductivity.

Aramid fiber is made from an aromatic organic compound consisting of carbon, nitrogen, oxygen, and hydrogen. It is known for its low density, low cost, high tensile strength, and good impact resistance. However, it has poor compressive strength and can degrade when exposed to sunlight.

Boron fiber is produced through chemical vapor deposition on a tungsten wire. It features high strength, high hardness, and low density. These fibers are mostly used as reinforcements in aerospace and sporting goods. They maintain their mechanical properties at high temperatures and offer excellent toughness, fatigue resistance, and compressive performance. Due to their slow production rate, boron fibers are the most expensive among all fiber types.

2.3.2. Natural Fiber Reinforcement Materials

Among fiber-reinforced composites, natural fiber-reinforced composites (NFRCs) are gaining popularity due to their undeniable environmental benefits and ease of processing. The limited availability of petrochemical resources has inevitably pushed industries toward bio-based materials. Both raw and processed cellulose fibers, as well as other bio-based polymers, have been explored for a wide range of applications, from medical to defense sectors [16], [17]. The most significant component of natural fibers is cellulose, which is found in great abundance on Earth. NFRCs often outperform their synthetic counterparts and metal-based composites in specific properties such as toughness, flexibility, ease of processing, and environmental friendliness [18]. Their combination of lightweight and strong mechanical performance makes natural fibers particularly appealing for automotive and aerospace applications.

2.3.2.1. Types and Sources of Natural Fibers

Natural fibers are derived from plants or animals and are not synthetic or man-made. These fibers, sourced from both renewable and non-renewable materials such as palm oil, sisal, flax, jute, and hemp, have gained significant attention and are widely used in composite materials [19]. They are primarily classified based on their origin as animal-based, plant-based, or mineral-based fibers, with the different types illustrated in Figure 2.1. This study focuses specifically on plant-based natural fibers. There are six main types of plant-based natural fibers: bast fibers like jute, flax, hemp, ramie, and kenaf; leaf fibers such as pineapple, sisal, and abaca; seed fibers like cotton, kapok, and coconut; core fibers including kenaf, jute, and hemp; grass and reed fibers such as corn, wheat, and rice; and other types like wood and root fibers.

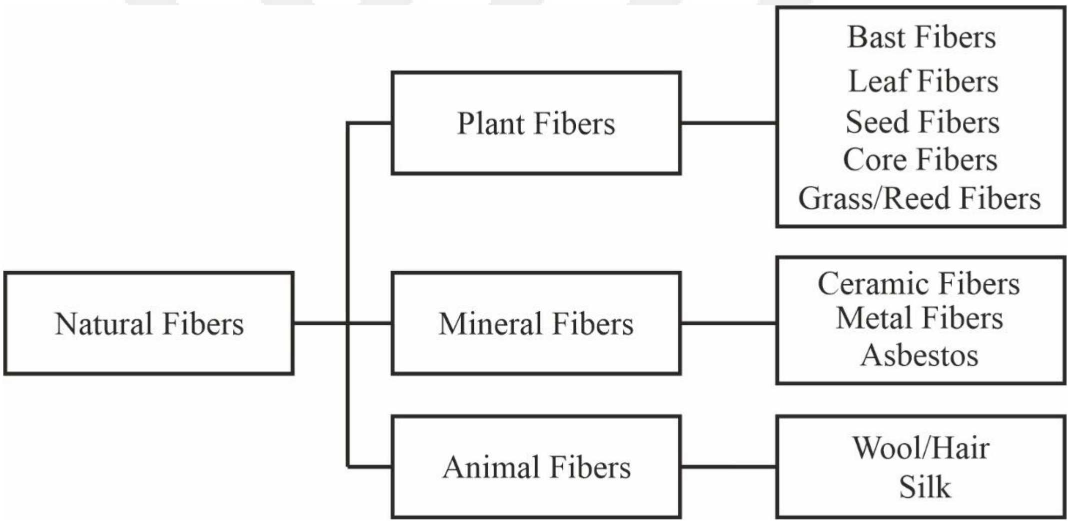

Figure 2.1. Natural fibers

Natural fibers from plants are also classified based on their intended use: primary plants are cultivated specifically for their fibers, while secondary plants produce fibers as by-products. Examples of primary fiber plants include jute, hemp, kenaf, and sisal, while pineapple, palm oil, and coconut are considered secondary sources.

2.3.2.2. *Physical and Chemical Properties of Natural Fibers*

Natural fibers can be thought of as natural composites, made up of cellulose microfibrils embedded in a lignin matrix. The primary components of these fibers are cellulose, hemicellulose, and lignin, which will be discussed in more detail in the following sections. Other constituents include pectin and waxes. Figure 2.2 provides a schematic illustration of a natural plant cell wall [20]. As shown, the microfibril structure resembles a hollow tube, and the surrounding cell wall is made up of four distinct layers. These include the primary cell wall, three secondary wall sections, and a central hollow channel within the microfibril known as the lumen.

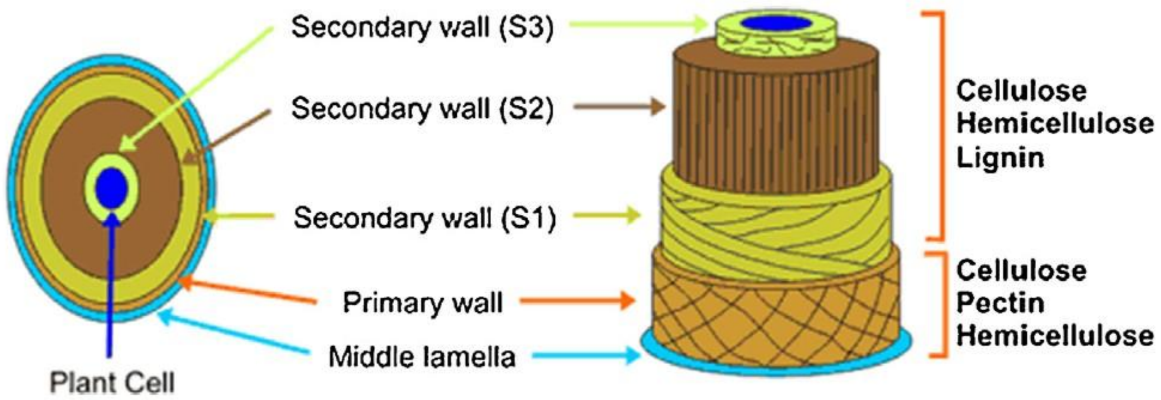

Figure 2.2. Structure of natural fibers

2.3.3. Mechanical Properties of Natural Fibers

The physical and mechanical properties of natural fibers provide essential information that must be considered before use, especially to achieve optimal performance. There have been numerous efforts to substitute synthetic fibers with natural alternatives in both structural and non-structural applications [21]. Today, many components in the automotive industry that were once made with glass fiber-reinforced composites are now being produced using natural fiber-reinforced composites. While the apparent mechanical properties of natural fibers may not match those of synthetic counterparts like glass fibers, their higher elongation at break can actually enhance the overall performance of the final composite [22]. In Table 2.1, a comparison of the mechanical properties of some common natural fibers with those of glass fiber is presented [23].

Table 2.1. Mechanical property comparison of natural fibers with glass fiber

Fiber	Density (g/cm^3)	Tensile Strength (MPa)	Young Modulus (GPa)	Elongation at break (%)
E-glass	2.5	2000-3000	70	0.5
Hemp	1.3-1.5	530-1100	45-70	2.0-4.0
Jute	1.2-1.8	325-800	10-55	1.5-2.5
Cotton	1.2-1.6	250-500	5.5-12.6	7.0-8.0
Kenaf	1.2-1.5	745-930	41-53	1.6
Ramie	1.4-1.6	500-915	23-44	1.2-3.7
Sisal	1.2-1.5	310-855	9.4-22	2.0-3.2
Flax	1.2-2.4	500-1500	27.6-80	2.3-3.2
Abaca	1.5	410-810	41	3.4

2.4. Hemp Fiber and Its Use in Composites

Hemp fibers have been utilized as a reinforcement material for more than 1000 years [24]. The low cost and continuously improving performance of technical and standard plastics have renewed interest in the utilization of hemp fibers. Currently, there is a growing focus on hemp-based composites in both industrial applications and fundamental research. These materials present a promising alternative to synthetic fibers, offering a more cost-effective and sustainable solution for reinforcement purposes [25]. Wambua et al. conducted a comparative study on the mechanical properties of polypropylene composites reinforced with sisal, kenaf, hemp, jute, coir, and glass fibers [26]. Among these, the hemp fiber-reinforced composites exhibited the highest tensile strength at 52 MPa, while the coir composites showed superior impact strength. Certain specific properties of the hemp fiber composites were found to be comparable to those of glass fiber composites. In Table 2.2, the advantages and disadvantages of hemp fiber composites are presented [27], [28], [29].

Table 2.2. Advantages and disadvantages of hemp fiber-reinforced composites

Advantages	Disadvantages
Low density, coupled with high specific stiffness and strength.	Lower durability compared to synthetic fibers, but can be significantly enhanced through various chemical and physical treatments.
Derived from renewable resources, their production typically requires relatively low energy input.	High moisture absorption which can lead to swelling and dimensional instability.
The production costs associated with natural fibers are generally lower than those of synthetic fibers.	Lower strength.
Lower health risks during the manufacturing process.	High variability in their properties, such as harvesting methods, growth condition, and maturity.
Low levels of toxic fumes when exposed to heat or incinerated at the end of their life cycle.	Less matrix options due to lower processing temperature need.
Less abrasive to processing equipment compared to synthetic fibers.	May have poor interfacial adhesion between the fiber and the matrix.
Favorable thermal and acoustic insulation properties.	Sensitive to UV, more flammable, can be microbial and sensitive to fungal attacks.

The long-term performance or durability of hemp fiber-reinforced composites remains a significant concern, particularly for outdoor applications. Environmental factors such as humidity, temperature fluctuations, and UV radiation can negatively affect their service life. Furthermore, under sustained loading conditions, hemp fiber-reinforced composites tend to exhibit greater susceptibility to creep compared to their glass fiber-reinforced counterparts. In order to overcome these disadvantages, further investigations are needed. Hybridizing hemp fiber with a suitable synthetic fiber may help mitigate these unfavorable properties and enhance the overall mechanical and durability performance of the composite. Combining synthetic and hemp fibers in composite materials has been employed to improve overall performance and mechanical properties, while also reducing moisture absorption and balancing material costs [30]. According to Sature and Mache [31], incorporating glass fibers alongside natural fibers can serve as a protective outer layer.

2.4.1. Physical and Chemical Structure of Hemp Fibers

Hemp fiber is among the strongest and stiffest natural fibers available (see Table 2.1), making it highly promising as a reinforcement material in composite applications. Hemp is a fast-growing annual crop, typically ready for harvest within approximately three months after planting. Located in the bast region of the hemp plant, these fibers exhibit specific stiffness levels that are comparable to those of glass fibers (Table 2.1) [31]. The cross-section of hemp fiber is irregular and varies along its length [32], [33]. The phloem tissue (Figure 2.3.a) contains the primary bast fibers, which are long fiber bundles extending throughout the plant stem. These fibers are composed of nearly 70–74% cellulose. Their other contents are 15–20% hemicellulose, 3.5–5.7% lignin, 0.8% pectin, and 1.2–6.2% wax [34].

Hemp fiber possesses a multi-celled structure, often described as a natural composite composed of numerous adjacent lumens (Figure 2.3.b) [33]. A typical elementary structure of a hemp fiber is illustrated in Figure 2.3.c. The fiber's cell wall is multilayered, consisting of a primary wall, formed during early cell development, and a secondary wall (S) that includes three sub-layers (S1 to S3). The elementary fibers are bonded by lignin in the middle lamella, where lignin content reaches approximately 90%. In contrast, the highest cellulose concentration, around 50%, is found in the S2 layer, which is also the thickest. Due to its high cellulose content, the S2 layer primarily governs the mechanical properties of the fiber [33], [35].

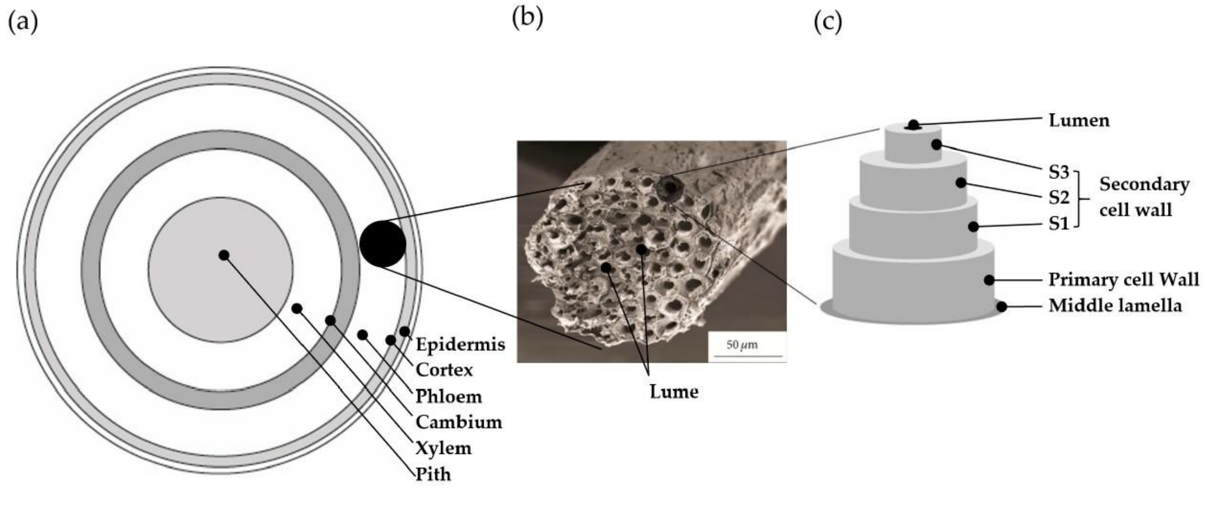

Figure 2.3. Structure of hemp fibers

The bond between hemp fibers is weakened through a microbial process known as retting. Following retting, the fibers are extracted from the hemp stem either mechanically or manually [36]. Thamae et al. [37] investigated the effects of retting conditions and duration, as well as treatments such as mercerization with NaOH and hydrothermal processing, on the tensile properties of hemp fibers. Their findings showed that both mercerization and hydrothermal treatment altered the surface morphology of the fibers, leading to improved mechanical properties, likely due to changes in their microstructural arrangement. Additionally, retting for up to three weeks had no significant impact on the tensile strength of the hemp fibers.

2.4.1.1. Cellulose

Cellulose is the primary component of natural fibers and is considered the most abundant bio-based material on Earth. Structurally, cellulose consists of two main regions: crystalline and amorphous. About 60–90% of its weight is made up of crystalline regions. In these areas, the molecular chains are tightly packed with limited hydroxyl (OH) groups available, making them less hydrophilic. In contrast, the amorphous regions have fewer hydrogen bonds between chains, leading to a higher number of OH groups that can interact with water molecules, thus increasing hydrophilicity. Figure 2.4 illustrates the chemical structure of cellulose [38].

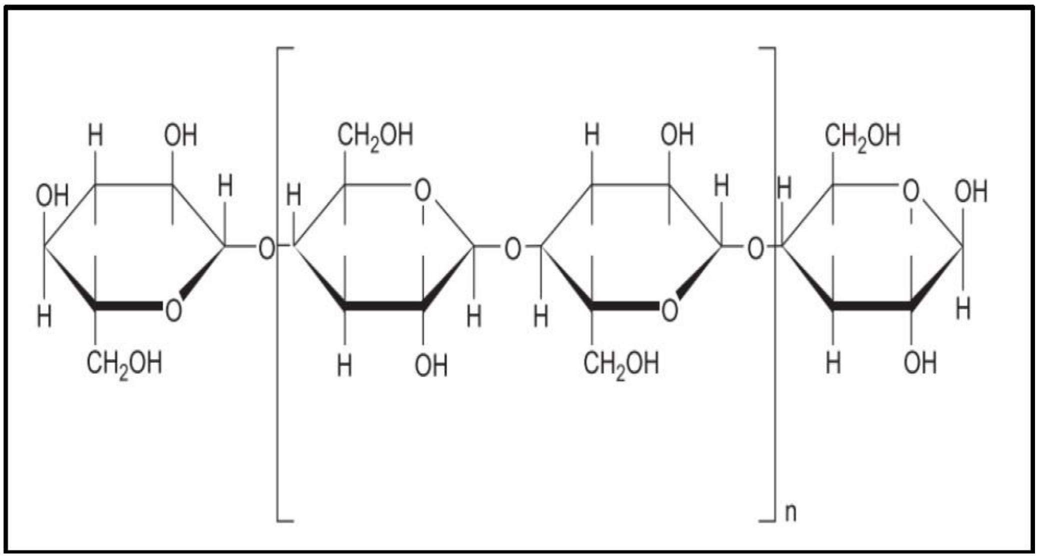

Figure 2.4. Chemical structure of cellulose

2.4.1.2. Hemicellulose

Alongside cellulose, hemicellulose is another key component of natural fibers and ranks as the second most common bio-based polymer. It has a lower molecular weight than cellulose and acts as a binding agent, filling the gaps between cellulose microfibrils. Hemicellulose is made up of a group of branched polysaccharides. Through hydrogen bonding, it attaches to cellulose to form cellulose–hemicellulose networks, which then contribute to the structural framework of the fiber cell [39]. Compared to cellulose, hemicellulose has a more amorphous structure, which allows its OH groups easier access to water molecules, thus making it more hydrophilic. The typical chemical structure of hemicellulose is illustrated in Figure 2.5 [38].

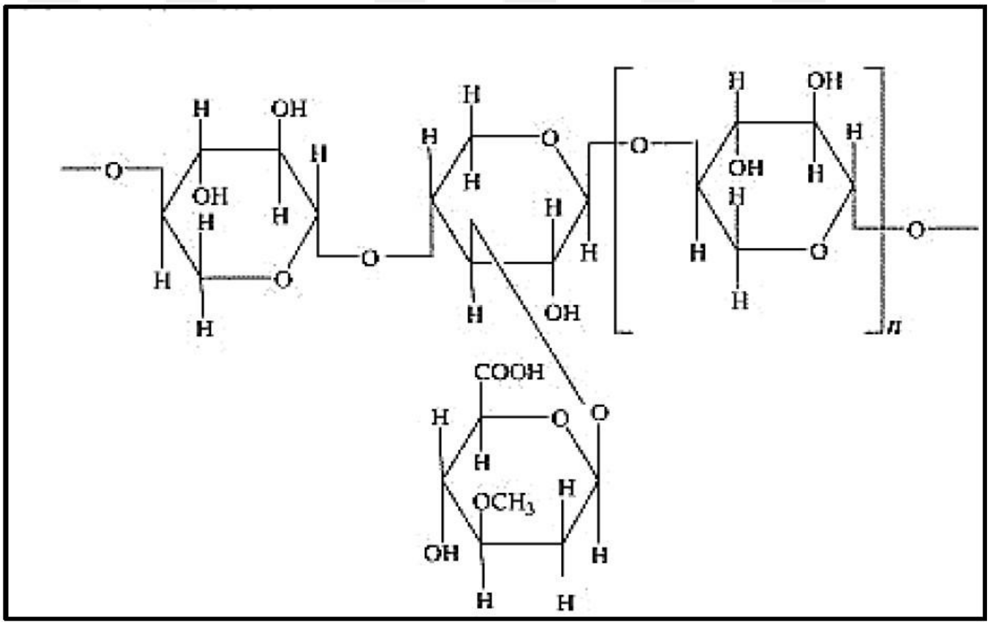

Figure 2.5. Chemical structure of hemicellulose

2.4.1.3. Lignin

Lignin is a highly branched polymer that acts as the matrix for natural fibers, allowing cellulose to be incorporated into the fiber cell along with hemicellulose. It has a complex three-dimensional structure made up of phenylpropane units. As shown in Figure 2.6, these units are linked by various carbon-carbon or ether bonds, making lignin insoluble in water and separating it into monomeric units. Lignin plays a crucial role in protecting cellulose and hemicellulose under harsh environmental conditions, such as high humidity. In addition to providing structural support to the fiber, it also shields natural fibers from UV exposure and thermal stress. However, when lignin is removed from the cell walls, fiber stiffness increases, and load transfer between the fiber and matrix becomes more efficient. While lignin is stable under thermal and UV conditions, hemicellulose is the main contributor to thermal degradation and moisture absorption in the fiber [40].

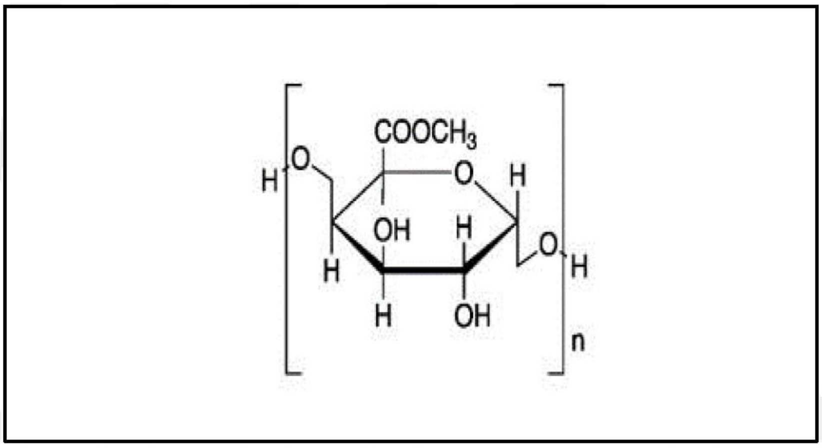

Figure 2.6. Chemical structure of lignin

2.5. Polymer Matrix Materials

The matrix in a composite material serves multiple functions, including shielding the fibers from environmental effects, maintaining their fixed alignment, transferring loads to the fibers, and defining the shape and surface finish of the composite [41]. Additionally, the matrix properties influence key performance aspects such as maximum service temperature, resistance to moisture and chemicals, and overall thermal stability. In hemp fiber composites, polymeric matrices, both thermoplastic and thermoset, are most commonly used due to their lightweight nature and low processing temperature requirements [42]. The characteristics of these polymeric matrices used with hemp fibers are summarized in Table 2.3 [43].

Table 2.3. Properties of thermoplastic and thermoset polymers used for hemp fibers

Polymer	Density (g/cm^3)	Failure Strain (%)	Tensile Strength (Mpa)	Young's Modulus (GPa)
		Thermoplastics		
PP	0.89-0.92	20-400	30-40	1.1-1.6
HDPE	0.94-0.96	2-130	14.5-38	0.4-1.5
PS	1.04-1.06	1-2.5	25-69	4-5
PLA	1.21-1.25	2.5-6	21-60	0.35-3.5
		Thermosets		
Epoxy	1.1-1.4	1-6	35-100	3-6
Polyester	1.2-1.5	4-7	40-90	2-4.5

2.5.1. Thermoplastic Matrices

Thermoplastics include both linear and branched polymers, which can be melted or softened and then re-hardened reversibly depending on temperature [44]. Since natural fibers typically possess a higher modulus than thermoplastics, combining the two can result in composites with enhanced stiffness [45]. Among the most common processing methods for hemp fiber composites are melt compounding and melt pressing. Melt compounding involves equipment such as single- or twin-screw extruders and internal melt mixers, which can be used individually or in combination. Melt pressing, on the other hand, is typically applied to loose chopped fibers or mats composed of short or long fibers. In this method, the fibers are alternately layered with the thermoplastic matrix before applying heat and pressure. Producing high-quality composites through this process depends on careful control of factors such as viscosity, pressure, holding time, and temperature, all of which must be tailored to the specific fiber and matrix used [46]. The thermoplastic matrices that have been most extensively researched include polypropylene (PP), polystyrene (PS), polyethylene (PE), and polylactic acid (PLA).

2.5.2. Thermoset Matrices

Thermoset matrices are cross-linked polymers that undergo a permanent hardening process through a chemical reaction with a secondary component, commonly referred to as a hardener or curing agent. Due to their excellent mechanical strength, dimensional stability, and resistance to chemicals, thermosets are widely utilized in advanced composite applications, including aerospace, construction, and insulation sectors [28]. Examples of thermoset matrices include vinyl esters, polyimides, epoxies, and phenolics. Frequently used hardeners include multifunctional amines, acids, and anhydrides.

Polyester and epoxy are considered the most robust thermoset matrices for reinforcing natural fibers. Their processing temperatures, typically ranging from 25 °C to over 100 °C, remain safely below the degradation threshold of hemp fibers, which begins around 150 °C [47]. As a result, thermosets offer certain advantages over thermoplastics, such as lower processing temperatures, reduced risk of thermomechanical degradation, and the ability to incorporate higher fiber content into the matrix. However, efficient recycling of thermoset composites remains a significant challenge, whereas thermoplastics offer greater flexibility in design and ease of recyclability [28].

Common processing techniques for thermoset composites include sheet molding compound (SMC), resin transfer molding (RTM), pultrusion, vacuum-assisted resin transfer molding (VARTM), and hand layup. Among these, vacuum-assisted methods are preferred for producing high-performance thermoset composites. Their key advantages include: (1) the ability to achieve high fiber content in laminates, (2) reduced void formation, and (3) enhanced fiber wet-out due to applied pressure [28], [48].

2.5.2.1. Epoxy Resin

Epoxy resins are primarily classified as thermoset polymers [49]. Typically, each epoxy molecule contains one epoxy group. These epoxy rings are highly strained, making them particularly reactive with other chemical groups, especially curing agents. The first and still the most widely used commercial epoxy resin is diglycidyl ether of bisphenol A (DGEBA), which is synthesized through a reaction between bisphenol A and epichlorohydrin in the presence of sodium hydroxide (NaOH). Figure 2.7 illustrates the typical reaction pathway for producing DGEBA [50]. Other types of epoxy resins differ mainly in the non-epoxy portion of the molecule, resulting in distinct chemical structures and, as expected, varied properties. This non-epoxy segment can be aromatic, cycloaliphatic, or aliphatic.

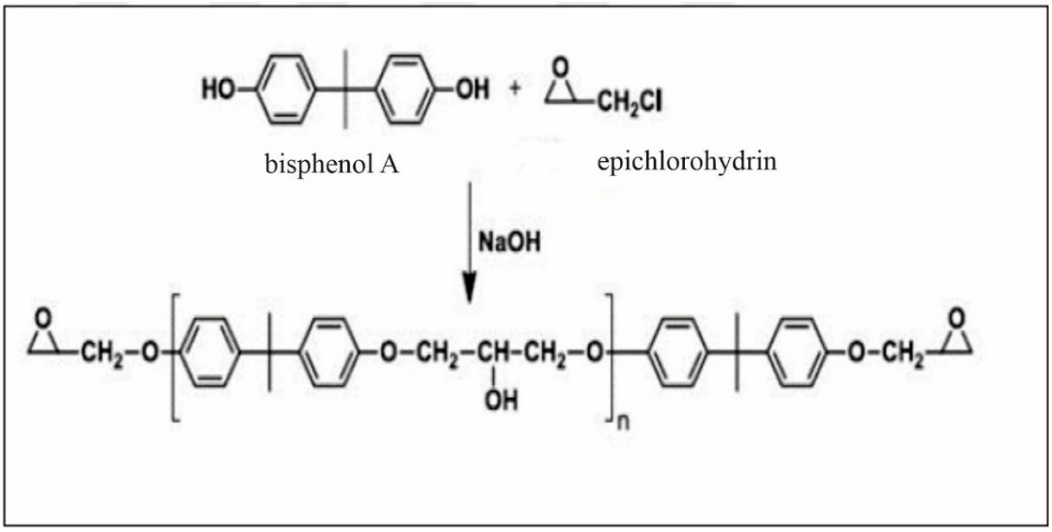

Figure 2.7. Bisphenol A and epichlorohydrin reaction

The synthesis process of the epoxy begins with reactions either between monomers or between monomers and curing agent molecules. This leads to the formation of branched structures accompanied by increasing viscosity. As the reaction progresses, a gelation phase occurs, characterized by the transformation of functional groups and the formation of a large macromolecule, which ultimately becomes the final thermoset product. During the transition to a glassy structure, the mobility of the system decreases due to the formation of covalent bonds, resulting in a shift from a gel to a glassy state. This transition is illustrated in Figure 2.8 [50].

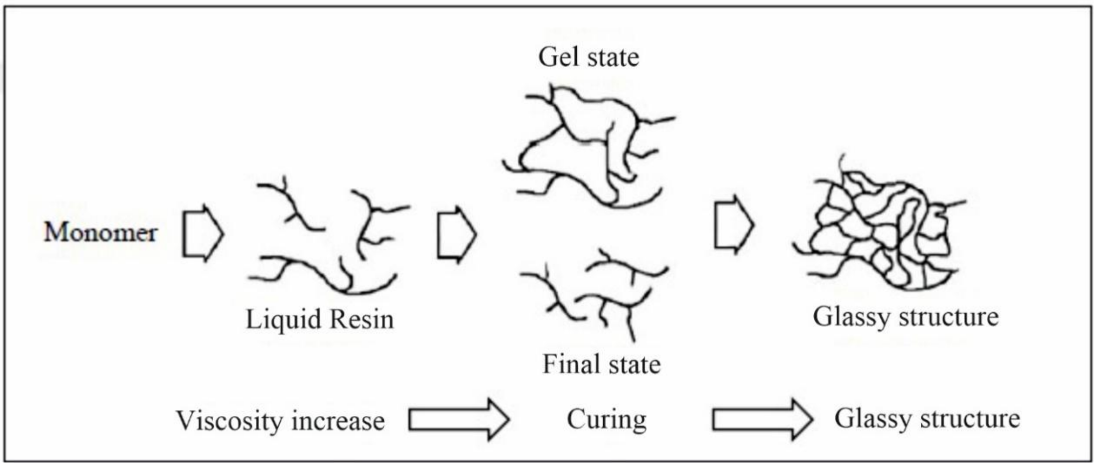

Figure 2.8. Epoxy curing prosess

Due to its excellent properties, such as, moderate cost, low shrinkage and toxicity, high strength, and compatibility with various processing techniques and applications, epoxy resin has become a primary matrix material in composite manufacturing. This thermoset matrix can be used at temperatures up to 175 °C and is generally compatible with a wide range of reinforcement materials [51].

2.6. Manufacturing Techniques for Laminated Composites

Due to the superior mechanical properties of composite materials compared to traditional materials, the manufacturing methods used to produce them are also of great importance. There are several production techniques available; the most commonly used ones are hand lay-up, vacuum bagging, filament winding, spray-up, resin transfer molding, and vacuum-assisted resin transfer molding methods.

2.6.1. Hand Lay-up Method

The hand lay-up technique is the most widely used and simplest manufacturing method for composites [52]. It involves manually placing the reinforcement material into a mold and then applying resin over it (Figure 2.9). The wet composite is then rolled or brushed to ensure even resin distribution and to eliminate air bubbles. The process is carried out repeatedly until the target thickness is reached. The hand lay-up process consists of four main steps: mold preparation, gel coating, layering (lamination), and curing. Preparing the mold is one of the most critical stages in the layering process. Depending on the number of parts to be produced, curing temperature, and pressure, molds can be made from wood, plaster, plastic, composite, or metal materials. After the mold is prepared, a gel coat is applied to give the final part a smooth surface finish. Initially, a resin layer is brushed onto the mold before adding the reinforcement. A well-mixed blend of resin and catalyst is then applied over the fibers using a brush. Curing typically takes place at room temperature, and the final part is dismounted from the mold once the process is complete [53].

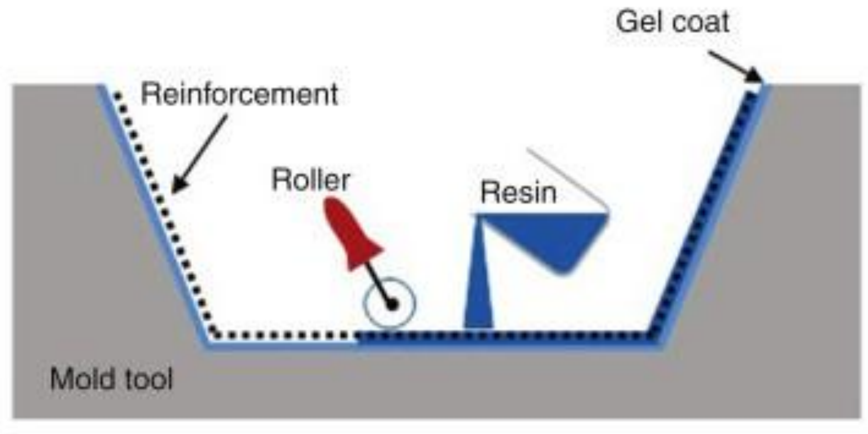

Figure 2.9. Hand layup method

2.6.2. Vacuum Bagging Method

The vacuum bagging method can be seen as an advanced version of the hand lay-up process. In this technique, after applying resin to the fibers using a brush or roller, just like in hand lay-up, the entire system is then processed under vacuum conditions (Figure 2.10). Compared to traditional hand lay-up, vacuum bagging offers several advantages: a higher fiber-to-resin ratio, fewer air bubbles, better resin penetration between fibers, and effective removal of excess resin from the system [54]. However, one downside of this method is its higher production cost. Despite this, it is especially suitable when using resins like epoxy or phenolic. The vacuum bagging process is carried out as follows:

- A mixture of resin and hardener is applied to the fibers laid on a surface using a roller or brush.
- A perforated release film is then placed over the layered structure.
- A breather fabric is added on top of the release film to help remove air bubbles and absorb excess resin.
- To isolate the resin-infused structure from the external environment, a plastic vacuum film is used along with a sealing tape.
- The vacuum process is carried out utilizing a vacuum pump, and the material is then subjected to the curing process.

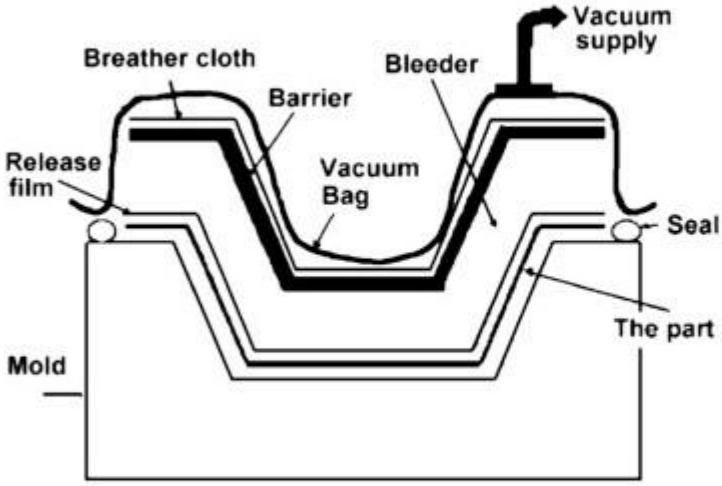

Figure 2.10. Vacuum bagging method

2.6.3. Filament Winding Method

The filament winding method involves winding resin-impregnated fibers around a rotating mandrel at specific angles (Figure 2.11) [55]. Although it's a relatively slow process, it allows partial control over the fiber orientation. Once the winding is complete, the system is cured in an oven or autoclave and then removed from the mandrel. This technique is commonly used to produce round or cylindrical objects such as pressure vessels, rockets, and industrial storage tanks.

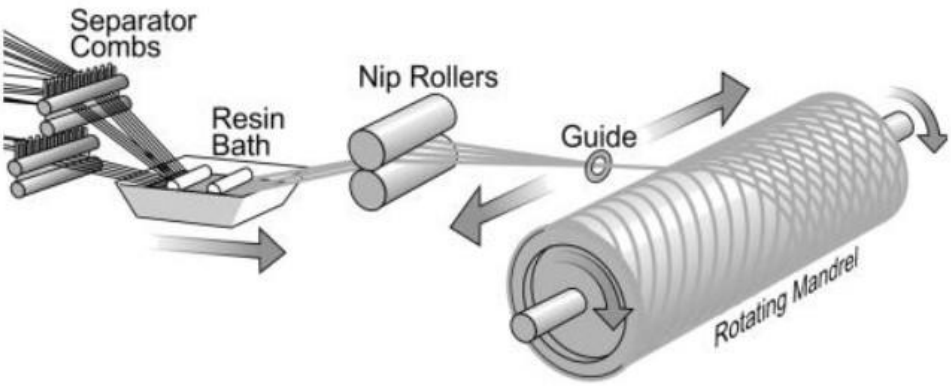

Figure 2.11. Filament winding method

2.6.4. Spray-Up Method

Similar to the hand lay-up method, the spray-up technique differs in that a mixture of chopped fibers and resin is sprayed directly into the mold using a spray gun (Figure 2.12) [56]. After spraying, a roller is used to remove any air trapped within the resin. This method offers greater ease when producing complex-shaped parts compared to traditional hand lay-up. Curing generally occurs at room temperature. While the spray-up method is cost-effective and easy to apply, its main drawback is the use of chopped fibers, which limits the composite's mechanical performance.

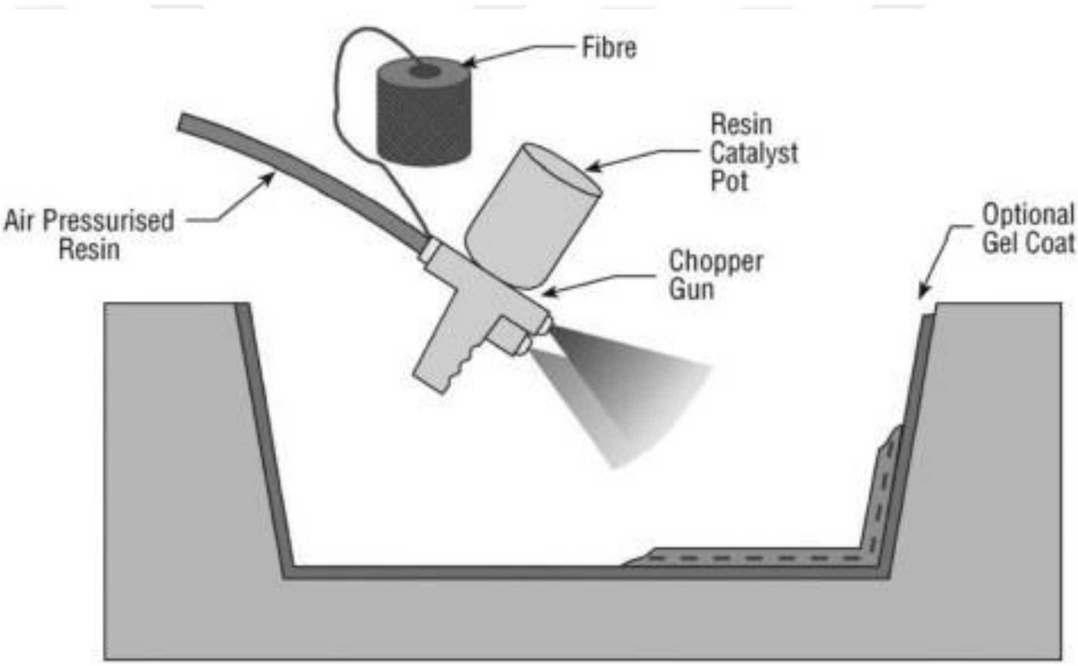

Figure 2.12. Spray up method

2.6.5. Resin Transfer Molding (RTM) Method

This method is well-suited for producing large components in medium to high production volumes. The process diagram for RTM is shown in Figure 2.13 [57]. Unlike open-mold methods, where the polymer is poured directly, RTM involves loading the resin into a reservoir while the mold is preheated. Once the layers of textile fabric are placed inside the solid mold, resin is injected to saturate the preform. To assist in pulling the resin into the mold and minimize the formation of air bubbles, vacuum assistance is often used [58].

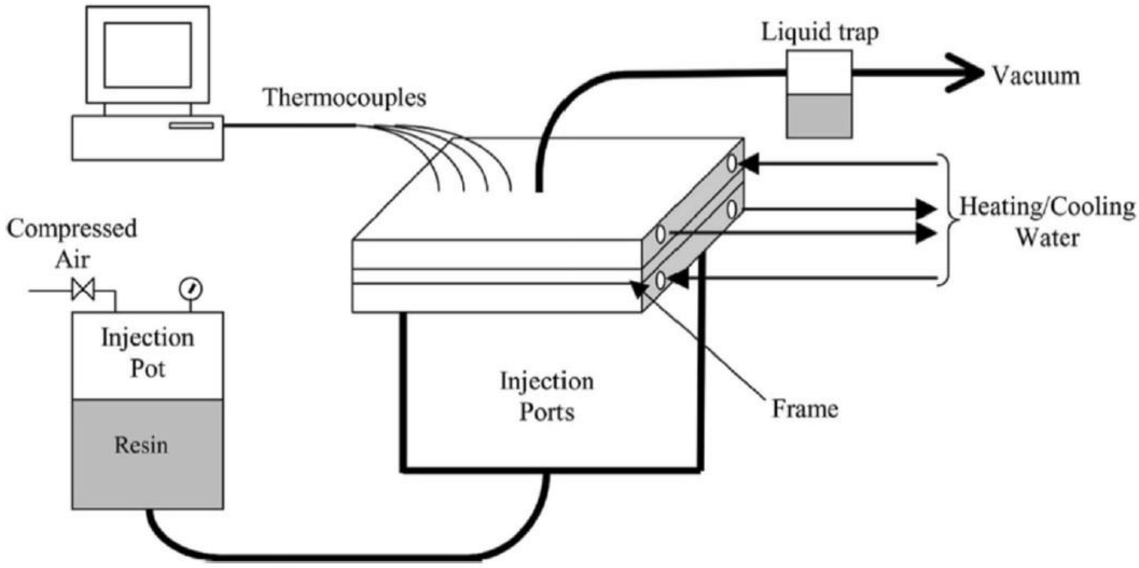

Figure 2.13. Resin transfer molding method

2.6.6. Vacuum-Assisted Resin Transfer Molding (VARTM) Method

The VARTM method is a modified version of the RTM process, where the upper mold is replaced with a vacuum bag [59]. In this method, a vacuum is used to assist resin flow while maintaining atmospheric pressure during curing. Key components used in the VARTM setup include a release fabric, flow media, spiral tubing, a vacuum bag, and sealing tape. The process begins by placing the preform material into the bottom mold, shaped to the desired dimensions. A flexible tooling surface is then pressed down over the composite part. The flow media, laid over the release fabric, helps guide and control the resin flow. Spiral tubing is used to direct the resin across the fiber preform. Liquid resin is pumped into the mold at moderate pressure, allowing it to fully wet out the fibers. To reduce air voids and improve composite quality, a vacuum is applied to the mold. A typical setup for the VARTM process is shown in Figure 2.14 [60]. This method will be presented in detail in further sections.

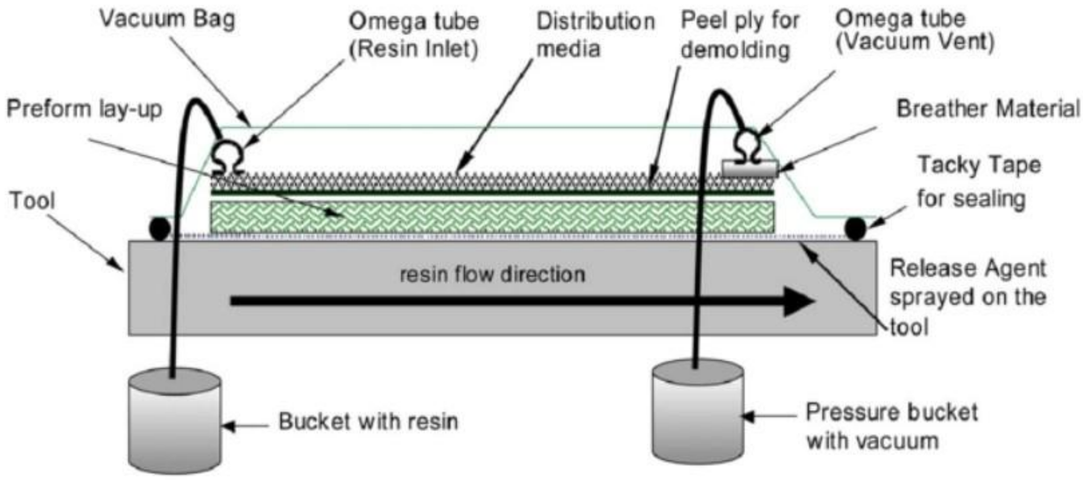

Figure 2.14. Vacuum-assisted resin transfer molding method

2.7. Laminated Composite Curved Beam Equations

2.7.1. Constitutive Equations

For small displacements and rotations, the nonlinear Green-Lagrange strain measures can be linearized. Under this assumption, only the first-order strain terms are considered, and higher-order nonlinear components, such as quadratic strain terms, are disregarded. As a result, the axial and shear strain expressions for a composite curved beam are simplified as follows:

$$\begin{aligned} \varepsilon_{11} &= e_{11} \\ \gamma_{13} &= e_{13} + e_{31} \end{aligned} \tag{2.1}$$

For a beam with constant radius of curvature *R*, and using a curvilinear coordinate system $\alpha_1, \alpha_2, \zeta$), the linearized strain components become:

$$\begin{aligned} e_{11} &= \frac{\partial u}{\partial \alpha_1} + \frac{w}{R_1} \\ e_{31} &= \frac{\partial w}{\partial \alpha_1} - \frac{u}{R_1} \\ e_{13} &= \frac{\partial u}{\partial \zeta} \end{aligned} \tag{2.2}$$

where u and w denote the displacements in the axial α_1 and radial ζ directions, respectively. And the parameter *R* is the principal radius of curvature in the $\alpha_1 - \zeta$ plane.

Thereafter, for simplicity in notation, the curvilinear coordinate system ($\alpha_1, \alpha_2, \zeta$) is renamed as *x, y, z* and radius of curvature (R_1) is written as *R*. Geometric parameters of the laminated curved beam are presented in Figure 2.15.

In a curved beam, the displacements at a general point (*x*, *z*) at time *t* can be expressed in terms of the mid-plane displacements and rotation as follows:

$$\begin{aligned} u(x,z,t) &= u_0(x,t) + z\theta_x(x,t) \\ w(x,z,t) &= w_0(x,t) \end{aligned} \tag{2.3}$$

where u_0 and w_0 are mid-plane displacements and θ_x is the rotation about *y* axis.

By substituting the linear strain definitions into the displacement field, the resulting expressions for axial and shear strains are obtained as follows:

$$\begin{aligned} \varepsilon_x &= \varepsilon_1 + z\varepsilon_2 \\ \gamma_{zx} &= \varepsilon_{s1} \end{aligned} \tag{2.4}$$

The relevant strain terms are defined as:

$$\begin{aligned} \varepsilon_1 &= \left(\frac{\partial u_0}{\partial x} + \frac{w_0}{R} \right) \\ \varepsilon_2 &= \frac{\partial \theta_x}{\partial_x} \\ \varepsilon_{s1} &= \theta_x \end{aligned} \tag{2.5}$$

The linear constitutive relationship for a laminated composite curved beam is formulated in terms of the in-plane force resultants and their corresponding strain components as follows:

$$N = \begin{Bmatrix} N_1 \\ N_2 \end{Bmatrix} = \begin{bmatrix} A_1 & A_2 \\ B_1 & B_2 \end{bmatrix} \begin{Bmatrix} \varepsilon_1 \\ \varepsilon_2 \end{Bmatrix} = A_{mat}\varepsilon \tag{2.6}$$

The transverse shear force resultant is expressed as:

$$Q_1 = A_{s1}\varepsilon_{s1} = A_{smat}\varepsilon_s \tag{2.7}$$

In this context, A_i, B_i, and A_{s1} represent the laminate's extensional, bending-extensional coupling, and shear stiffness coefficients, respectively. These stiffness parameters are calculated by integrating through the thickness of the beam, as shown below:

$$\begin{aligned}
\{A_1, A_2\} &= \sum_{k=1}^{n}\int_{z_{k-1}}^{z_k} E_x^k \{1, z\} dz \\
\{B_1, B_2\} &= \sum_{k=1}^{n}\int_{z_{k-1}}^{z_k} E_x^k \{z, z^2\} dz \\
\{A_{s1}\} &= \sum_{k=1}^{n} k_s \int_{z_{k-1}}^{z_k} b\bar{Q}_{55}^{(k)} dz
\end{aligned} \tag{2.8}$$

where $E_x^{(k)}$ is the equivalent elastic modulus for the *k*-th lamina, $\bar{Q}_{55}^{(k)}$ is the transverse shear modulus, and $k_s = 5/6$ is the shear correction factor. Readers can visit [61].

$$\frac{1}{E_x^k} = \frac{\cos^4(\theta_k)}{E_{11}} + \frac{\sin^4(\theta_k)}{E_{22}} + \left(\frac{1}{G_{12}} - \frac{2\nu_{12}}{E_{11}}\right)\cos^2(\theta_k)\sin^2(\theta_k) \tag{2.9}$$

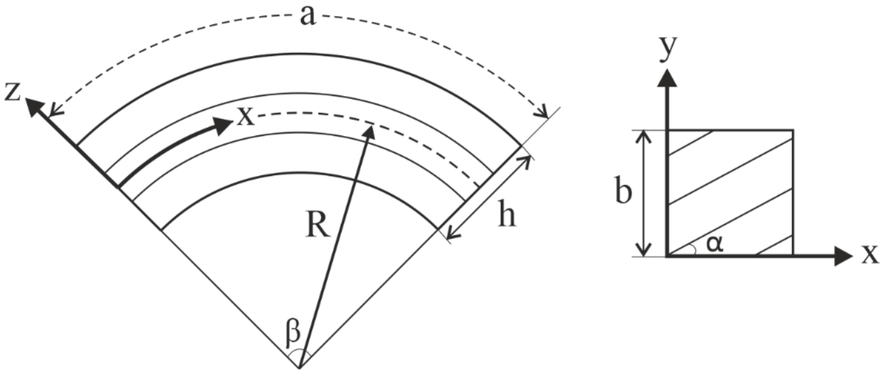

Figure 2.15. Geometric parameters of the laminated curved beam

2.7.2. Equation of Motion

The principle of virtual work is utilized to derive the equations of motion for a laminated composite curved beam. Under the assumptions of small displacements and rotations, and in the absence of external forces, the internal virtual work must equal the virtual variation of kinetic energy:

$$\sum_{k=1}^{L}\int_{z_{k-1}}^{z_k}\int_X\left[\sigma_x^{(k)}(\delta\varepsilon_1+z\delta\varepsilon_2)+k_s\tau_{zx}^{(k)}\delta\theta_x+(\rho^{(k)}\ddot{u}_0+\rho^{(k)}z\ddot{\theta}_x)\delta u_0+\rho^{(k)}\ddot{w}_0\delta w_0\right]dxdz=0 \tag{2.10}$$

In this expression, ε_1 and ε_2 denote the axial and curvature-induced strains, respectively, while θ_x represents the cross-sectional rotation. The kinetic energy terms incorporate both translational and rotational inertia effects of each individual lamina.

To express the inertial terms in a compact form, the following cross-sectional inertia integrals are defined:

$$\begin{aligned} I_0 &= \sum_{k=1}^{n}\int_{z_{k-1}}^{z_k}\rho^{(k)}dz \\ I_1 &= \sum_{k=1}^{n}\int_{z_{k-1}}^{z_k}\rho^{(k)}zdz \\ I_2 &= \sum_{k=1}^{n}\int_{z_{k-1}}^{z_k}\rho^{(k)}z^2dz \end{aligned} \tag{2.11}$$

The coupling inertia term I_1 vanishes for symmetric laminates.

The internal force resultants are related to the linear strain components through the following relationship:

$$\int_X\left[N_1\delta\varepsilon_1+N_2\delta\varepsilon_2+Q_1\delta\theta_x+I_0\ddot{u}_0\delta u_0+I_2\ddot{\theta}_x\delta\theta_x+I_0\ddot{w}_0\delta w_0\right]dx=0 \tag{2.12}$$

The expressions for the force resultants N_1, N_2, and Q_1 are directly derived from the constitutive relations in Equation (2.6).

2.8. Laminated Composite Plate Equations

2.8.1. Constitutive Equations

The general layout of a rectangular laminated composite plate of length *a*, width *b*, and thickness *h* can be shown as in Figure 2.16. The mid-surface of the plate is represented by the $z = 0$ plane. When the plate is subjected to external loads, displacements at a general point (*x*, *y*, *z*) at a time *t* can be expressed in the *x*, *y* and *z* directions as follows:

$$
\begin{aligned}
u(x,y,z,t) &= u_0(x,y,t) + z\theta_x(x,y,t) \\
v(x,y,z,t) &= v_0(x,y,t) + z\theta_y(x,y,t) \\
w(x,y,z,t) &= w_0(x,y,t)
\end{aligned}
\qquad (2.13)
$$

where u_0, v_0, and w_0 indicate mid-plane displacements in *x*, *y*, and *z* axis respectively. θ_x and θ_y denote rotations around *y* and *x* axes, respectively.

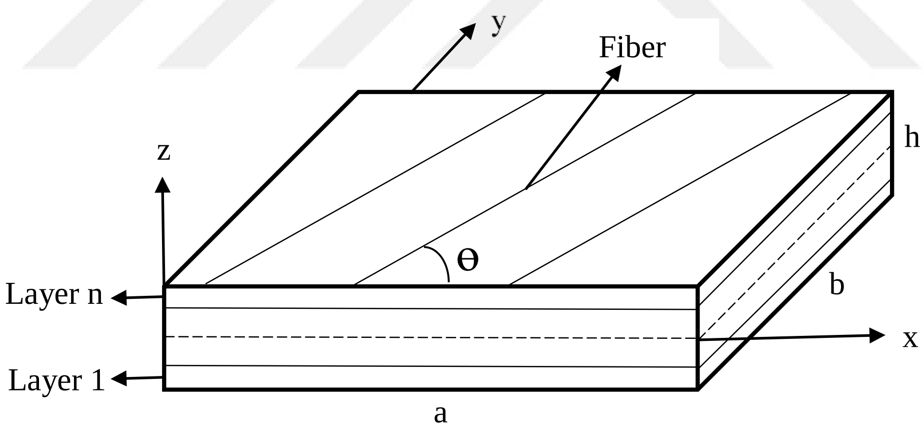

Figure 2.16. Geometric parameters of the laminated composite plate

When external loads are high or the plate is thin, large displacements occur in the plate. In the case of large displacements, in-plane displacements can be stated using Green-Lagrange nonlinear strain-displacement relationships, as follows [61], [62]. Green-Lagrange nonlinear strain-displacement relationships with the corresponding scale factors can be stated as follows:

$$\varepsilon_{ij} = \frac{\lambda_{ij}}{h_i h_j} \tag{2.14}$$

The strain-displacement relationship for shell structures, incorporating nonlinear terms without any simplifications, is given below [62]:

$$\begin{aligned}\lambda_{xx} &= h_x \frac{\partial u}{\partial x} + \frac{h_x v}{h_y}\frac{\partial h_x}{\partial y} + \frac{h_x w}{h_z}\frac{\partial h_x}{\partial z} + \frac{1}{2}\left(\frac{\partial u}{\partial x} + \frac{v}{h_y}\frac{\partial h_x}{\partial y} + \frac{w}{h_z}\frac{\partial h_x}{\partial z}\right)^2 \\ &+ \frac{1}{2}\left(\frac{\partial v}{\partial x} - \frac{u}{h_y}\frac{\partial h_x}{\partial y}\right)^2 + \frac{1}{2}\left(\frac{\partial w}{\partial x} - \frac{u}{h_z}\frac{\partial h_x}{\partial z}\right)^2\end{aligned} \tag{2.15}$$

$$\begin{aligned}\lambda_{yy} &= h_y \frac{\partial v}{\partial y} + \frac{h_y w}{h_z}\frac{\partial h_y}{\partial z} + \frac{h_y u}{h_x}\frac{\partial h_y}{\partial x} + \frac{1}{2}\left(\frac{\partial v}{\partial y} + \frac{w}{h_z}\frac{\partial h_y}{\partial z} + \frac{u}{h_x}\frac{\partial h_y}{\partial x}\right)^2 \\ &+ \frac{1}{2}\left(\frac{\partial w}{\partial y} - \frac{v}{h_z}\frac{\partial h_y}{\partial z}\right)^2 + \frac{1}{2}\left(\frac{\partial u}{\partial y} - \frac{v}{h_x}\frac{\partial h_y}{\partial x}\right)^2\end{aligned} \tag{2.16}$$

$$\begin{aligned}\lambda_{xy} &= \frac{1}{2}\left(h_x \frac{\partial u}{\partial y} + h_y \frac{\partial v}{\partial x} - v\frac{\partial h_y}{\partial x} - u\frac{\partial h_x}{\partial y}\right) \\ &+ \frac{1}{2}\left(\frac{\partial u}{\partial y} - \frac{v}{h_x}\frac{\partial h_y}{\partial x}\right)\left(\frac{\partial u}{\partial x} + \frac{v}{h_y}\frac{\partial h_x}{\partial y} + \frac{w}{h_z}\frac{\partial h_x}{\partial z}\right) \\ &+ \frac{1}{2}\left(\frac{\partial v}{\partial x} - \frac{u}{h_y}\frac{\partial h_x}{\partial y}\right)\left(\frac{\partial v}{\partial y} + \frac{u}{h_x}\frac{\partial h_y}{\partial x} + \frac{w}{h_z}\frac{\partial h_y}{\partial z}\right) \\ &+ \frac{1}{2}\left(\frac{\partial w}{\partial x} - \frac{u}{h_z}\frac{\partial h_x}{\partial z}\right)\left(\frac{\partial w}{\partial y} - \frac{v}{h_z}\frac{\partial h_y}{\partial z}\right)\end{aligned} \tag{2.17}$$

$$\lambda_{yz} = \frac{1}{2}\left(h_z \frac{\partial w}{\partial y} + h_y \frac{\partial v}{\partial z} - v\frac{\partial h_y}{\partial z} - w\frac{\partial h_z}{\partial y} \right)$$
$$+\frac{1}{2}\left(\frac{\partial v}{\partial z} - \frac{w}{h_y}\frac{\partial h_z}{\partial y} \right)\left(\frac{\partial v}{\partial y} + \frac{w}{h_z}\frac{\partial h_y}{\partial z} + \frac{u}{h_x}\frac{\partial h_y}{\partial x} \right)$$
$$+\frac{1}{2}\left(\frac{\partial w}{\partial y} - \frac{v}{h_z}\frac{\partial h_y}{\partial z} \right)\left(\frac{\partial w}{\partial z} + \frac{v}{h_y}\frac{\partial h_z}{\partial y} + \frac{u}{h_x}\frac{\partial h_z}{\partial x} \right) \tag{2.18}$$
$$+\frac{1}{2}\left(\frac{\partial u}{\partial y} - \frac{v}{h_x}\frac{\partial h_y}{\partial x} \right)\left(\frac{\partial u}{\partial z} - \frac{w}{h_x}\frac{\partial h_z}{\partial x} \right)$$

$$\lambda_{zx} = \frac{1}{2}\left(h_z \frac{\partial w}{\partial x} + h_x \frac{\partial u}{\partial z} - u\frac{\partial h_x}{\partial z} - w\frac{\partial h_z}{\partial x} \right)$$
$$+\frac{1}{2}\left(\frac{\partial u}{\partial z} - \frac{w}{h_x}\frac{\partial h_z}{\partial x} \right)\left(\frac{\partial u}{\partial x} + \frac{w}{h_z}\frac{\partial h_x}{\partial z} + \frac{v}{h_y}\frac{\partial h_x}{\partial y} \right)$$
$$+\frac{1}{2}\left(\frac{\partial w}{\partial x} - \frac{u}{h_z}\frac{\partial h_x}{\partial z} \right)\left(\frac{\partial w}{\partial z} + \frac{u}{h_x}\frac{\partial h_z}{\partial x} + \frac{v}{h_y}\frac{\partial h_z}{\partial y} \right) \tag{2.19}$$
$$+\frac{1}{2}\left(\frac{\partial v}{\partial x} - \frac{u}{h_y}\frac{\partial h_x}{\partial y} \right)\left(\frac{\partial u}{\partial z} - \frac{w}{h_y}\frac{\partial h_z}{\partial y} \right)$$

where u, v, and w represent the displacement components along the orthogonal curvilinear principal coordinates x, y, and z, respectively. By performing the necessary arrangements, the Green-Lagrange strain-displacement relationships for the laminated plate can be derived as follows:

$$\varepsilon_x = \frac{\partial u}{\partial x} + \frac{1}{2}\left[\left(\frac{\partial u}{\partial x} \right)^2 + \left(\frac{\partial v}{\partial x} \right)^2 + \left(\frac{\partial w}{\partial x} \right)^2 \right] \tag{2.20}$$

$$\varepsilon_y = \frac{\partial v}{\partial y} + \frac{1}{2}\left[\left(\frac{\partial u}{\partial y} \right)^2 + \left(\frac{\partial v}{\partial y} \right)^2 + \left(\frac{\partial w}{\partial y} \right)^2 \right] \tag{2.21}$$

$$\gamma_{xy} = \frac{\partial u}{\partial y} + \frac{\partial v}{\partial x} + \frac{\partial u}{\partial x}\frac{\partial u}{\partial y} + \frac{\partial v}{\partial x}\frac{\partial v}{\partial y} + \frac{\partial w}{\partial x}\frac{\partial w}{\partial y} \tag{2.22}$$

$$\gamma_{yz} = \frac{\partial v}{\partial z} + \frac{\partial w}{\partial y} + \frac{\partial u}{\partial y}\frac{\partial u}{\partial z} + \frac{\partial v}{\partial y}\frac{\partial v}{\partial z} + \frac{\partial w}{\partial y}\frac{\partial w}{\partial z} \tag{2.23}$$

$$\gamma_{zx} = \frac{\partial w}{\partial x} + \frac{\partial u}{\partial z} + \frac{\partial u}{\partial z}\frac{\partial u}{\partial x} + \frac{\partial v}{\partial z}\frac{\partial v}{\partial x} + \frac{\partial w}{\partial z}\frac{\partial w}{\partial x} \tag{2.24}$$

Considering the First-Order Shear Deformation Theory (FSDT) [61], the displacement components at a general point (x, y, z) in a plate at time t were presented in Eq. (2.13). By substituting these displacements into Equations (2.20-2.24) by retaining all nonlinear terms in each degree of freedom parameter, the following expressions are obtained.

$$\varepsilon_x = \frac{\partial u_0}{\partial x} + \frac{1}{2}\left[\left(\frac{\partial u_0}{\partial x}\right)^2 + \left(\frac{\partial v_0}{\partial x}\right)^2 + \left(\frac{\partial w_0}{\partial x}\right)^2\right] + z\frac{\partial \theta_x}{\partial x} \tag{2.25}$$

$$\varepsilon_y = \frac{\partial v_0}{\partial y} + \frac{1}{2}\left[\left(\frac{\partial u_0}{\partial y}\right)^2 + \left(\frac{\partial v_0}{\partial y}\right)^2 + \left(\frac{\partial w_0}{\partial y}\right)^2\right] + z\frac{\partial \theta_y}{\partial y} \tag{2.26}$$

$$\gamma_{xy} = \frac{\partial u_0}{\partial y} + \frac{\partial v_0}{\partial x} + \frac{\partial u_0}{\partial x}\frac{\partial u_0}{\partial y} + \frac{\partial v_0}{\partial x}\frac{\partial v_0}{\partial y} + \frac{\partial w_0}{\partial x}\frac{\partial w_0}{\partial y} + z\frac{\partial \theta_x}{\partial y} + z\frac{\partial \theta_y}{\partial x} \tag{2.27}$$

$$\gamma_{yz} = \theta_y + \frac{\partial w_0}{\partial y} \tag{2.28}$$

$$\gamma_{zx} = \theta_x + \frac{\partial w_0}{\partial x} \tag{2.29}$$

By rearranging, Equations (2.25-2.29) can be expressed in matrix form as follows:

$$\varepsilon_p = \begin{Bmatrix} \varepsilon_x \\ \varepsilon_y \\ \gamma_{xy} \end{Bmatrix} = \begin{Bmatrix} \dfrac{\partial u_0}{\partial x} + \dfrac{1}{2}\left[\left(\dfrac{\partial u_0}{\partial x} \right)^2 + \left(\dfrac{\partial v_0}{\partial x} \right)^2 + \left(\dfrac{\partial w_0}{\partial x} \right)^2 \right] \\ \dfrac{\partial v_0}{\partial y} + \dfrac{1}{2}\left[\left(\dfrac{\partial u_0}{\partial y} \right)^2 + \left(\dfrac{\partial v_0}{\partial y} \right)^2 + \left(\dfrac{\partial w_0}{\partial y} \right)^2 \right] \\ \dfrac{\partial u_0}{\partial y} + \dfrac{\partial v_0}{\partial x} + \dfrac{\partial u_0}{\partial x}\dfrac{\partial u_0}{\partial y} + \dfrac{\partial v_0}{\partial x}\dfrac{\partial v_0}{\partial y} + \dfrac{\partial w_0}{\partial x}\dfrac{\partial w_0}{\partial y} \end{Bmatrix} + z \begin{Bmatrix} \dfrac{\partial \theta_x}{\partial x} \\ \dfrac{\partial \theta_y}{\partial y} \\ \dfrac{\partial \theta_x}{\partial y} + \dfrac{\partial \theta_y}{\partial x} \end{Bmatrix} \tag{2.30}$$

When the plate is moderately thick ($10 < \dfrac{a,b}{h} < 20$) or thick ($\dfrac{a,b}{h} < 10$), transverse shear strains also occur after deformation. For moderately thick plates, transverse shear strains can be expressed using the FSDT as follows:

$$\varepsilon_s = \begin{Bmatrix} \gamma_{yz} \\ \gamma_{zx} \end{Bmatrix} = \begin{Bmatrix} \theta_y + \dfrac{\partial w_0}{\partial y} \\ \theta_x + \dfrac{\partial w_0}{\partial x} \end{Bmatrix} \tag{2.31}$$

The constitutive equations of laminated composite plates can be expressed in terms of in-plane force (N_x, N_y and N_{xy}) and moment (M_x and M_y) resultants as below:

$$\begin{Bmatrix} N_x \\ N_y \\ N_{xy} \\ M_x \\ M_y \\ M_{xy} \end{Bmatrix} = \begin{bmatrix} A_{11} & A_{12} & A_{16} & B_{11} & B_{12} & B_{16} \\ A_{12} & A_{22} & A_{26} & B_{12} & B_{22} & B_{26} \\ A_{16} & A_{26} & A_{66} & B_{16} & B_{26} & B_{66} \\ B_{11} & B_{12} & B_{16} & D_{11} & D_{12} & D_{16} \\ B_{12} & B_{22} & B_{26} & D_{12} & D_{22} & D_{26} \\ B_{16} & B_{26} & B_{66} & D_{16} & D_{26} & D_{66} \end{bmatrix} \times \begin{Bmatrix} \dfrac{\partial u_0}{\partial x} + \dfrac{1}{2}\left[\left(\dfrac{\partial u_0}{\partial x} \right)^2 + \left(\dfrac{\partial v_0}{\partial x} \right)^2 + \left(\dfrac{\partial w_0}{\partial x} \right)^2 \right] \\ \dfrac{\partial v_0}{\partial y} + \dfrac{1}{2}\left[\left(\dfrac{\partial u_0}{\partial y} \right)^2 + \left(\dfrac{\partial v_0}{\partial y} \right)^2 + \left(\dfrac{\partial w_0}{\partial y} \right)^2 \right] \\ \dfrac{\partial u_0}{\partial y} + \dfrac{\partial v_0}{\partial x} + \dfrac{\partial u_0}{\partial x}\dfrac{\partial u_0}{\partial y} + \dfrac{\partial v_0}{\partial x}\dfrac{\partial v_0}{\partial y} + \dfrac{\partial w_0}{\partial x}\dfrac{\partial w_0}{\partial y} \\ \dfrac{\partial \theta_x}{\partial x} \\ \dfrac{\partial \theta_y}{\partial y} \\ \dfrac{\partial \theta_x}{\partial y} + \dfrac{\partial \theta_y}{\partial x} \end{Bmatrix} \tag{2.32}$$

In Equation (2.32), *A*, *B*, and *D* matrices represent extensional, extensional-bending coupling, and bending terms, respectively.

For moderately thick plates, the constitutive equation in the transverse direction can be expressed in terms of transverse shear force resultants as follows:

$$\begin{Bmatrix} V_x \\ V_y \end{Bmatrix} = \left[\underbrace{\begin{matrix} A_{44} & A_{45} \\ A_{45} & A_{55} \end{matrix}}_{A_s} \right] \begin{Bmatrix} \gamma_{yz} \\ \gamma_{zx} \end{Bmatrix} \tag{2.33}$$

Using the mechanical properties of laminates, *A*, *B*, *D*, and A_s matrices can be calculated as below:

$$\left\{ A_{ij}, B_{ij}, D_{ij} \right\} = \sum_{k=1}^{n} \int_{z_{k-1}}^{z_k} \left\{ 1, z, z^2 \right\} \bar{Q}_{ij}^{(k)} dz \quad (i, j = 1, 2, 6) \tag{2.34}$$

$$A_{ij} = \sum_{k=1}^{n} k_i k_j \int_{z_{k-1}}^{z_k} \bar{Q}_{ij}^{(k)} dz \quad (i, j = 4, 5) \tag{2.35}$$

$$B_{ij} = \sum_{k=1}^{n} k_i k_j \int_{z_{k-1}}^{z_k} z \bar{Q}_{ij}^{(k)} dz \quad (i, j = 4, 5) \tag{2.36}$$

$$D_{ij} = \sum_{k=1}^{n} k_i k_j \int_{z_{k-1}}^{z_k} z^2 \bar{Q}_{ij}^{(k)} dz \quad (i, j = 4, 5) \tag{2.37}$$

where shear correction factors are indicated with $k_i^2 = 5/6 \; (i = 4, 5)$. $\bar{Q}_{ij}^{(k)}$ coefficients in Equation (2.34) indicate transformed stiffness coefficients of *k*-th layer. $\bar{Q}_{ij}^{(k)}$ is presented as follows:

$$\bar{Q}_{11} = Q_{11} \cos^4(\alpha) + 2\left[Q_{12} + 2Q_{66} \right] \sin^2(\alpha) \cos^2(\alpha) + Q_{22} \sin^4(\alpha) \tag{2.38}$$

$$\bar{Q}_{12} = \left[Q_{11} + Q_{22} - 4Q_{66} \right] \sin^2(\alpha) \cos^2(\alpha) + Q_{12} \left[\sin^4(\alpha) + \cos^4(\alpha) \right] \tag{2.39}$$

$$\bar{Q}_{22} = Q_{11}\sin^4(\alpha) + 2[Q_{12} + 2Q_{66}]\sin^2(\alpha)\cos^2(\alpha) + Q_{22}\cos^4(\alpha) \tag{2.40}$$

$$\bar{Q}_{16} = [Q_{11} - Q_{12} - 2Q_{66}]\sin(\alpha)\cos^3(\alpha) + [Q_{12} - Q_{22} + 2Q_{66}]\sin^3(\alpha)\cos(\alpha) \tag{2.41}$$

$$\bar{Q}_{26} = [Q_{11} - Q_{12} - 2Q_{66}]\sin^3(\alpha)\cos(\alpha) + [Q_{12} - Q_{22} + 2Q_{66}]\sin(\alpha)\cos^3(\alpha) \tag{2.42}$$

$$\bar{Q}_{66} = [Q_{11} + Q_{22} - 2Q_{12} - 2Q_{66}]\sin^2(\alpha)\cos^2(\alpha) + Q_{66}\left[\sin^4(\alpha) + \cos^4(\alpha)\right] \tag{2.43}$$

$$\bar{Q}_{44} = Q_{44}\cos^2(\alpha) + Q_{55}\sin^2(\alpha) \tag{2.44}$$

$$\bar{Q}_{45} = [Q_{55} - Q_{44}]\sin(\alpha)\cos(\alpha) \tag{2.45}$$

$$\bar{Q}_{55} = Q_{55}\cos^2(\alpha) + Q_{44}\sin^2(\alpha) \tag{2.46}$$

The components of the transformed stiffness coefficients $\bar{Q}_{ij}^{(k)}$ are presented below:

$$Q_{11} = \frac{E_1}{1 - \nu_{12}\nu_{21}} \tag{2.47}$$

$$Q_{12} = Q_{21} = \frac{\nu_{12}E_1}{1 - \nu_{12}\nu_{21}} = \frac{\nu_{21}E_2}{1 - \nu_{12}\nu_{21}} \tag{2.48}$$

$$Q_{22} = \frac{E_2}{1 - \nu_{12}\nu_{21}} \tag{2.49}$$

$$Q_{66} = G_{12} \tag{2.50}$$

$$Q_{44} = G_{23} \tag{2.51}$$

$$Q_{55} = G_{13} \tag{2.52}$$

where E_1 and E_2 represent the elastic modulus, while v_{12} and v_{21} are the Poisson's ratios of the composite layer in the principal material directions. G_{12}, G_{23} and G_{13} denote the shear modulus.

2.8.2. Equation of Motion

Using the Virtual Work principle, the equation of motion of a composite plate under distributed load *q* (*x*, *y*, *t*) can be expressed in terms of force and moment resultants, as well as inertia effects, as follows:

$$
\begin{aligned}
&\int_{\Omega}[N_x\delta\varepsilon_x^0 + N_y\delta\varepsilon_y^0 + N_{xy}\delta\gamma_{xy}^0 + M_x\delta\varepsilon_x^0 + M_y\delta\varepsilon_y^0 \\
&+M_{xy}\delta\gamma_{xy}^0 + V_y\delta\gamma_{yz}^0 + V_x\delta\gamma_{zx}^0 + (I_0\ddot{u}_0 + I_1\ddot{\theta}_x)\delta u_0 \\
&+(I_0\ddot{v}_0 + I_1\ddot{\theta}_y)\delta v_0 + I_0\ddot{w}_0\delta w_0 + (I_1\ddot{u}_0 + I_2\ddot{\theta}_x)\delta\theta_x \\
&+(I_1\ddot{v}_0 + I_2\ddot{\theta}_y)\delta\theta_y]dxdy = \int_{\Omega} q\delta w_0 dxdy
\end{aligned}
\tag{2.53}
$$

I_0, I_1, and I_2 in Equation (2.53) denote resultant mass inertias of the laminated plate and are expressed as below:

$$
\left\{I_0, I_1, I_2\right\} = \sum_{k=1}^{n}\int_{z_{k-1}}^{z_k}\left\{1, z, z^2\right\}\rho^{(k)}dz \tag{2.54}
$$

where $\rho^{(k)}$ indicates the density of the *k*-th layer.

When no external force (i.e., q=0) acts on the plate, such as in free vibration, Equation (2.53) can be simplified as below:

$$
\mathbf{M}\ddot{\mathbf{U}} + \mathbf{K}(\mathbf{U})\mathbf{U} = 0 \tag{2.55}
$$

In Equation (2.55), $\mathbf{U} = \begin{bmatrix} u_0 & v_0 & w_0 & \theta_x & \theta_y \end{bmatrix}^T$ represents unknown displacements and rotations and $\ddot{\mathbf{U}}$ indicates accelerations. $\mathbf{M}$ denotes the mass matrix and is expressed as below:

$$\mathbf{M}=\iint\begin{bmatrix} I_0 & 0 & 0 & I_1 & 0 \\ 0 & I_0 & 0 & 0 & I_1 \\ 0 & 0 & I_0 & 0 & 0 \\ I_1 & 0 & 0 & I_2 & 0 \\ 0 & I_1 & 0 & 0 & I_2 \end{bmatrix} dxdy \tag{2.56}$$

In Equation (2.55), $\mathbf{K}$ indicates (nonlinear) stiffness matrix that depends on $\mathbf{U}$. It can be expressed in terms of constant, linear, and quadratic parts in $\mathbf{U}$ as $\mathbf{K}=\mathbf{K}_0+\mathbf{K}_1(\mathbf{U})+\mathbf{K}_2(\mathbf{U}^2)$. $\mathbf{K}_0$, $\mathbf{K}_1$, and $\mathbf{K}_2$ parts can be expressed as follows:

$$\begin{aligned} \mathbf{K}_0 &= \iint\left[B_0^T\left(AB_0+BB_1\right)+B_1^T\left(BB_0+DB_1\right)+B_{s0}^T A_s B_{s0}\right]dxdy \\ \mathbf{K}_1 &= \iint\left[B_0^T AB_{01}N_d+N_d^T B_{02}^T\left(AB_0+BB_1\right)+B_1^T BB_{01}N_d\right]dxdy \\ \mathbf{K}_2 &= \iint\left[N_d^T B_{02}^T AB_{01}N_d\right]dxdy \end{aligned} \tag{2.57}$$

where B_{01}, B_{02}, and N_d matrices are defined as below:

$$B_{01}=\begin{bmatrix} \frac{1}{2}\frac{\partial u_0}{\partial x} & 0 & \frac{1}{2}\frac{\partial v_0}{\partial x} & 0 & \frac{1}{2}\frac{\partial w_0}{\partial x} & 0 \\ 0 & \frac{1}{2}\frac{\partial u_0}{\partial y} & 0 & \frac{1}{2}\frac{\partial v_0}{\partial y} & 0 & \frac{1}{2}\frac{\partial w_0}{\partial y} \\ \frac{\partial u_0}{\partial y} & 0 & \frac{\partial v_0}{\partial y} & 0 & \frac{\partial w_0}{\partial y} & 0 \end{bmatrix} \tag{2.58}$$

$$B_{02}=\begin{bmatrix} \frac{\partial u_0}{\partial x} & 0 & \frac{\partial v_0}{\partial x} & 0 & \frac{\partial w_0}{\partial x} & 0 \\ 0 & \frac{\partial u_0}{\partial y} & 0 & \frac{\partial v_0}{\partial y} & 0 & \frac{\partial w_0}{\partial y} \\ \frac{\partial u_0}{\partial y} & \frac{\partial u_0}{\partial x} & \frac{\partial v_0}{\partial y} & \frac{\partial v_0}{\partial x} & \frac{\partial w_0}{\partial y} & \frac{\partial w_0}{\partial x} \end{bmatrix} \tag{2.59}$$

N_d matrix in Equation (2.57) relates in-plane displacement derivatives with in-plane displacements as follows:

$$\left[\frac{\partial u_0}{\partial x} \quad \frac{\partial u_0}{\partial y} \quad \frac{\partial v_0}{\partial x} \quad \frac{\partial v_0}{\partial y} \quad \frac{\partial w_0}{\partial x} \quad \frac{\partial w_0}{\partial y}\right]^T = [N_d]\mathbf{U} \tag{2.60}$$

The form of the N_d matrix in Equation (2.60) depends on how derivatives are expressed. In this study, all spatial derivatives are expressed using GDQ or shortly DQM. Calculation of $\mathbf{K}$ and $\mathbf{M}$ matrices in Equation (2.55) requires integration. In this study, integration is performed numerically using the Gauss-Lobatto quadrature method.

2.9. Comprehensive Literature Review and Research Gap

Composite materials are indispensable for various industrial fields, such as aerospace, automotive, and construction, due to their superior mechanical properties, including lightness, corrosion resistance, high strength-to-weight ratio, and flexibility in design. Among the wide spectrum of reinforcing materials used in composite structures, fiber reinforcement is one of the most preferred techniques [63]. Carbon, aramid, and glass fibers are the most utilized synthetic fibers due to their superior properties in distinctive applications [64], [65]. However, increasing environmental concerns have led researchers to seek more environmentally friendly reinforcement materials, such as natural fibers like flax, jute, and hemp. These fibers are particularly valued for their remarkable sustainability, short growth cycles, low energy demands for production, recyclability, and biodegradability. Summerscales et al. [66] reviewed the production and mechanical characterization of bast fibers, such as hemp, kenaf, jute, and flax, for potential use in polymer matrix composites. Yan et al. [67] reviewed the mechanical behavior and sustainability aspects of flax fiber reinforced composites, covering various matrix types and fiber configurations. Key factors influencing tensile properties, such as humidity, treatments, and defects, were discussed, along with the impact of manufacturing methods, fiber volume, and interface quality on composite performance. Costa and D'Almeida [68] examined how water aging affects the mechanical properties of jute- and sisal-based polyester and epoxy composites. Bambach [69] experimentally and analytically investigated flax, jute, and hemp fiber composite plates and channel sections under pure compression, highlighting their stability in buckling and post-buckling behavior. While intrinsic strength was modest, the gradual and ductile failure modes suggest suitability for light structural applications. An effective width model was also proposed for estimating compressive strength.

Among natural fibers, hemp fiber is one of the most robust natural fibers available due to its attractive mechanical properties and high cellulose content. Moreover, hemp plants can be easily cultivated in diverse environmental conditions globally, and their life cycle assessment reveals further advantages, such as high biomass yield, over other natural fibers [70]. All these advantages have attracted researchers and encouraged numerous studies on hemp fibers. Iucolano et al. [71] evaluated the potential of bio-degummed hemp fibers as a sustainable alternative to glass fibers in gypsum-based composites. Both dynamic and static tests showed that hemp-reinforced gypsum offers comparable strength and toughness to glass fiber-reinforced gypsum, making it a viable, eco-friendly option for improving impact and seismic resistance in non-structural building elements. Boccarusso et al. [72] enhanced the flame retardancy of hemp/epoxy bio-composites by incorporating ammonium polyphosphate. Produced via infusion technology, the composites were tested for fire and mechanical performance. Results showed significant improvement in flame resistance without negatively affecting mechanical properties or manufacturing feasibility, making them suitable for aeronautic applications. PLA-hemp bio-composites with varying fiber content were produced via compression molding, and their flexural, impact, and creep behaviors were analyzed by Durante et al. [17]. Using DMA and Arrhenius theory, the study applied the Time-Temperature Superposition model to assess long-term performance, offering insights into the industrial application limits of natural fiber-reinforced PLA.

Although hemp and other natural fibers have some advantages over synthetic ones, they have some drawbacks, such as lower mechanical properties compared to synthetic fibers. To enhance the strength and stiffness of the natural fiber-reinforced composites, a common approach is to utilize both natural and synthetic fibers in a hybrid form. Recent studies have pointed out that hybrid composites utilizing natural and synthetic fibers can offer both good mechanical properties and environmentally friendly sustainability. Pinto et al. [73] designed hybrid carbon/hemp fiber laminates with four stacking sequences and tested them for bending, shear, damping, and impact performance. Results showed that placing hemp layers near the neutral axis maintains flexural properties close to pure carbon, while placing them on the outer surface enhances energy absorption under both static and dynamic loading. Uppalapati et al. [74] manufactured hybrid hemp-epoxy composites reinforced with carbon, basalt, and natural fillers and tested for structural use. Among various formulations, the hemp/carbon fiber composite showed the highest strength (104 MPa), stiffness, and hardness, outperforming basalt-based variants. The findings support its suitability for load-bearing applications. Pulleti and Singh [75] developed hybrid and functionally graded hemp, carbon, and glass fiber composites and tested them for mechanical performance. Treated hemp fibers were combined with synthetics in various stacking forms. Functionally graded hybrid and sandwich hybrid composites showed superior tensile, compressive, flexural, and shear strength compared to pure hemp composites, supporting their potential as alternatives to glass fiber reinforced polymer in structural use.

Like other natural fibers, hemp fiber has lower mechanical properties than carbon fiber. However, the mechanical properties of hemp fiber are quite close to those of glass fiber and have the potential to be a substitute for glass fiber in composite materials [34]. Besides, the health issues associated with the usage of glass fibers throughout their entire lifecycle, and utilization of natural fibers, such as flax and hemp, have proven to be suitable replacements in various applications [76], [77]. Replacing glass fiber with natural fibers is an active area of research and presents a compelling challenge. In this context, numerous investigations have been carried out to determine and improve the mechanical properties of hemp-carbon fiber-reinforced composite plates. Ramesh et al. [78] tested carbon and hemp fiber hybrid composites, both untreated and alkali-treated, for mechanical and water absorption properties. Alkaline treatment improved strength, with max values reaching 61.4 MPa (tensile) and 122.4 MPa (flexural). Finite element analysis closely matched experimental results, validating the model's predictive accuracy. Pach et al. [79] experimentally investigated the quasi-static penetration behavior of hybrid laminates reinforced with aramid fabrics, carbon fabrics, and short hemp fibers in a polyurethane–polyurea matrix. Results showed that hybridization and layer sequencing significantly influenced energy absorption, punch shear strength, and failure mechanisms. The inclusion of hemp fibers in aramid laminates led to improved impact resistance, demonstrating a positive hybrid effect. Shah et al. [80] evaluated the mechanical performance of hemp fiber and recycled carbon fiber hybrid composites in a polypropylene thermoplastic matrix for injection molding applications. Results showed significant improvements, up to 15% for tensile strength, 35% for flexural strength, and 40% for impact strength, with increasing recycled carbon fiber content.

There are also numerous studies that investigate the effects of hybridization on the mechanical properties of hemp fiber with synthetic fibers, such as aramid and glass. Sangilimuthukumar et al. [81] manufactured Kevlar-hemp and Kevlar-pineapple leaf fiber hybrid composites with numerous weaving architectures via compression molding and tested for quasi-static indentation performance. Twill weave hybrids showed superior peak load and energy absorption compared to other configurations and pure composites. Ultrasonic C-scan imaging revealed that damage size and surface failure were influenced by the weave pattern. Jeyaguru et al. [82] manufactured hemp-Kevlar epoxy hybrid composites with plain, twill, and basket weaves via compression molding and evaluated them for mechanical, vibrational, and acoustic properties. Twill and basket weave hybrids outperformed plain weaves mechanically, while all hybrid types showed better free vibration behavior than single-fiber composites. Ghiaskar and Nouri [83] tested Kevlar and hemp fabric-reinforced elastomeric bio composites with lignin-filled matrices under high-velocity impact to assess their fracture behavior and penetration resistance. Experimental and FEM simulation results confirmed that hemp-based composites achieved impact performance comparable to Kevlar, offering a sustainable alternative with enhanced energy absorption and reduced penetration depth. Boria et al. [84] investigated the low-velocity impact behavior of hemp fiber-reinforced vinyl ester composites using instrumented falling weight tests, including both penetration and indentation scenarios. Hybrid stacking with glass fibers was also evaluated. The study applied and validated analytical models for delamination onset and load-displacement prediction, showing strong agreement with experimental results.

Although numerous studies have been conducted on natural fiber-reinforced hybrid composites (NFRHC) materials, most of them focus on determining the mechanical properties. Few studies focus on the dynamic behavior of NFRHC structures. Some studies reveal that NFRHC materials might have a more efficient energy dissipation mechanism, which can enhance the performance of components where vibration damping is especially crucial [85], [86]. Considering laminated composite plates are frequently subjected to vibration, understanding the dynamic behavior of HFRCs and accurately predicting their behavior under vibration is an important design consideration. Mercedes et al. carried out experimental and numerical linear modal analysis and concluded that there is no discrepancy between vibration modes of the hemp and glass fiber reinforced cementitious matrix sandwich panels [87]. Etaati et al. investigated the damping behavior of short hemp fiber-reinforced polypropylene composites and reported optimal damping performance at intermediate fiber volume fractions, especially for 30 wt% hemp content [88]. Chinnasamy et al. investigated the damping capacity of the hemp, sisal, and areca fiber-reinforced epoxy composites using a linear free vibration test [89]. Jalili et al. studied the acoustic and damping behavior of carbon, glass, and hemp fiber-reinforced polyester composites, revealing that hemp composites demonstrated notable damping with acceptable mechanical performance [90]. In another study, Jalili et al. proposed a flexural free vibration-based non-destructive method to assess viscoelastic parameters, including damping ($\tan\delta$), of carbon, glass, and hemp fiber-reinforced polyester composites [91]. Singh and Rajamurugan fabricated different types of hemp-flax hybrid composites with waste carbon fiber particles and stainless steel wire mesh and investigated the linear vibration behavior of these composites under different boundary conditions [92]. Zhang et al. examined the vibration-damping and acoustic characteristics of composites made from bamboo, cotton, and flax fibers blended with polylactic acid (PLA), as well as fiber-reinforced polypropylene composites incorporating hemp and kenaf fibers. [93]. Di Landro and Lorenzi investigated the vibration-damping performance of thermoplastic composites reinforced with glass fibers and natural fibers, including flax, kenaf, and hemp [94]. They carried out both forced and free vibration tests, and their study revealed that NFRCs are comparable to, and in some cases even superior to, glass fiber-reinforced composites. Chakraborty et al. investigated linear vibration and acoustic behavior experimentally on hybrid composites based on pristine and aged basalt and hemp fibers [95]. They also studied the moisture ingression effect on natural frequencies and damping factors of composites and stated that fibre treatment enhances natural frequencies, whereas aging has adverse effects on natural frequencies. Pinto et al. demonstrated that hybrid carbon/hemp laminates exhibit tunable damping behavior depending on stacking sequence, with improved vibration performance when hemp layers are placed near the neutral axis [73]. Hadiji et al. investigated nonwoven natural fiber (flax, hemp, kenaf) reinforced composites and found that hemp-based laminates offer superior damping behavior compared to glass-reinforced counterparts, making them suitable for vibration-sensitive applications [96]. Singh et al. experimentally and numerically investigated the modal behavior of hemp and jute fiber-reinforced composites, reporting that hemp-based laminates showed higher natural frequencies and damping ratios compared to jute composites [97]. Alaoui et al. carried out static, modal, and harmonic analyses using the finite element method (FEM) for wind turbine blades and attempted to develop a hemp-based composite blade as an alternative to conventional glass fiber-reinforced composite and aluminum alloy wind turbine blades [98]. Their study indicates higher natural frequencies for the hemp composite blade than those of glass fiber-reinforced composite and aluminum alloy blades. Jeyaguru et al. carried out linear free vibration analysis and determined the acoustic characteristics of intra-ply hemp/Kevlar hybrid reinforced composites for various weaving types, such as twill, basket, and plain[82]. They also produced hemp and Kevlar fiber-reinforced composites separately. Results indicate that all the hybrid composites, regardless of weaving types, exhibit superior performance compared to mono-fiber composites. Borah et al. conducted linear free vibration analysis using FEM for carbon, glass, and various NFRC thin plates [99]. They concluded that the plate aspect ratio and volume percentage of fibers have significant effects on the frequency parameter. Singh et al. carried out linear vibration studies for hemp, bamboo, and coir fiber-reinforced composites and concluded that HFRC has higher natural frequencies and better damping characteristics than other natural fibers [100].

Most of the studies conducted on vibration and dynamic analyses employ FEM and the finite difference method, which are widely used numerical techniques for analyzing composite and other structural elements. However, these methods often involve a high computational cost in structural analyses. As a more efficient alternative, the differential quadrature method (DQM) was first introduced by Bellman et al. to acquire an admissible level of accuracy with fewer grid points [101]. Shu subsequently improved the DQM by deriving a straightforward explicit expression for the weighting coefficients, which led to the development of the Generalized Differential Quadrature (GDQ) method. [102]. The GDQ method and its further refinements have been utilized to analyze the thermo-mechanical properties, bending behavior, buckling resistance, vibration characteristics, and transient response of beam, plate, and shell structures [103], [104], [105], [106], [107], [108].

2.9.1. Studies on Laminated Curved Composite Beams

Among the various composite structures, beam-like elements are widely used and often subjected to in-plane or out-of-plane vibrations depending on their loading and boundary conditions [109]. While the free vibration behavior of straight composite beams has been extensively investigated, significantly fewer studies have focused on the in-plane vibration characteristics of curved composite beams. The majority of curved composite beam studies focusing on in-plane vibration behavior are summarized as follows.

A comprehensive analytical framework was developed by Qatu [110] for analyzing the free and forced in-plane vibrations of laminated composite beams with slight curvature. The governing equations were derived utilizing a variational approach to ensure consistency, and exact solutions were obtained for simply supported curved beams. For arbitrary boundary conditions, the Ritz method utilizing algebraic polynomials was applied to estimate the natural frequencies. Case studies included fully free and cantilevered curved beams. The analysis distinguished between extension-bending coupling effects caused by lamination and those induced by curvature. Parametric studies revealed the influence of material orthotropy, curvature, and lamination sequence on vibration behavior.

In another study, Qatu formulated a comprehensive and consistent set of equations for the analysis of free vibration in laminated composite curved beams and closed rings, suitable for both thin and moderately thick structures. For moderately thick beams, the formulation included shear deformation, rotary inertia, and detailed kinematic relations. Exact solutions were obtained for simply supported curved beams, and the study distinguished between extension-bending coupling effects arising from unsymmetrical lamination and those due to geometric curvature. A thorough parametric investigation examined the impacts of rotary inertia, shear deformation, curvature, thickness ratio, and material orthotropy on the natural frequency behavior.

An exact analytical solution was presented for the in-plane vibration of arches with varying curvature and cross-section, employing the Frobenius method alongside the dynamic stiffness approach by Huang et al. [111]. The model accounts for rotary inertia and shear deformation, and ensures a numerically stable and convergent solution. Significantly, the study introduces the first known dynamic stiffness matrix formulated for arches featuring both variable curvature and cross-section. Detailed numerical results were provided for parabolic arches, examining the effects of slenderness, rise-to-span ratio, and cross-sectional variation. High-precision frequency tables and graphical charts were also generated to support practical structural design.

Kadioglu and Iyidogan [112] analyzed the free vibration behavior of cross-ply laminated composite curved beams using the Gateaux differential method in combination with a mixed finite element formulation based on Timoshenko beam theory, accounting for shear deformation. The beam model incorporated six degrees of freedom, including axial and radial displacements, rotation, shear forces, and bending moment. The calculated natural frequencies showed strong correlation with values reported in the existing literature. The study also compared the influence of symmetric and non-symmetric layer configurations on vibration behavior under various boundary conditions.

Li and Soares [113] developed a spectral finite element model to analyze the in-plane free vibration behavior of cross-ply laminated shallow arches, incorporating the exponential shear deformation theory. Hamilton’s principle was applied to derive the governing equations, and the spectral element matrix was constructed using dynamic shape functions derived from the exact solutions of the corresponding homogeneous equations. The Wittrick-Williams algorithm was employed to determine natural frequencies and mode shapes. A comprehensive parametric study was carried out to investigate how stacking sequence, material orthotropy, curvature ratio, length-to-thickness ratio, and boundary conditions affect the vibration behavior of laminated arches.

Lü and Lü [114] developed a precise analytical approach for examining the in-plane free vibrations of simply supported laminated circular arches, based on two-dimensional elasticity theory. The separation of variables method was applied to express field variables as a Fourier series along the longitudinal coordinate, reducing the governing PDEs to ODEs in the radial direction. Subsequently, the state-space approach was applied to obtain a set of first-order differential equations. Due to radial variability, an approximate laminate model with constant coefficients was adopted for tractability. Continuity and traction-free boundary conditions were used to relate state vectors across the arch thickness. The model was validated against existing results, and a parametric study was performed to explore the effects of geometric parameters and stacking sequences on natural frequencies. The results provide reference benchmarks for future studies.

Yang et al. [115] derived the governing differential equations for in-plane free vibration in both uniform and non-uniform curved beams with variable curvature, accounting for axis extensibility, shear effects, and rotary inertia through the extended Hamilton principle. The Galerkin finite element method was employed to numerically solve the equations along the beam’s curved axis. A non-isoparametric finite element formulation was also developed for cases where these effects were excluded. The model enables analysis of curved beams under various geometries and boundary conditions. Mode shapes, natural frequencies, and deformed configurations were computed and validated against results available in the literature, demonstrating the method's accuracy and flexibility.

Yildirim [116] examined the in-plane free vibration characteristics of symmetric cross-ply laminated circular arches by applying both Timoshenko and Bernoulli–Euler beam models, within a distributed parameter modeling framework. The analysis was conducted using the transfer matrix method, incorporating an exact dynamic transfer matrix derived via a numerical algorithm. While the Timoshenko model considered shear deformation, axial, and rotary inertia effects based on FSDT, these effects were neglected in the Bernoulli–Euler model. A detailed parametric study was conducted for varying radius-to-thickness ratios, opening angles (10° and 90°), and different boundary conditions (fixed–simple, fixed–fixed, fixed–free). The effect of the ratio between extensional and transverse moduli on natural frequencies was analyzed, and the non-dimensional outcomes were evaluated through relative error comparisons.

Tseng et al. [117] analyzed the free vibration behavior of composite laminated curved beams with variable curvature using a Timoshenko-type beam theory, which includes both rotary inertia and shear deformation effects. An analytical solution was developed by integrating the dynamic stiffness method with a series solution approach. The curved beam was discretized into multiple elements, within which solutions were expressed as polynomial series governed by recurrence relations. This technique allows for accurate results with fewer terms in the series and in the Taylor expansion of variable coefficients. The method was validated against previous studies, demonstrating its efficiency and suitability for complex laminated arch structures.

Chen [118] developed a DQM model for analyzing the in-plane free vibration of arbitrarily curved beam structures. This approach utilizes the extended differential quadrature technique to discretize the eigenvalue differential equations within individual elements, while also accounting for transition conditions between elements and the overall boundary constraints. The proposed numerical algorithm demonstrated efficient convergence, confirming the method's accuracy and computational effectiveness for modeling complex curved beam geometries.

Malekzadeh [119] calculated the natural frequencies of laminated thick circular deep arches through a solution scheme that combines two-dimensional elasticity theory with the layerwise finite element method. The formulation accounts for variations in beam curvature, normal and transverse shear stresses, and rotary inertia across the arch's thickness. Exact solutions were derived for antisymmetric cross-ply laminated arches under simply supported boundary conditions. The study demonstrated convergence concerning the number of mathematical layers and investigated the effects of thickness-to-length ratio, opening angle, and orthotropy ratio on vibration characteristics. Owing to its precision, the method offers benchmark results for future research.

Malekzadeh and Setodeeh [120] proposed a differential quadrature-based method for analyzing the free vibrations of moderately thick laminated circular arches subjected to general boundary conditions, grounded in Reissner-Naghdi shell theory. The formulation incorporates the effects of rotary inertia and transverse shear deformation, and provides explicit discrete forms of both the equations of motion and boundary conditions. High accuracy was achieved with a minimal number of grid points, demonstrating the efficiency of the DQM. A parametric study was conducted to explore the influence of boundary conditions, thickness-to-length ratio, opening angle, and orthotropy ratio on the natural frequencies of antisymmetric cross-ply laminated arches.

Malekzadeh et al. [121] proposed an efficient and accurate solution procedure for analyzing the free vibration of arbitrarily laminated thick circular deep arches, grounded in two-dimensional elasticity theory and the layer-wise displacement model to accurately capture through-thickness strain variation. The governing equations were derived via Hamilton's principle and discretized using the DQM. A detailed parametric study was conducted considering various classical boundary conditions, opening angles, thickness-to-length ratios, and orthotropy ratios.

Validation was performed by comparing the results with finite element simulations conducted in ABAQUS, as well as with established first- and higher-order shear deformation theories, demonstrating close agreement and confirming the accuracy of the proposed model.

Fard et al. [122] introduced closed-form solutions grounded in refined and higher-order beam theories to analyze the free vibration behavior of simply supported cross-ply laminated composite and sandwich curved beams. The refined theory includes a trapezoidal shape factor that accounts for stress integration over the curved thickness surface, enhancing the accuracy of previous beam models for strongly thick circular curved beams. The stress-strain relationships were derived from a three-dimensional orthotropic lamina formulation. The study presented numerical results for thin/thick straight and shallow/deep curved beams, and the closed-form solutions were validated against exact two-dimensional elasticity solutions and other analytical results from literature, showing excellent agreement.

Luu et al. [123] established an isogeometric analysis framework using NURBS for examining the free vibration behavior of generally laminated deep curved beams of the Timoshenko type with arbitrary curvature. The method integrates the equivalent modulus of elasticity to account for material coupling and accurately incorporates deepness effects into the beam's ABD matrix. Geometry and curvature were modeled using NURBS, enabling seamless analysis of both constant and variable curvature configurations. The model considers shear deformation, axis extensibility, and rotary inertia. Non-dimensional natural frequencies were computed for elliptic, circular, parabolic, and Tschirnhausen's cubic curved laminated beams, with results validating well against existing literature and demonstrating the model's effectiveness for complex free-form geometries.

Based on FSDT, Hajianmaleki and Qatu [124] investigated the static response and free vibration characteristics of generally laminated deep curved beams, incorporating modified ABD parameters. The deepness effect, expressed by the term (1+z/R), was exactly integrated into the stiffness formulation, and an equivalent modulus of elasticity was used to represent both deepness and material coupling effects. Both analytical (for simply supported beams) and numerical solutions via the GDQ method (for other boundary conditions) were provided. The results, including deflections, moment resultants, and natural frequencies, were validated against 3D finite element simulations, showing that the enhanced FSDT model delivers accurate predictions across a range of lamination schemes and support conditions.

Yang et al. [125] presented a comprehensive review of the free in-plane vibration analysis of curved beams, emphasizing the added complexity compared to straight beams due to curvature-induced coupled tangential displacements. The study discussed the governing differential equations of motion derived from various beam theories, accounting for or neglecting effects such as axial extensibility, rotary inertia, and shear deformation. A range of analytical and numerical solution approaches for these equations was identified. The review concluded with a systematic comparison of dynamic responses for curved beams with different geometries and modeling assumptions, providing a clear overview of the current state of research in this field.

Guo et al. [126] developed a formulation for analyzing the static and dynamic vibration behavior of laminated composite curved beams by employing an efficient domain decomposition technique. The beam was divided into multiple segments to improve solution accuracy, and continuity constraints across segment interfaces were enforced via a system potential functional. Chebyshev orthogonal polynomials were employed as admissible displacement functions. The proposed method was validated against published results and finite element simulations using ABAQUS. Following validation, a parametric study was conducted to explore the influence of geometric and material factors on the structural response of laminated curved beams.

Yan et al. [127] presented a novel three-dimensional free vibration analysis of curved metallic and composite beams using a refined beam theory developed within the Carrera Unified Formulation (CUF) framework. The model introduces an Improved Hierarchical Legendre Expansion (IHLE) to describe cross-sectional deformation, combining hierarchical Legendre and Lagrange polynomials to preserve kinematic accuracy while enabling efficient layer-wise modeling. The strong form governing equations were solved utilizing a differential quadrature-based meshless method, eliminating the need for traditional meshing and enhancing computational efficiency. The proposed approach was validated through multiple numerical examples, demonstrating superior convergence and performance compared to conventional 3D FEM and previous CUF-HLE models.

Demir et al. [128] investigated the free vibration and damping behavior of three-layered curved sandwich beams consisting of laminated composite face layers and a viscoelastic core. The governing equations and boundary conditions were derived using the principle of virtual work and, for the first time, solved in the frequency domain using the GDQ method. Model validation was performed by comparing results with existing literature and ANSYS finite element solutions using the modal strain energy method. A comprehensive parametric study examined the effects of lamination angle, layer thicknesses, and curvature on both vibration frequencies and damping behavior, highlighting the method's accuracy and efficiency.

Arikoglu and Ozturk [129] presented a novel method for examining the vibration and damping behavior of sandwich beams with arbitrary curvature and multiple layers (n-layered), incorporating both laminated composite and viscoelastic core configurations. Hamilton's principle was applied to derive the governing equations, which were then solved using the GDQ method. Validation was performed by comparing results with literature data and those obtained from an in-house finite element solver, showing strong agreement. A detailed case study on a spiral curved sandwich beam with a frequency-dependent viscoelastic core was conducted, investigating the effects of core thickness and subtended angle on dynamic behavior.

Considering the computational time and efficiency DQM and GDQ method have great advantages over commonly used FEM for the vibration analysis of different structures [107], [130]. This advantage of GDQ can be quite useful, especially in a parametric study, such as the present one, where the vibration behavior of the structure under consideration needs to be computed repeatedly [131], [132], [133], [134].

2.9.2. Studies on Laminated Composite Plates

In the literature, there are studies focusing on the vibration behavior of laminated composite plates. In this section, the vibration behavior of both linear and nonlinear (large amplitude) laminated composite plates will be discussed. Gopalan et al. [86] experimentally and numerically analyzed the linear free vibration behavior of woven flax/bio-epoxy laminated composite plates, addressing the growing interest in sustainable green composites for structural applications. The elastic constants required for numerical modeling were determined using both conventional mechanical tests and the impulse excitation technique, and the results were compared to validate the measurements. Finite element analysis was conducted using ANSYS, and the model was verified against experimental modal testing. Additionally, a parametric optimization was performed using response surface methodology (RSM) to study the effects of ply orientation, boundary condition, and aspect ratio on dynamic behavior. The study showed a strong correlation between regression-based predictions and numerical results.

Malekzadeh and Shojaee [105] conducted a nonlinear free vibration study on thin to moderately thick laminated composite skew plates based on FSDT, with numerical solutions obtained using DQM. Geometric nonlinearity was incorporated using Green's strain in combination with von Kármán assumptions, and the model included the effects of rotary inertia. After spatial discretization, both the direct iterative approach and the harmonic balance technique were employed to solve the nonlinear equations. The influence of aspect ratio, thickness-to-length ratio, skew angle, and various boundary conditions on nonlinear frequencies and convergence was examined. The results showed good agreement with existing methods, validating the accuracy of the approach.

Maraş and Yaman [108] conducted a numerical linear free vibration analysis of fiber metal laminated (FML) composite plates, focusing on commonly used hybrid structures like CARALL, GLARE, and ARALL, which combine fiber-reinforced polymer layers with aluminum sheets. The DQM method was employed to compute natural frequencies, and the numerical results were validated with experimental data. A parametric study was carried out to assess how different fiber orientation angles and boundary conditions influence the vibration characteristics of antisymmetric carbon and glass fiber-based FMLs. The study identified key layer configurations that significantly affect the dynamic characteristics of these hybrid structures.

The linear free vibration behavior of FML composite plates was investigated through both numerical and experimental methods by Maraş and Yaman [130]. The study utilized classical plate theory to derive the governing equations of motion and applied various forms of the differential quadrature method, standard DQ, GDQ, and harmonic DQ (HDQ), to solve them. The FMLs, composed of fiber-reinforced polymer layers (carbon, glass, aramid) and metal sheets, were analyzed under different boundary conditions. Numerical results showed strong agreement with experimental data, confirming the accuracy and convergence of the DQ-based methods. The study highlights the reliability and effectiveness of DQ approaches in modeling the vibrational characteristics of hybrid FML structures, offering practical value for their use in engineering applications.

Bacciocchi et al. [131] performed linear free vibration analyses of laminated composite plates, singly-curved, and doubly-curved shell structures with continuously varying thickness, which enables stiffness tailoring without increasing weight. The study employed the GDQ method to solve the governing equations, offering a versatile and reliable numerical approach. The method's accuracy was validated through comparisons with analytical, semi-analytical, and three-dimensional finite element solutions. The framework was built upon a general kinematic formulation that supports various higher-order structural theories, allowing the kinematic expansion order to be freely selected to suit different modeling needs.

The nonlinear transient air blast response of basalt/epoxy laminated composite plates was investigated by Süsler et al. [135] using the GDQ method, which offers reduced computational time and complexity compared to finite element approaches. A shock tube setup was developed for experimental validation, and transient responses in terms of strain, displacement, and acceleration were measured. Numerical results showed strong agreement with experimental data. Additionally, the dynamic performance of Kevlar/epoxy, glass/epoxy, and carbon/epoxy composite plates was analyzed using the same method, and the results were compared with those of the basalt-based composite to evaluate relative blast resistance.

Maraş and Yaman [136] numerically and experimentally investigated the linear vibration behavior of FML composite plates, which are hybrid structures combining fiber-reinforced polymers with metal sheets. The governing equations were formulated using classical plate theory, and the GDQ method was employed for the numerical solution. Natural frequencies obtained from the model were validated through experimental modal analysis, showing strong agreement. A parametric study was conducted to examine the effects of material composition, geometry, and boundary conditions. Results indicated that increasing the number of aluminum layers or relocating them from the surface to the core significantly influenced the fundamental frequencies. Boundary conditions also had a marked impact on the dynamic response.

Civalek [137] analyzed the nonlinear dynamic response of rectangular laminated composite plates on nonlinear Pasternak-type elastic foundations using a coupled numerical method. The study employed FSDT and incorporated von Kármán geometric nonlinearity to model moderately thick plates. Spatial and temporal discretizations of the governing nonlinear equations were achieved using a combination of the discrete singular convolution (DSC) and DQM. The proposed method was validated through comparison with existing results in the literature. A detailed parametric study was conducted to assess how foundation stiffness, boundary conditions, and geometric properties influence the transient nonlinear vibration behavior of the laminated plate structures.

Malekzadeh and Vosoughi [138] investigated the large-amplitude free vibration behavior of thin to moderately thick angle-ply laminated rectangular plates with rotational restraints at the edges, employing the DQM. The analysis was conducted based on both classical plate theory and FSDT, incorporating Green's strain and von Kármán geometric nonlinearity. Boundary conditions were applied directly at the grid points, and the nonlinear eigenvalue problem was solved using a direct iterative method after transforming the equations to the frequency domain. Convergence and accuracy of the method were validated through comparison with classical and linear vibration cases. The study also explored the influence of various parameters on the nonlinear-to-linear natural frequency ratio.

Singha et al. [139] studied the large-amplitude free flexural vibration behavior of thin laminated composite skew plates through a finite element approach. Geometric nonlinearity was incorporated through von Kármán assumptions, and composite material was modeled with orthotropic lamina properties. The study validated its numerical model by comparing nonlinear frequency ratios against existing literature, demonstrating strong agreement. Parametric analysis revealed the influence of plate skewness and vibration amplitude on natural frequency behavior, confirming a characteristic "hardening" response, where increased amplitude leads to a stiffening effect.

In another study, Singha and Daripa [140] investigated the large-amplitude free flexural vibration behavior of symmetrically laminated composite skew plates using the FEM. The model incorporated in-plane and rotary inertia, shear deformation, and von Kármán geometric nonlinearity. Galerkin's method was used to derive the nonlinear matrix amplitude equations, which were solved via direct iteration, and the results were verified with Newmark's time integration method. A parametric study was performed to analyze how fiber orientation, skew angle, and boundary conditions affect nonlinear frequency ratios, revealing a clear dependence of vibration behavior on these design variables.

The large-amplitude free vibration behavior of orthotropic laminated composite plates with randomly varying material properties was analyzed by Onkar and Yadav [141]. The study is based on classical laminate theory and incorporates von Kármán-type geometric nonlinearity. Governing equations were derived using Hamilton's principle, and the solution was obtained through a term-wise series integration approach. A perturbation technique was employed to determine second-order response statistics, capturing the effect of material uncertainty. Parametric studies investigated the impact of aspect ratio, side-to-thickness ratio, amplitude, and material variability on vibration characteristics for both cross-ply symmetric and antisymmetric laminates under simply supported edges.

A theoretical investigation was conducted on the large-amplitude free vibration behavior of symmetric and unsymmetric composite plates using a nonlinear finite element modal reduction method by Lee et al. [142]. The nonlinear problem was reduced to a set of Duffing-type modal equations, which were solved using both the Runge–Kutta integration method and the harmonic balance method. This approach was shown to provide comparable results with significantly reduced computational effort. The study evaluated the influence of mode contributions on maximum deflection and presented frequency ratios for both isotropic and composite plates under varying deflection levels. Convergence concerning the number of finite elements, harmonic terms, and linear modes was also analyzed.

The nonlinear free vibration of laminated composite and FML rectangular plates was analyzed by Shooshtari and Razavi [143] based on FSDT, accounting for both shear deformation and rotary inertia. The governing equations were reduced via a force function to a system of coupled nonlinear PDEs and a compatibility equation. Applying the Galerkin method, the authors derived a novel nonlinear ordinary differential equation that incorporates both nonlinear inertia and stiffness terms. Analytical expressions for nonlinear frequency and displacement were then obtained using the method of multiple time scales. The approach was validated against existing results for isotropic and laminated plates, and the influence of various system parameters on nonlinear frequency behavior was systematically explored.

In another study, Shooshtari and Razavi [144] investigated the nonlinear free and forced vibration behavior of anti-symmetric angle-ply composite and FML rectangular plates using FSDT, incorporating both shear deformation and rotary inertia. The governing nonlinear equations were reduced via the Galerkin method to a single nonlinear ordinary differential equation. This equation was solved analytically using the multiple time scales method, allowing the derivation of expressions for nonlinear frequencies. Validation against existing results confirmed the accuracy of the model. The effects of key system parameters on the nonlinear vibration response of FML rectangular plates were also analyzed.

Houmat [145] analyzed the geometrically nonlinear free vibration behavior of single-ply composite rectangular plates with variable fiber spacing. The study considered straight, parallel fibers, more densely distributed at the center to enhance stiffness, and was based on von Kármán's nonlinear thin plate theory. The problem was numerically solved employing the hierarchical FEM, and the time-domain equations were transformed into the frequency domain utilizing the harmonic balance method. A linearized updated mode method was used to solve the nonlinear system iteratively. The analysis, conducted for clamped and simply supported square plates with E-Glass, Boron, and Graphite fibers in epoxy matrices, showed that fiber distribution, volume fraction, fiber type, and boundary conditions significantly affect the plate's hardening behavior.

Adhikari and Dash [146] investigated the geometrically nonlinear free vibration of laminated composite plates using a higher-order non-polynomial shear deformation theory that captures a realistic, nonlinear distribution of transverse shear stresses through the plate thickness. The theory inherently satisfies zero shear traction conditions at the plate surfaces. The governing equations were derived using Lagrange's equations and solved numerically through a finite element method with a displacement field incorporating seven degrees of freedom. Various laminate configurations, symmetric, anti-symmetric, cross-ply, and angle-ply, were analyzed under different edge support conditions to evaluate their influence on nonlinear vibration behavior.

Wang et al. analyzed the geometrically nonlinear vibration behavior of carbon fiber reinforced composite rectangular plates with random material properties, using a meshless numerical approach grounded in the reproducing kernel particle method. The study employed classical plate theory and derived the governing equations through the principle of virtual displacement. Linear and nonlinear eigenvalues and mode shapes were computed iteratively using dimensionless amplitude. The meshless method demonstrated high computational accuracy, particularly in enforcing essential boundary conditions. A comprehensive parametric study was conducted to evaluate the influence of boundary conditions, aspect ratio, plate dimensions, and carbon fiber content on the nonlinear dynamic response.

Nonlinear free vibration behavior of laminated composite plates and shallow shell panels (spherical, cylindrical, and hyperboloid types) was investigated using a non-polynomial inverse trigonometric HSDT incorporating seven degrees of freedom by Lore et al. [147]. The model accounted for geometric nonlinearity through Green-Lagrange strain and von Kármán assumptions, and used a nonlinear finite element formulation with an eight-noded, continuous isoparametric rectangular element. The theory ensured a parabolic distribution of transverse stresses and satisfied traction-free boundary conditions by default. A detailed parametric study was performed to assess the influence of plate/shell geometry, lamination patterns, material combinations, curvature, and boundary conditions on the nonlinear frequency response. The accuracy of the method was validated against existing results.

2.9.3. Identified Research Gap and Contribution of This Study

As can be seen from the literature review, there are promising studies investigating the hemp-based composite structures. However, studies focusing on the vibrational behavior of the HFRC structures are quite few. In order to investigate and promote the usability of HFRCs in structural applications, a comprehensive vibration analysis of these structures is needed. Although numerous studies have investigated the in-plane vibration behavior of curved composite beams, the majority rely on arbitrarily chosen material properties, and none have specifically examined the vibrational performance of HFRC curved beams. In this context, the current study investigates the in-plane free vibration characteristics of curved composite beams reinforced with hemp fibers in pure and hybrid form (e.g., carbon/hemp, carbon/glass, and glass/hemp). The mechanical properties of pure carbon, glass, and hemp fiber composites are experimentally obtained through uniaxial tensile testing. A numerical model based on the GDQ method is developed in MATLAB and validated through benchmark problems available in the literature. To further validate the numerical findings, experimental vibration analysis is performed on nine straight composite beam specimens with different configurations. The close agreement between the experimental and numerical results is observed. One of the objectives of this study is to evaluate the potential of hemp fiber as a sustainable substitute for traditional fibers, particularly glass fiber. Accordingly, a comprehensive parametric study is carried out to investigate the influence of fiber type, hybridization, curvature ratio, stacking sequence, and boundary conditions on the vibrational characteristics of both pure and hybrid composite configurations.

Considering that plates are one of the most common structural elements and are used in almost every field, vibration analyses were also carried out for plates in this study. Even though numerous studies on HFRC materials exist, most of them focus on the mechanical properties and linear free vibration behavior of HFRC. However, none of them focus on the large amplitude (nonlinear) free vibration behavior of hemp fiber-reinforced hybrid composite plates. Previous studies that focus on the nonlinear vibration of composite plates utilize random material properties or fiber reinforcement materials other than hemp. In this context, another numerical model based on the GDQ method, for the linear and nonlinear vibration analysis of the laminated plates, is developed in MATLAB and validated through benchmark problems available in the literature. Then, a detailed parametric study was conducted to investigate the effects of hybridization, stacking sequence, aspect ratio, and boundary conditions on the large amplitude free vibration behavior of hemp-based hybrid laminated plates.

3. MATERIALS AND METHODS

3.1. Materials Used in Manufacturing

3.1.1. Fiber Reinforcement Materials

In the present study, plain woven hemp, carbon, and glass fabrics were used as reinforcement materials. In Figure 3.1, carbon, glass, and hemp fabric samples are presented. The mechanical and physical properties of each fabric are provided in Table 3.1. Density, tensile strength, and elastic modulus values of the carbon, glass, and hemp fibers are taken from the literature.

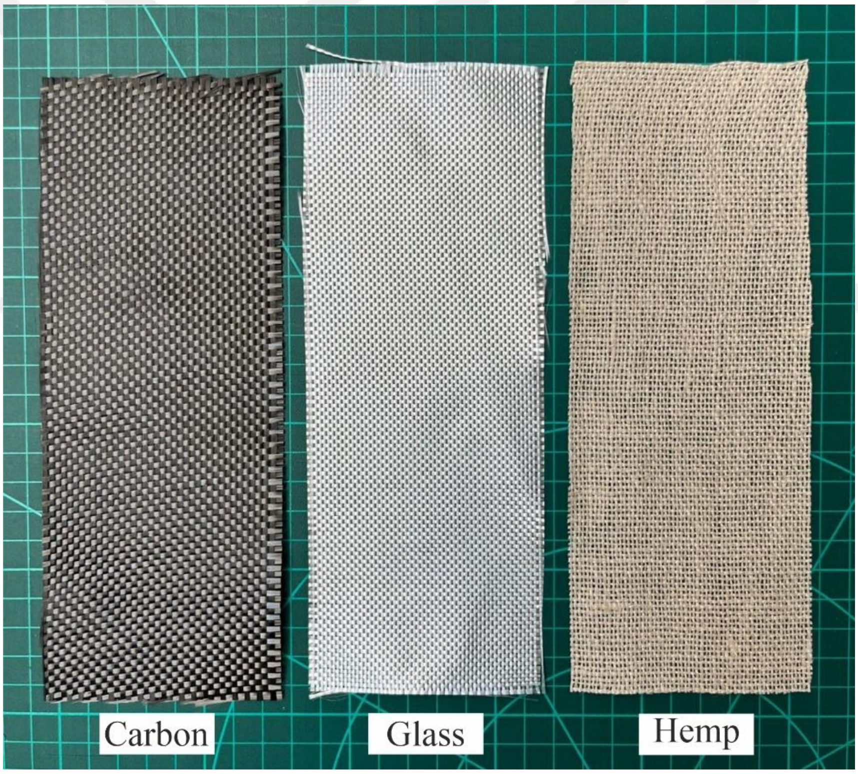

Figure 3.1. Carbon, glass, and hemp fabric samples

Table 3.1. Mechanical and physical properties of fabrics

Fabric	Basic Weight (g/m^2)	Woven Type	Density (g/cm^3)	Tensile Strength (Mpa)	Elastic modulus (GPa)	Refs.
Carbon	200	Plain	1.7	4000	230-240	[148]
Glass	200	Plain	2.5	2000-3000	70	[43]
Hemp	260	Plain	1.4	550-1110	30-70	[43]

3.1.2. Epoxy Resin System

As a matrix element, the HEXION MGS L160/H160 epoxy system, supplied by Dost Kimya, was used. The MGS L160 laminating system is widely utilized in industries such as aerospace, automotive, marine, space, wind energy, and defense. It is particularly suitable for small-to-medium-scale infusion applications. The system cures at room temperature, and with post-curing, it can produce parts that meet civil aviation standards [149]. The physical and chemical properties of the MGS L160 laminating resin are listed in Table 3.2, while those of the H160 hardener are provided in Table 3.3.

Table 3.2. Physical and chemical properties of the MGS L160 resin

Density (g/cm^3)	1.13-1.17
Viscosity (mPas)	700-900
Epoxy equivalent (g/eq)	166-182
Epoxy Equivalent Value (eq/100 g)	0.55-0.60
Measurement Condition	25 °C

Table 3.3. Physical and chemical properties of the MGS H160 hardener

Density (g/cm^3)	0.96-1.00
Viscosity (mPas)	10-50
Amine value (mgr KOH/g)	560-650
Refractor index	1.520-1.521
Measurement Condition	25 °C

3.2. Manufacturing of Laminated Composites

The VARTM method was utilized for the production of the composite materials. The VARTM method was preferred in this study due to its ability to produce more precise composites rather than the commonly used hand layup (HL) method. The VARTM method provides uniform quality because the vacuum effect evenly distributes the resin across the composite, making the process less dependent on the operator’s expertise. The VARTM method is a viable alternative to HL and is especially preferred for manufacturing large components, as it allows better resin penetration between layers, resulting in composite structures that are both lighter and stronger. Although VARTM requires more equipment than the HL method, precise resin usage, consistently produced parts of the desired quality and smoothness, and elimination of uneven resin absorption make it superior to the HL method [150].

For the production of the composite plates, the designated area is initially cleaned with a surface cleaner. Following, to facilitate taking out the produced part from the mold, mold release wax is applied to the surface of the mold. Then the fabrics are aligned in the predetermined sequence in the area encircled by the sealant tape. Peeling fabric is laid down on the composite fabrics to facilitate taking out the produced part from the excess resin and infusion mesh. To facilitate the movement of the resin, an infusion mesh is placed on the peeling fabric. And finally, to avoid air infiltration, everything is closed with a vacuum bag and sealant tape. Sufficient space is left for the inlet and outlet hoses, and the prepared resin mixture is pulled into the system using a vacuum pump. Figure 3.2 illustrates the production process of the VARTM method step by step. The overall production scheme of the VARTM method is also illustrated in Figure 3.3. The vacuum pump is operated at a pressure of 1 bar. After the laminates have completely absorbed the resin, the pump is switched off, and the composite part is left to cure for 24 hours. All manufacturing steps were conducted at an ambient temperature of 25 ± 2 °C.

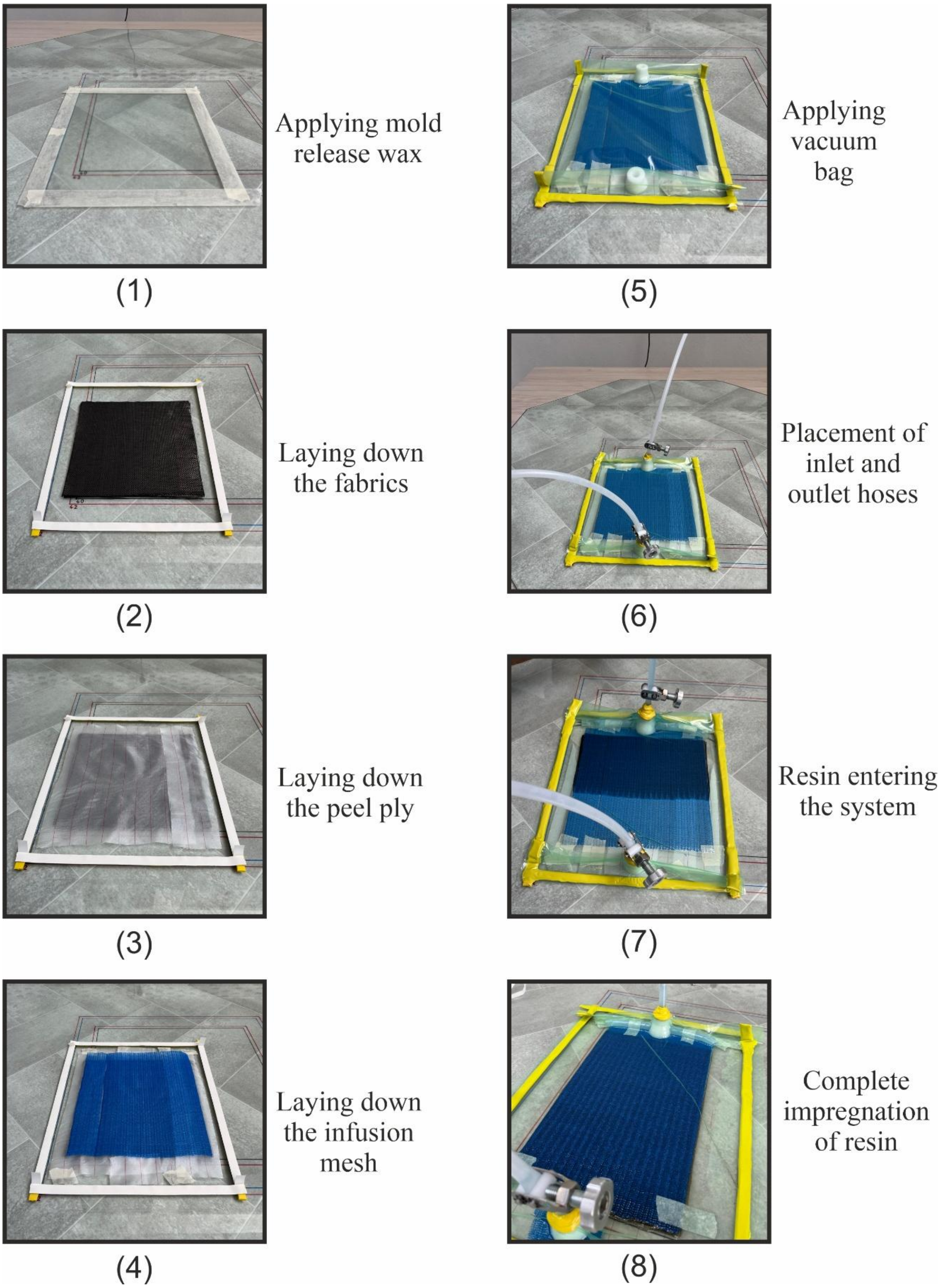

Figure 3.2. Composite material production using the VARTM method

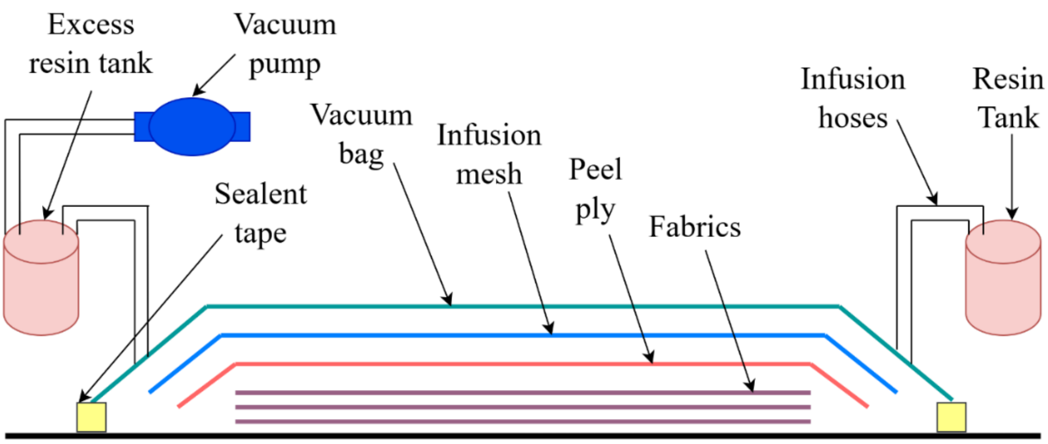

Figure 3.3. The production scheme of the VARTM method

In the first place, pure carbon, pure glass, and pure hemp fiber reinforced composite materials were produced for tensile tests to determine the mechanical properties of these composite materials. Then, for the experimental vibration tests, nine pure and hybrid form composites were manufactured. In Figure 3.4, pure carbon, glass, and hemp fiber-reinforced composite plates are presented. After the production process was completed, tensile and vibration test specimens of the desired dimensions were cut from the produced plates using a water jet (Figure 3.5).

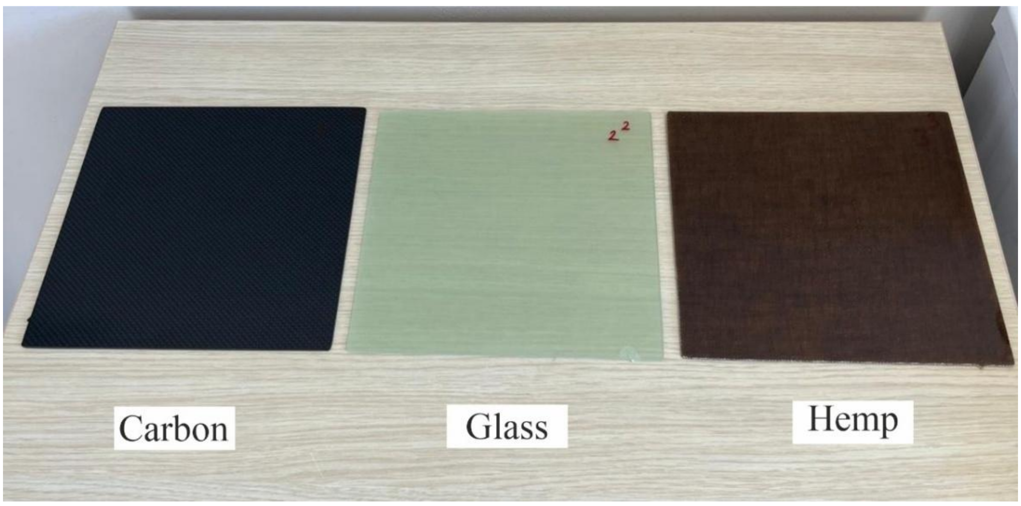

Figure 3.4. Pure carbon, glass, and hemp fiber-reinforced composite plates

Figure 3.5. Cutting the tensile and vibration test specimens using water jet

3.3. Experimental Methods

3.3.1. Tensile Testing

To evaluate the mechanical properties of the pure carbon, pure glass, and pure hemp fiber-reinforced composites, a tensile test was carried out. Tensile test specimens were cut from the produced plates using a water jet, with dimensions of 250 × 25 × (2.2 ± 0.05) mm^3 according to the ASTM D3039 standard [151]. Figure 3.6 presents the tensile test specimens made from carbon, glass, and hemp composites.

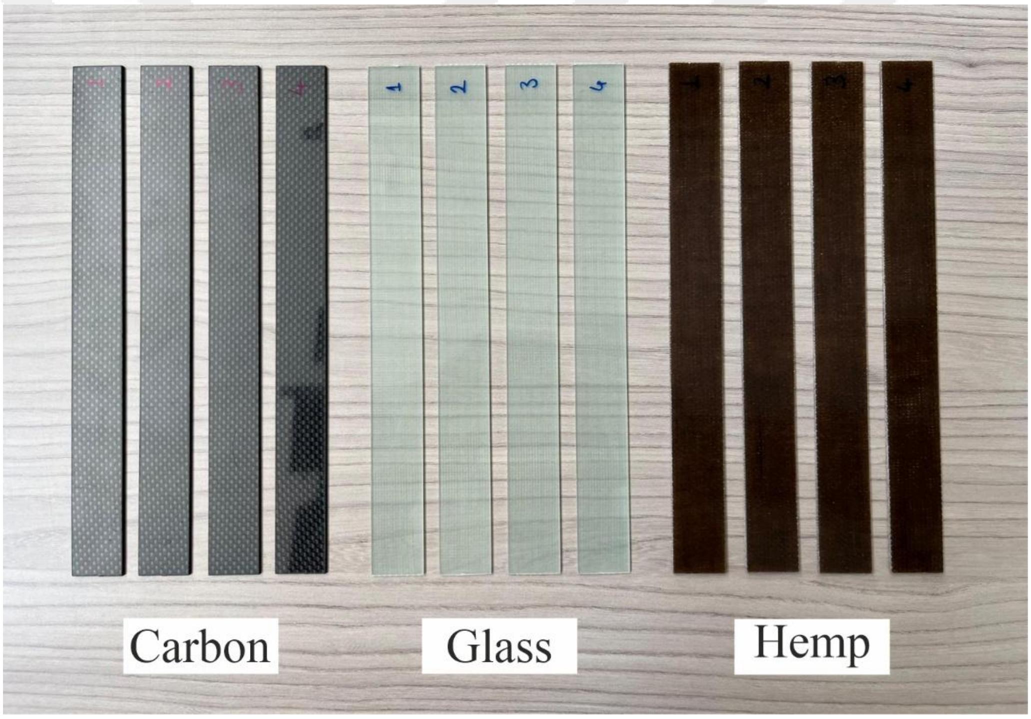

Figure 3.6. Tensile test specimens cut by water jet

To ensure proper attachment to the testing device, 0.5 mm thick aluminum sheets are bonded to the ends of the tensile test specimens using epoxy adhesive. This technique enhances the grip within the machine's jaws and prevents damage to the specimens. The prepared specimens after bonding the aluminum sheets are presented in Figure 3.7. The tensile tests were carried out utilizing a SHIMADZU testing machine (Figure 3.8) located in the Mechanical Engineering

Laboratory at Adana Alparslan Türkeş Science and Technology University. All tests were conducted under an ambient temperature of 25 ± 2 °C. For each configuration 4, a total of 12 samples were tested. The tensile test results for each material configuration were determined by averaging the results from four individual samples. Testing was performed at a displacement rate of 2 mm/min, according to ASTM D3039, to determine the relevant mechanical properties of the composites. In Figure 3.9, the tensile test specimen attached to the tensile test device and the specimen after the breakage are presented.

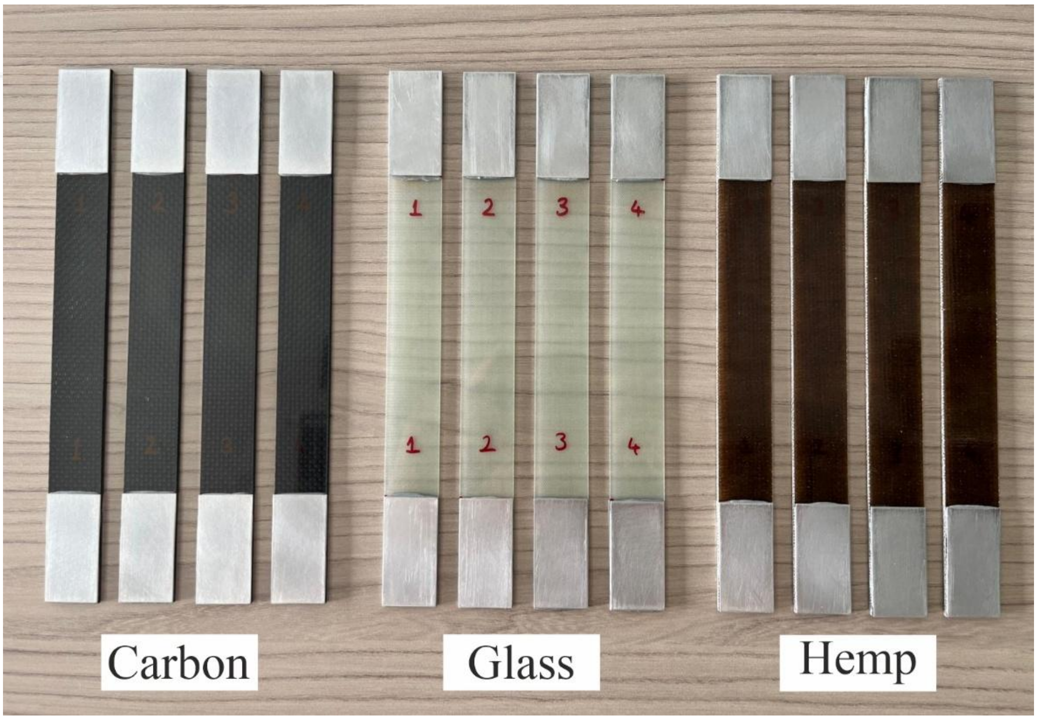

Figure 3.7. Tensile test specimens after the aluminum sheets are bonded

Figure 3.8. SHIMADZU tensile testing machine

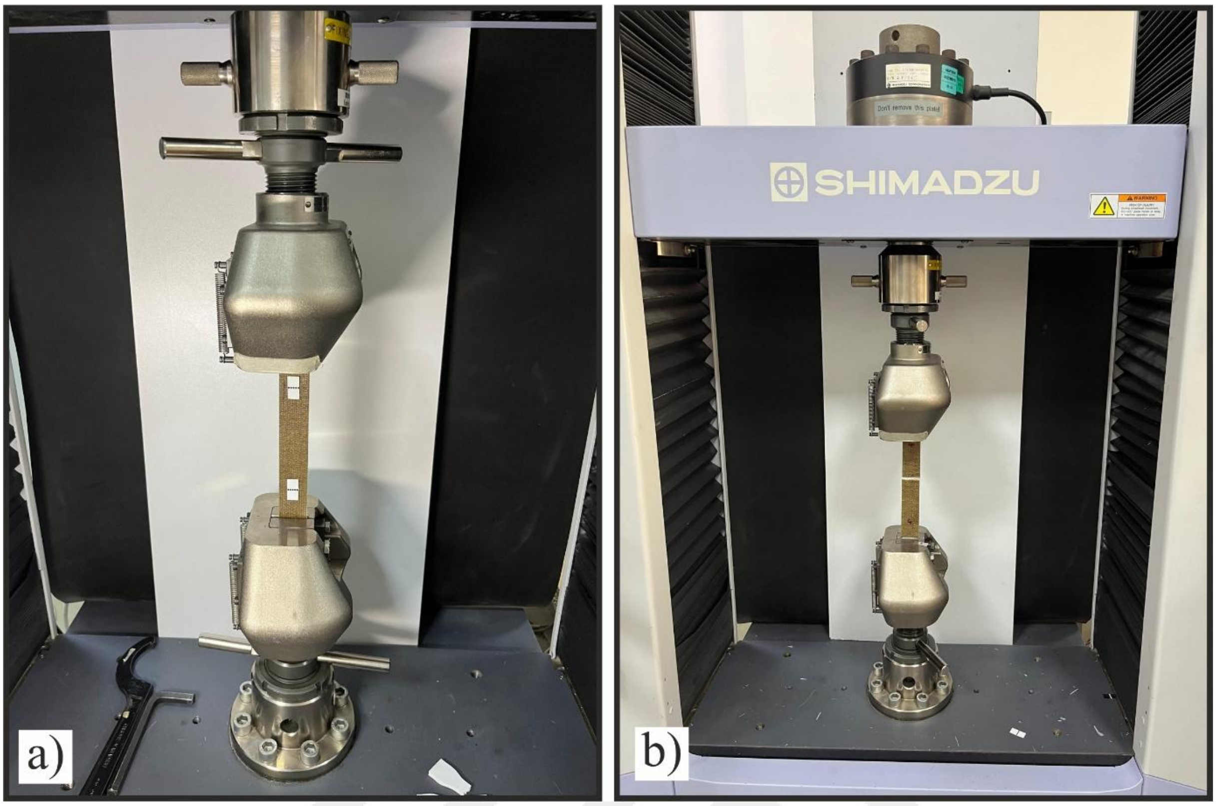

Figure 3.9. a) Attaching the tensile test specimen to the tensile test device, **b)** Tensile test specimen after the breakage

3.3.2. Experimental Vibration Test Procedure and Data Acquisition

For the experimental vibration test, nine laminated composite straight beam specimens that have dimensions of 340×25×(2.2±0.5) mm^3 were cut from the manufactured plates using a water jet. Composite specimens were then prepared by attaching metal sheets having dimensions of 25×20×0.4 mm^3 at the free end of the beams using epoxy adhesive for the test. After mounting the metal sheets, the final weight of the specimens was measured, and the total weight of the metal sheets and epoxy adhesive was measured as 3.3 grams on average. In order to detect the displacement momentarily by the magnetic sensor, these metal sheets are crucial. In Figure 3.10, cantilever beam test specimens and metal sheets attached to the free tips are presented.

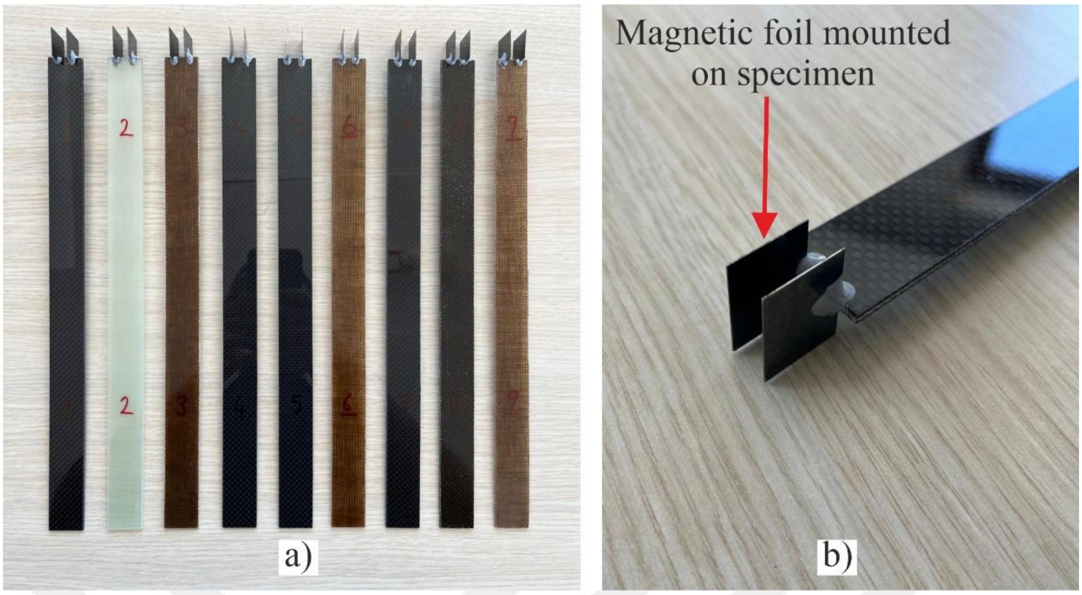

Figure 3.10. a) Vibration test specimens, **b)** Magnetic foil on the free end of the cantilever beam

TecQuipment TM166 Free Vibration test device (TecQuipment Ltd.), which is detailed in Figure 3.11, was used for the experimental vibration study. This specialized device is intended for assessing the free vibration behavior, especially the fundamental mode, of cantilever beams by precisely capturing and documenting displacement measurements of the specimen. Test specimens can be regarded as cantilever beams, as one end is rigidly fixed to the testing apparatus while the other end remains free to move (Figure 3.12). A magnetic displacement sensor with high sampling capacity is employed for this purpose and calibrated to standard interval settings. The tip of each cantilever test specimen was given an initial displacement of 4 mm to initiate the free vibration during testing. The beams were subsequently allowed to undergo free vibration, during which the displacement sensor continuously recorded their displacement data. To guarantee precise data collection and avoid aliasing, the sampling rate for the displacement measurements was carefully set by the Nyquist sampling theorem. A sampling rate of 125 Hz was chosen, resulting in a Nyquist frequency of 62.5 Hz, which is well above the highest frequency observed in the beam tests. This effectively eliminates the risk of aliasing. A digital low-pass filter was applied to enhance the accuracy of the sampled data, yielding a smoother and more reliable representation of the experimental results. Throughout the experiment, real-time displacement data were visualized on a computer screen via the

Versatile Data Acquisition System (VDAS) software, developed by TecQuipment Ltd. Subsequently, the time-displacement data were exported to an Excel file and examined to identify the fundamental natural frequencies of the beams. The necessary calculations were carried out utilizing a code developed in the MATLAB program. Fast Fourier Transform (FFT) analysis was employed to extract the damped natural frequency results derived from the time-displacement measurements, as it is regarded as the most reliable and commonly used method for this type of calculation. FFT analysis was applied to the time-displacement data of each specimen, and the resulting frequency-domain graphs were obtained. In addition, the damping ratios were calculated through the exponential curve fitting technique, which is particularly appropriate for viscously underdamped systems [152]. This method involves aligning an exponentially decreasing curve with the peak values of the sinusoidal, decaying time-displacement response of the vibrating system. Since the produced vibration test specimens have damping ratio values less than 0.2, which applies to most structural systems, the reduction in natural frequency value by damping is minimal and therefore typically considered negligible [152]. In the present study, the damped natural frequency (ω_D) values were obtained from experimental data, and then the undamped natural frequency (ω_n) values were evaluated according to Eq. (3.1). The ω_n values were found almost identical with ω_D values. These results are presented in further sections.

$$\omega_n = \frac{\omega_D}{\sqrt{1-\zeta^2}} \tag{3.1}$$

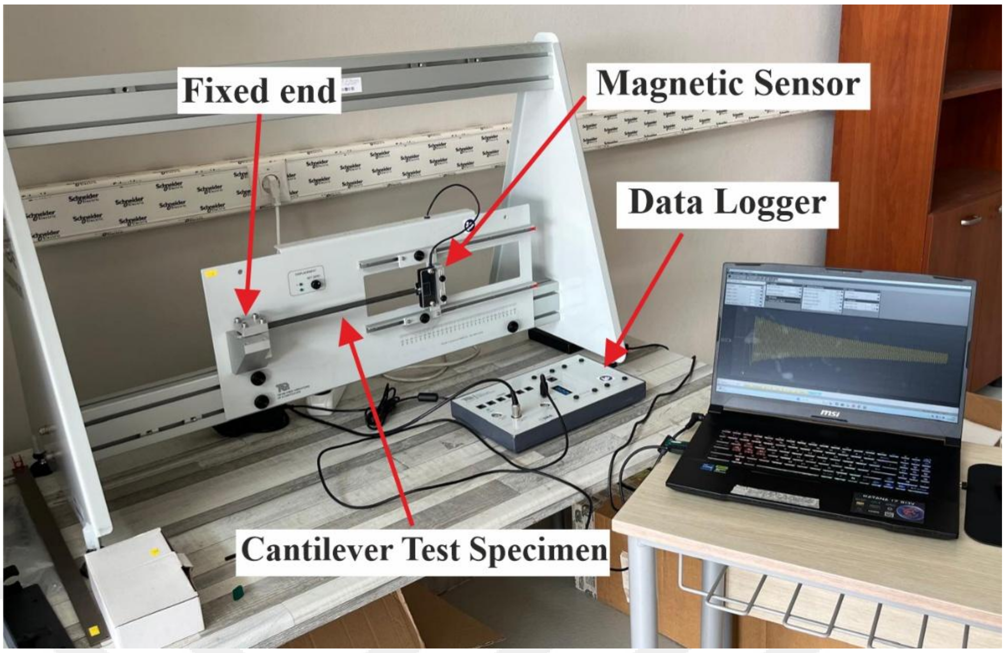

Figure 3.11. Experimental setup for cantilever beam specimens

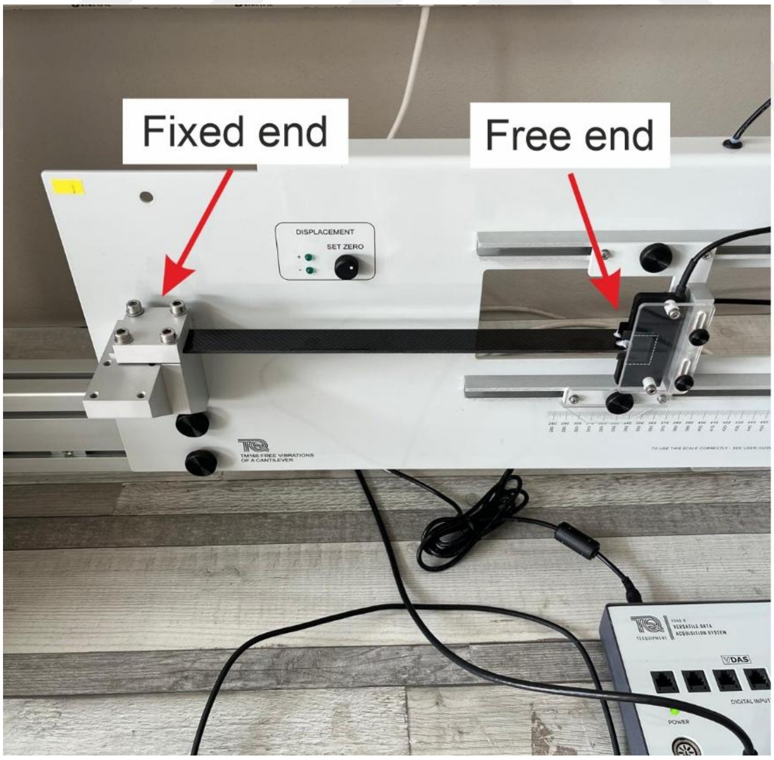

Figure 3.12. Vibration test specimen mounted on TM 166 vibration test device

3.4. Numerical Solution Procedure

3.4.1. Geometric Mapping

In the present study, integral terms within the virtual work equations are calculated using non-uniform Gauss-Lobatto quadrature or Gauss quadrature rules. As illustrated in Figure 3.13, numerical integration is typically performed by transforming the Cartesian domain into a bi-unit square domain through geometric mapping, as follows:

$$x(\xi,\eta) = \sum S_k(\xi,\eta)x_k \quad -1 \le \xi \le 1 \tag{3.2}$$

$$y(\xi,\eta) = \sum S_k(\xi,\eta)y_k \quad -1 \le \eta \le 1 \tag{3.3}$$

where, $S_k(\xi,\eta)$ represents the interpolation functions utilized in the geometric mapping process, while ξ and η are the natural coordinates of the bi-unit square domain. These interpolation functions are commonly found in finite element literature and are defined as follows:

$$S_1 = \frac{1}{4}(1-\xi)(1-\eta) \tag{3.4}$$

$$S_2 = \frac{1}{4}(1+\xi)(1-\eta) \tag{3.5}$$

$$S_3 = \frac{1}{4}(1+\xi)(1+\eta) \tag{3.6}$$

$$S_4 = \frac{1}{4}(1-\xi)(1+\eta) \tag{3.7}$$

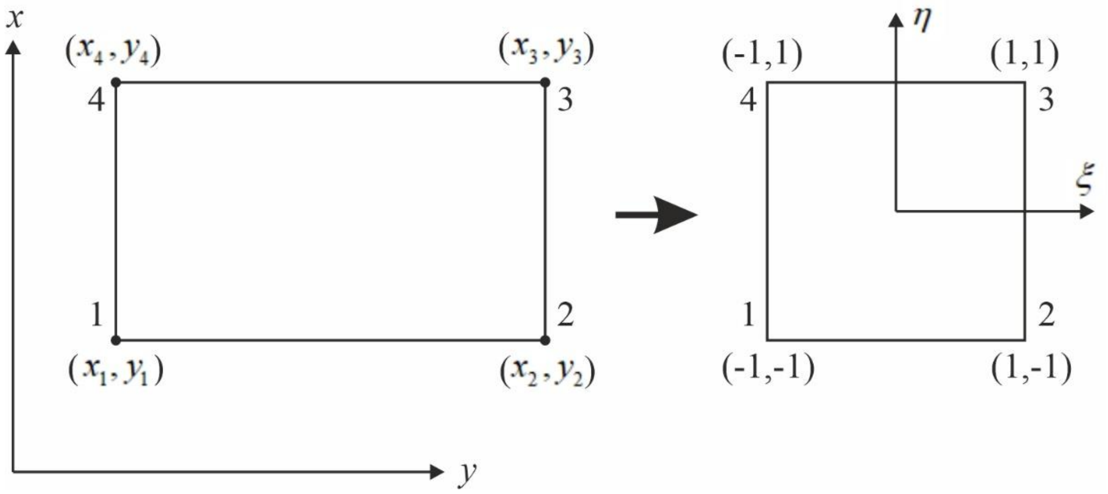

Figure 3.13. Geometric mapping process (Cartesian to natural coordinates transformation)

The spatial derivatives of a function *f(x,y)* in the Cartesian domain can be represented using natural coordinates as follows:

$$\frac{\partial f}{\partial x} = \frac{1}{J}\left(\frac{\partial y}{\partial \eta}\frac{\partial f}{\partial \xi} - \frac{\partial y}{\partial \xi}\frac{\partial f}{\partial \eta}\right) \tag{3.8}$$

$$\frac{\partial f}{\partial y} = \frac{1}{J}\left(\frac{\partial x}{\partial \xi}\frac{\partial f}{\partial \eta} - \frac{\partial x}{\partial \eta}\frac{\partial f}{\partial \xi}\right) \tag{3.9}$$

where *J* denotes the determinant of the Jacobian matrix and is defined as follows:

$$J = \frac{\partial x}{\partial \xi}\frac{\partial y}{\partial \eta} - \frac{\partial y}{\partial \xi}\frac{\partial x}{\partial \eta} \tag{3.10}$$

3.4.2. Generalized Differential Quadrature (GDQ) Method

In the early 1970s, Bellman and Casti [153], followed by Bellman et al. [101], introduced an efficient numerical approach known as the DQM. This method extended the well-established concept of integral quadrature to the computation of derivatives [154]. A key advantage of DQM is its ability to produce accurate results using fewer grid points compared to the widely used FEM. However, the initial applications of DQM were limited in terms of the number of grid points that could be used, and the method was not well-suited for calculating higher-order derivatives. A fundamental aspect of the DQM is the evaluation of weighting coefficients, similar to the approach used in integral quadrature methods. In its original form, these coefficients were obtained by solving an algebraic system, which became ill-conditioned when the number of grid points exceeded 13. While DQM offered the flexibility of arbitrary grid point selection, it was primarily applied to first-order derivative calculations. Later, Bellman and his collaborators proposed an improved version in which the weighting coefficients could be computed without solving an algebraic system. However, this version required the grid points to be distributed according to the roots of shifted Legendre polynomials.

Shu [102] later introduced an enhanced version of the DQM, known as the GDQ method. The GDQ method offers greater flexibility than the original DQM, as it allows for an arbitrary number and distribution of grid points. Moreover, higher-order derivatives can be efficiently computed using recursive formulations. The following section outlines the detailed formulation of the GDQ method.

The GDQ method is employed to compute the spatial derivatives of the field variables in the motion equation. The discretization of the plate domain into grid points is illustrated in Figure 3.14. In the GDQ framework, the *r*-th order derivative of a function $f(\xi)$ at a discrete point is expressed as a linear weighted sum of the function values at all grid points within the domain [155], and is formulated as follows:

$$\left(\frac{\partial f^{r}(x)}{\partial \xi^{r}}\right)_{\xi_i} = \sum_{j=1}^{n} \bar{C}_{ij}^{(r)} f_j \tag{3.11}$$

Here, n represents the total number of grid points, and ξ denotes the corresponding discrete locations. f_j refers to the function values at the grid points, while $\bar{C}_{ij}^{(r)}$ are the weighting coefficients associated with the *r*-th order derivative, calculated using Lagrange polynomial functions. For the case of a first-order derivative (r=1), the weighting coefficients can be defined as follows:

$$C_{ij}^{(1)} = \frac{\Phi(\xi_i)}{(\xi_i - \xi_j)\Phi(\xi_j)} \quad (i \neq j) \tag{3.12}$$

where

$$\Phi(\xi_i) = \prod_{j=1}^{n} (\xi_i - \xi_j) \qquad (i \neq j) \tag{3.13}$$

Higher-order derivatives can be computed using the following recursive relations:

$$\bar{C}_{ij}^{(r)} = r\left[\bar{C}_{ii}^{(r-1)}\bar{C}_{ij}^{(1)} - \frac{\bar{C}_{ij}^{(r-1)}}{(\xi_i - \xi_j)}\right] \qquad (i \neq j) \tag{3.14}$$

$$\bar{C}_{ii}^{(r)} = -\sum_{\substack{j=1 \\ i \neq j}}^{n} \bar{C}_{ij}^{(r)} \tag{3.15}$$

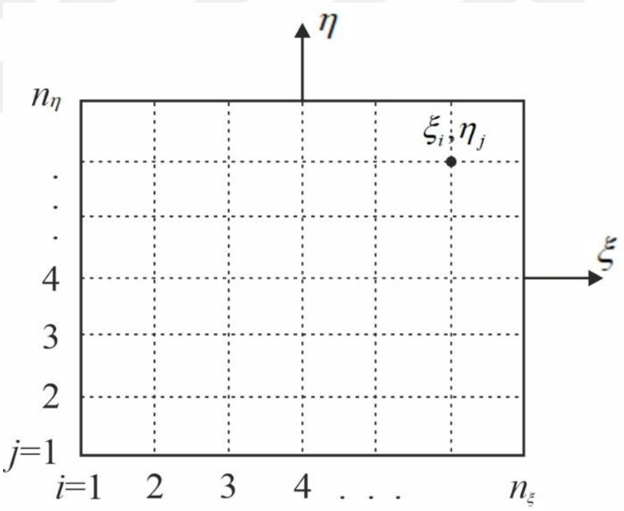

Figure 3.14. Discretization of plate domain in natural coordinate system

Partial derivatives can be evaluated using the GDQ method by extending the one-dimensional formulation to a two-dimensional domain. At an arbitrary grid point (ξ_i, η_j) within the discretized domain (as shown in Figure 3.14), the partial derivatives are computed as follows:

$$\left(\frac{\partial f^{r}(\xi,\eta)}{\partial \xi^{r}}\right)_{\xi_i,\eta_j} = \sum_{k=1}^{n_x} \bar{C}_{ik}^{(r)} f_{kj} \tag{3.16}$$

$$\left(\frac{\partial f^{s}(\xi,\eta)}{\partial \eta^{s}}\right)_{\xi_i,\eta_j} = \sum_{m=1}^{n_y} \bar{C}_{jm}^{(s)} f_{im} \tag{3.17}$$

$$\left(\frac{\partial f^{(r+s)}(\xi,\eta)}{\partial \xi^{r}\partial \eta^{s}}\right)_{\xi_i,\eta_j} = \frac{\partial^{r}}{\partial \xi^{r}}\left(\frac{\partial^{s} f}{\partial \eta^{s}}\right) = \sum_{k=1}^{n_x} \bar{C}_{ik}^{(r)} \sum_{m=1}^{n_y} \bar{C}_{jm}^{(s)} f_{km} \tag{3.18}$$

where, r and s indicate the orders of the partial derivatives, while n_ξ and n_η represent the number of grid points in the ξ and η directions, respectively.

Derivatives in Cartesian coordinates can be expressed in terms of derivatives with respect to natural coordinates as follows:

$$\left(\frac{\partial f}{\partial x}\right)_{ij} = \frac{1}{J_{ij}}\left[\left(\frac{\partial y}{\partial \eta}\right)_{ij}\left(\sum_{k=1}^{n_x} \bar{C}_{ik}^{(1)} f_{kj}\right) - \left(\frac{\partial y}{\partial \xi}\right)_{ij}\left(\sum_{m=1}^{n_y} \bar{C}_{jm}^{(1)} f_{im}\right)\right] \tag{3.19}$$

$$\left(\frac{\partial f}{\partial y}\right)_{ij} = \frac{1}{J_{ij}}\left[\left(\frac{\partial x}{\partial \xi}\right)_{ij}\left(\sum_{m=1}^{n_y} \bar{C}_{jm}^{(1)} f_{im}\right) - \left(\frac{\partial x}{\partial \eta}\right)_{ij}\left(\sum_{k=1}^{n_x} \bar{C}_{ik}^{(1)} f_{kj}\right)\right] \tag{3.20}$$

In this thesis, the Gauss-Lobatto quadrature rule is adopted for calculating the spatial derivatives of field variables, primarily because it generates grid points with non-uniform spacing. This rule places grid points at the domain boundaries, which facilitates the straightforward implementation of boundary conditions. Offering a balance between computational accuracy and ease of boundary condition application. The Gauss-Lobatto points x_i within the interval [-1,1] are determined by computing the roots of the following expression:

$$\frac{d\left[P_{n-1}(x_i)\right]}{dx} = 0 \qquad for\ \ i = 2,.....,(n-1) \tag{3.21}$$

where n represents the number of integration points in the x direction. $P_n(x)$ denotes the Legendre polynomial of degree n, which can be explicitly defined using Rodrigues' formula as follows:

$$P_n(x) = \frac{1}{2^n n!}\frac{d^n}{dx^n}\left((x^2-1)^n\right) \tag{3.22}$$

The first few Legendre polynomials can be computed as follows:

$$P_0(x) = 1 \tag{3.23}$$

$$P_1(x) = x \tag{3.24}$$

$$P_2(x) = \frac{1}{2}\left(3x^2-1\right) \tag{3.25}$$

$$P_3(x) = \frac{1}{2}\left(5x^3-3x\right) \tag{3.26}$$

$$P_4(x) = \frac{1}{8}\left(35x^4-30x^2+3\right) \tag{3.27}$$

The non-uniform grid points of the Lobatto rule in natural coordinates ($-1 \le \xi_i \le 1$) are defined for the curved beams as follows:

$$\xi_i = -1, \quad \xi_n = 1 \tag{3.28}$$

where $\xi_i (i = 2, ..., n-1)$ corresponds to the (i-1)th zero of

$$\frac{dP_{n-1}(\xi)}{d\xi} = 0 \tag{3.29}$$

Laminated curved beams are discretized using grid points, as illustrated in Figure 3.15, to identify the locations where the derivatives and field variable values will be computed.

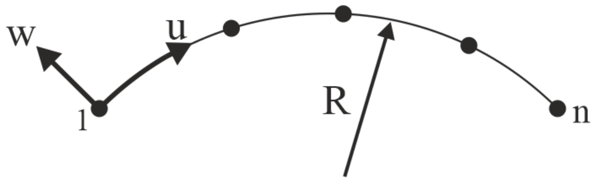

Figure 3.15. Grid points on curved beam

3.4.3. Solution of Free Vibration Equations

3.4.3.1. Free Vibration of Laminated Composite Curved Beams

By applying the virtual work equation given in Equation (2.12), the equation of motion can be formulated in matrix form as follows:

$$\mathbf{M}\ddot{\mathbf{U}} + \mathbf{K}\mathbf{U} = 0 \tag{3.30}$$

where **M** is the mass matrix, $\ddot{\mathbf{U}}$ is acceleration, **K** is the linear stiffness matrix, and **U** is the displacement vector. In the context of free vibration analysis, the displacement field is assumed to vary harmonically in time as:

$$\mathbf{U}(x,t) = \Phi(x)e^{i\omega t} \tag{3.31}$$

Substituting into the governing equation yields the standard eigenvalue problem:

$$(\mathbf{K} - \omega^2\mathbf{M})\Phi = 0 \tag{3.32}$$

where ω is the natural frequency and Φ is the corresponding mode shape vector. The stiffness matrix **K** in the linear regime includes only material contributions and is given by:

$$\mathbf{K} = \int_0^L \left[N_d^T B_b^T A_{mat} B_b N_d + N_d^T B_s^T A_{smat} B_s N_d \right] dx \tag{3.33}$$

Where B_b and B_s are the strain-displacement matrices for normal bending and shear deformation, respectively, as defined in Equations (3.34 and 3.35). And the A_{mat} and A_{mats} matrices contain the extensional bending and shear stiffness coefficients of the laminate.

$$B_b = \begin{bmatrix} 0 & \frac{1}{R} & 0 & 1 & 0 & 0 \\ 0 & 0 & 0 & 0 & 0 & 1 \end{bmatrix} \tag{3.34}$$

$$B_s = \begin{bmatrix} 0 & 0 & 0 & 0 & 0 & 0 \\ 0 & \frac{\theta_x}{R} & 0 & 0 & 0 & 0 \\ 0 & 0 & \frac{\partial \theta_x}{\partial x} & 0 & 0 & \theta_x \end{bmatrix} \tag{3.35}$$

3.4.3.2. *Free Vibration of Laminated Composite Plates*

In the case of vibrational behavior, unknown displacements $\mathbf{U}$ can be expressed as a harmonic function of $\mathbf{U} = \bar{\mathbf{U}} \sin \omega t$, where ω is the natural frequency, and $\bar{\mathbf{U}}$ is the amplitude of vibration. When $\mathbf{U} = \bar{\mathbf{U}} \sin \omega t$ is substituted into Equation (2.55) by considering $\mathbf{K} = \mathbf{K}_0 + \mathbf{K}_1(\mathbf{U}) + \mathbf{K}_2(\mathbf{U}^2)$ expression, the following equation is obtained.

$$-\omega^2 \mathbf{M}\bar{\mathbf{U}} \sin \omega t + \left(\mathbf{K}_0 + (\sin \omega t)\mathbf{K}_1(\bar{\mathbf{U}}) + (\sin \omega t)^2 \mathbf{K}_2(\bar{\mathbf{U}}^2)\right)\bar{\mathbf{U}} \sin \omega t = 0 \tag{3.36}$$

Equation (3.36) has a time dependency. Time dependency can be easily removed by applying time integration over a period of time. If Equation (3.36) is integrated in time after scaling by $\sin \omega t$ over a quarter of the time period, the following simplified equation is obtained.

$$\left[-\omega^2 \mathbf{M} + \left(\underbrace{\mathbf{K}_0 + \frac{8}{3\pi}\mathbf{K}_1\left(\bar{\mathbf{U}}\right) + \frac{3}{4}\mathbf{K}_2\left(\bar{\mathbf{U}}^2\right)}_{\mathbf{K}}\right)\right]\bar{\mathbf{U}} = 0 \tag{3.37}$$

Equation (3.37) corresponds to a nonlinear eigenvalue problem, the solution of which yields an eigenvalue (natural frequency) of ω and an eigenvector (mode shapes) of $\bar{\mathbf{U}}$. Equation (3.37) can be solved with a direct iteration approach by carefully selecting an initial solution. In nonlinear vibration problems, scaled values of linear mode shapes are commonly used as the initial solution. The solution of Equation (3.37) can be summarized as follows:

1- Firstly, the linear-free vibration problem $\left[-\omega^2\mathbf{M}+\mathbf{K}\right]\bar{\mathbf{U}}=0$ (by omitting the nonlinear terms of $\mathbf{K}_1$ and $\mathbf{K}_2$ in Equation (3.37)) is solved to obtain the linear frequency ω and corresponding mode shape $\bar{\mathbf{U}}$ by utilizing any standard eigenvalue extraction algorithm.

2- The linear mode shape $\bar{\mathbf{U}}$ in the first iteration (updated nonlinear mode shape $\bar{\mathbf{U}}$ in further iterations) is then normalized (scaled) so as to yield the maximum transverse displacement (i.e. amplitude) of $w_{\max}$ (or $w_{\max}/h$ ratio, *h* is the thickness of the plate) specified in the nonlinear vibration. After normalization of the mode shape, the nonlinear stiffness matrix $\mathbf{K}=\mathbf{K}_0+\frac{8}{3\pi}\mathbf{K}_1+\frac{3}{4}\mathbf{K}_2$ is updated by recalculating $\mathbf{K}_1$ and $\mathbf{K}_2$ terms.

3- Using the new value of the nonlinear stiffness matrix $\mathbf{K}$, the vibration equation of $\left[-\omega^2\mathbf{M}+\mathbf{K}\right]\bar{\mathbf{U}}=0$ is resolved to obtain the updated values of nonlinear frequency ω and mode shape $\bar{\mathbf{U}}$.

4- Steps 2 and 3 are repeated until the nonlinear frequency and mode shape converge.

The detailed solution procedure is also presented in Figure 3.16.

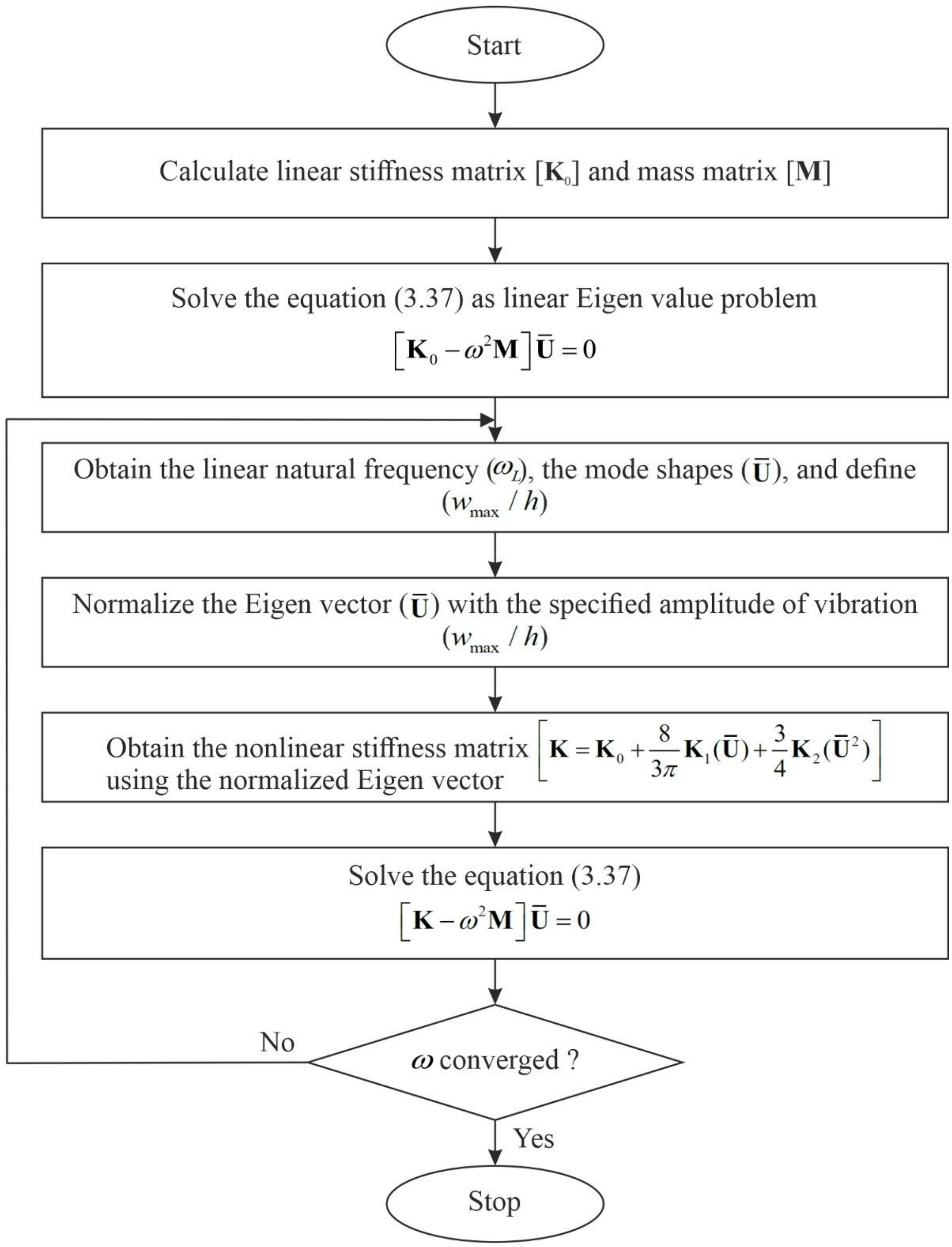

Figure 3.16. Flow chart of the solution procedure

4. ANALYSIS AND DISCUSSION

4.1. Tensile Test Results

Tensile tests were conducted to assess the mechanical properties of composites reinforced with pure carbon, pure glass, and pure hemp fibers. In Table 4.1, mechanical properties obtained from tensile tests of the carbon, glass, and hemp fiber-reinforced composites are presented. E_1, E_2, G_{12}, ν_{12}, and ρ stand for the longitudinal elastic modulus, transverse elastic modulus, shear modulus, Poisson's ratio, and density, respectively. Since plain woven bidirectional carbon, glass, and hemp fabrics were used, the values E_1 and E_2 are identical.

Table 4.1. Mechanical properties of carbon, glass, and hemp fiber-reinforced composites

Material	E_1 (Gpa)	E_2 (Gpa)	G_{12} (Gpa)	ν_{12}	ρ (kg/m^3)
Carbon/Epoxy	57.4	57.4	23.3	0.23	1360
Glass/Epoxy	16.4	16.4	6.7	0.19	1600
Hemp/Epoxy	8.4	8.4	3.4	0.39	1190

4.2. Experimental Vibration Test Results

In this section, experimental vibration test results of laminated composite straight beams are presented. Pure and hybrid forms of the composite beams can be seen in Figure 4.1. All specimens were manufactured to maintain a consistent thickness, and the thickness values of each layer are indicated in Table 4.2. A total thickness value of 2.2 ± 0.05 mm for each specimen was achieved. Cross-ply laminated composite beam specimens have a total length of 340 mm, and they were mounted on the fixed end of the vibration test device as 300 mm length cantilever beams. Then the data were collected and further analyses were carried out to obtain the damping ratio and the natural frequency values. In Figures 4.3-4.5, time-displacement and frequency domain graphs of composite beams are also presented.

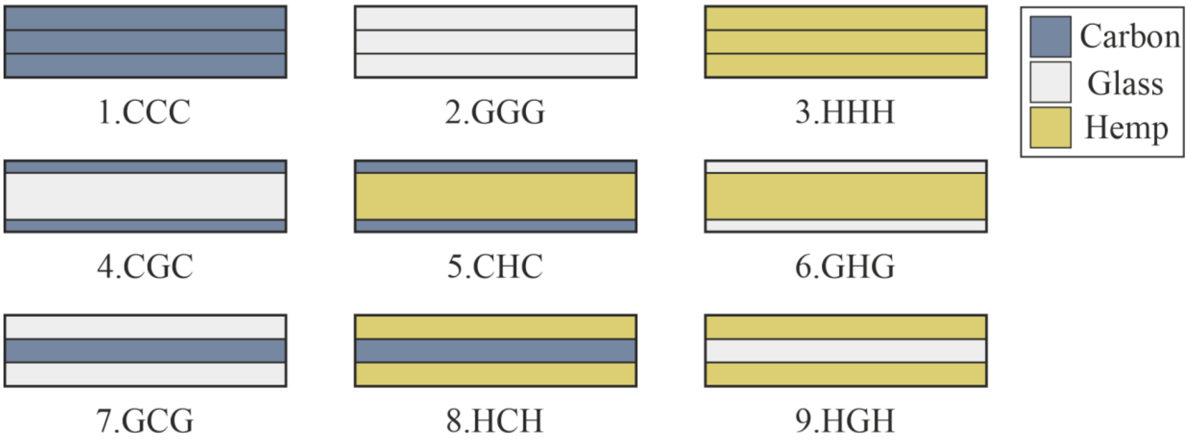

Figure 4.1. Stacking sequences of laminated composite beams tested experimentally

Table 4.2. Layer thickness values of the test specimens

	Mat.	Thick.		Mat.	Thick.		Mat.	Thick.
	C	0.7200 mm		G	0.7332 mm		H	0.7333 mm
1	C	0.7200 mm	2	G	0.7332 mm	3	H	0.7333 mm
	C	0.7200 mm		G	0.7332 mm		H	0.7333 mm
	C	0.3600 mm		C	0.3600 mm		G	0.3666 mm
4	G	1.4664 mm	5	H	1.4666 mm	6	H	0.7333 mm
	C	0.3600 mm		C	0.3600 mm		G	0.3666 mm
	G	0.7332 mm		H	0.7333 mm		H	0.7333 mm
7	C	0.7200 mm	8	C	0.7200 mm	9	G	0.7332 mm
	G	0.7332 mm		H	0.7333 mm		H	0.7333 mm

In Table 4.3, damping ratios, experimental natural frequency values, and natural frequency values based on the GDQ method with and without tip mass effect are presented. These results indicate only fundamental natural frequency values of the nine cantilever beams. After obtaining the experimental frequency values, numerical analyses were also carried out to compare experimental and numerical results and validate the efficiency of the GDQ method. Since the vibration test specimens have metal sheets at the free end for the magnetic sensor, the tip mass effect was taken into account while carrying out the GDQ method analyses. Numerical results without the tip mass effect are also presented in the table. Results indicate that the pure hemp composite beam has the highest damping ratio value, while the pure carbon composite has the lowest. These results agree well with the studies of Jalili et al. for pure carbon, pure glass, and pure hemp fiber-reinforced composite beams [90], [91]. The stacking sequence has a very dominant effect on the damping ratios. The stacking sequences in which hemp fiber is located at the top and bottom layers (HCH and HGH) have higher damping ratio values compared to composites in which hemp fiber is located at the middle layer (CHC and GHG). For HCH and HGH configurations, the damping ratio values are very close to those of pure hemp composite. It can be seen that the outer layer fiber material has a more significant effect on damping ratios, and this situation is also stated in an earlier study by Pinto et al. [73].

In Figure 4.2, experimental fundamental mode natural frequency values of the nine test specimens are presented, and these results are compared with GDQ method results. As can be seen from the figure, experimental and GDQ method results are compatible with each other. To see the tip mass effect on the test specimens, GDQ analysis results without tip mass were also presented. Since the highest density material is glass fiber and the lowest one is hemp fiber, glass fiber-reinforced composites were the least affected ones from tip mass, while hemp fiber-reinforced composites were the most affected. Comparing test specimens' frequency values, the highest value is observed for the pure carbon composite beam (CCC) as expected. On the other hand, although pure hemp fiber-reinforced composite (HHH) has the lowest frequency value, hybridizing hemp fiber with carbon fiber has an increasing effect on the frequency parameter. The CHC composite beam has a slightly higher frequency value than the CGC composite beam, and the second-highest natural frequency value after the CCC one. Besides, regardless of the stacking sequences, hybridizing the lower mechanical property fiber material with a higher one has an increasing effect on the natural frequency values. Consequently, the experimental vibration analysis results of straight beams indicate great similarity with the vibration analysis results of straight and curved beams in the parametric analysis section.

Table 4.3. Experimental vibration test results of the straight beams

	Damping Ratio (ζ)	Experimental Frequency (Hz) ω_D	Experimental Frequency (Hz) ω_n	GDQ (With tip mass)	GDQ (Without tip mass)
1. CCC	0.00174	15.9994	15,9994	15.6182	25.2672
2. GGG	0.00289	8.7881	8,7881	8.6140	12.6670
3. HHH	0.00896	6.6785	6,6788	6.4867	10.8263
4. CGC	0.00269	13.5552	13,5552	13.1844	20.9559
5. CHC	0,00276	13.9979	13,9980	13.6674	22.5547
6. GHG	0.00369	8.5447	8,5448	8.3282	13.1041
7. GCG	0.00271	9.1930	9,1930	8.9911	13.4836
8. HCH	0.00771	7.7279	7,7281	7.5093	11.4570
9. HGH	0.00825	6.9959	6,9961	6.7679	10.3667

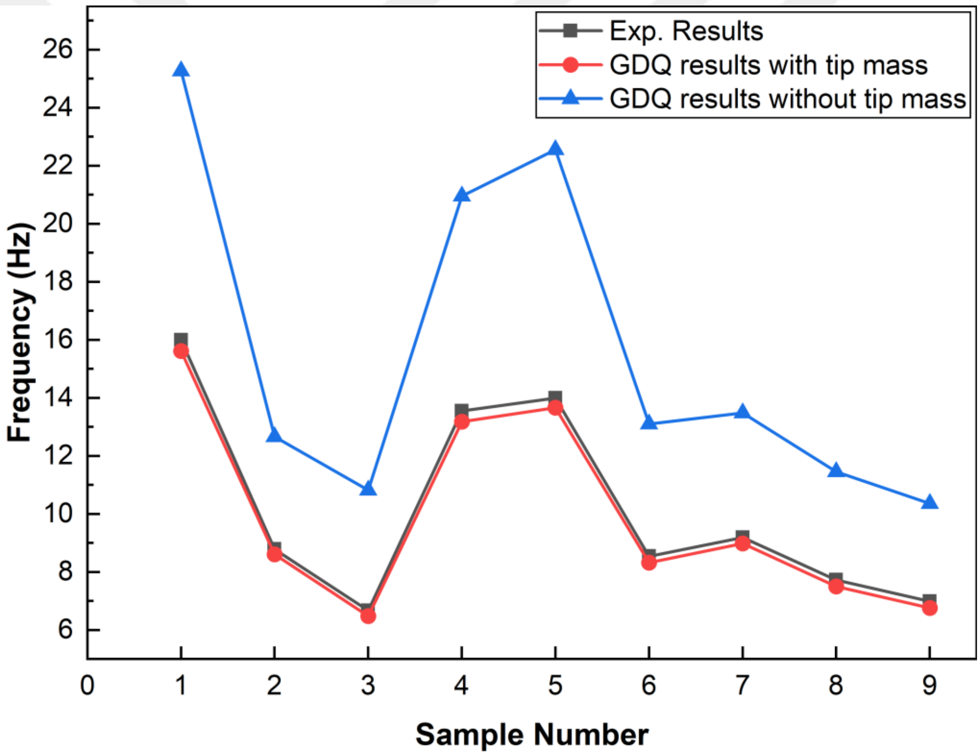

Figure 4.2. Experimental and GDQ frequency results of the test specimens

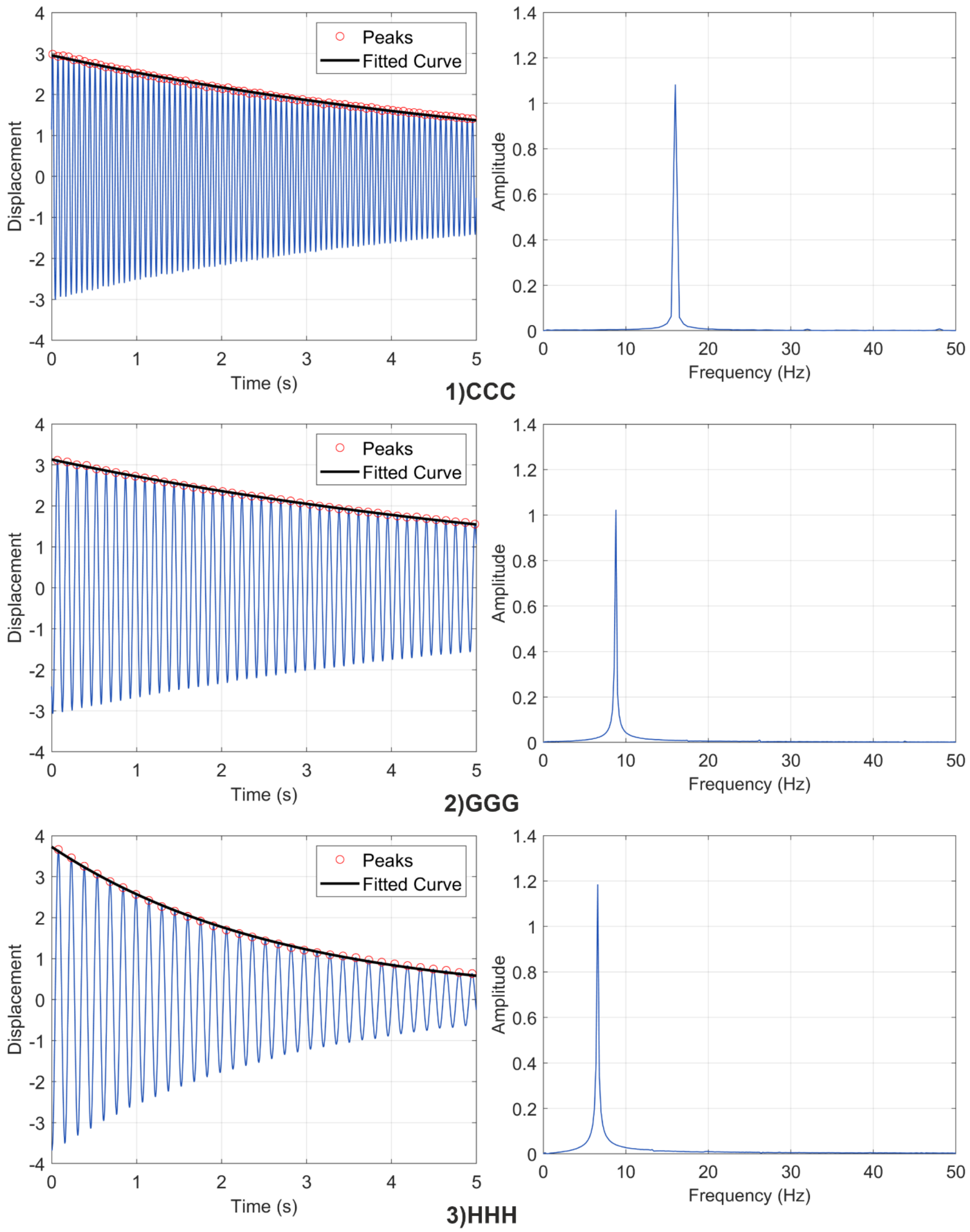

Figure 4.3. Time-displacement and Frequency domain graphs of composite beams

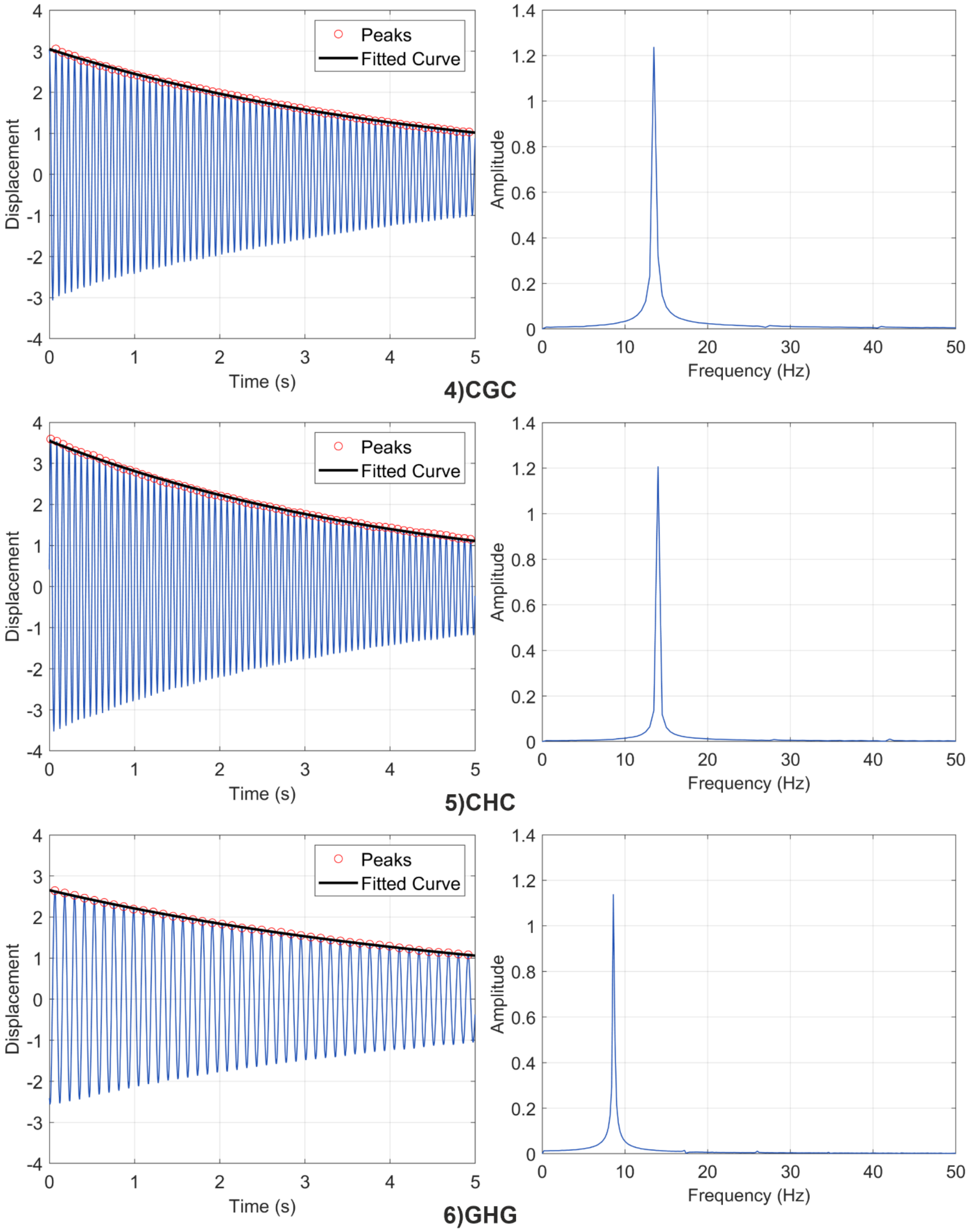

Figure 4.4. Time-displacement and Frequency domain graphs of composite beams

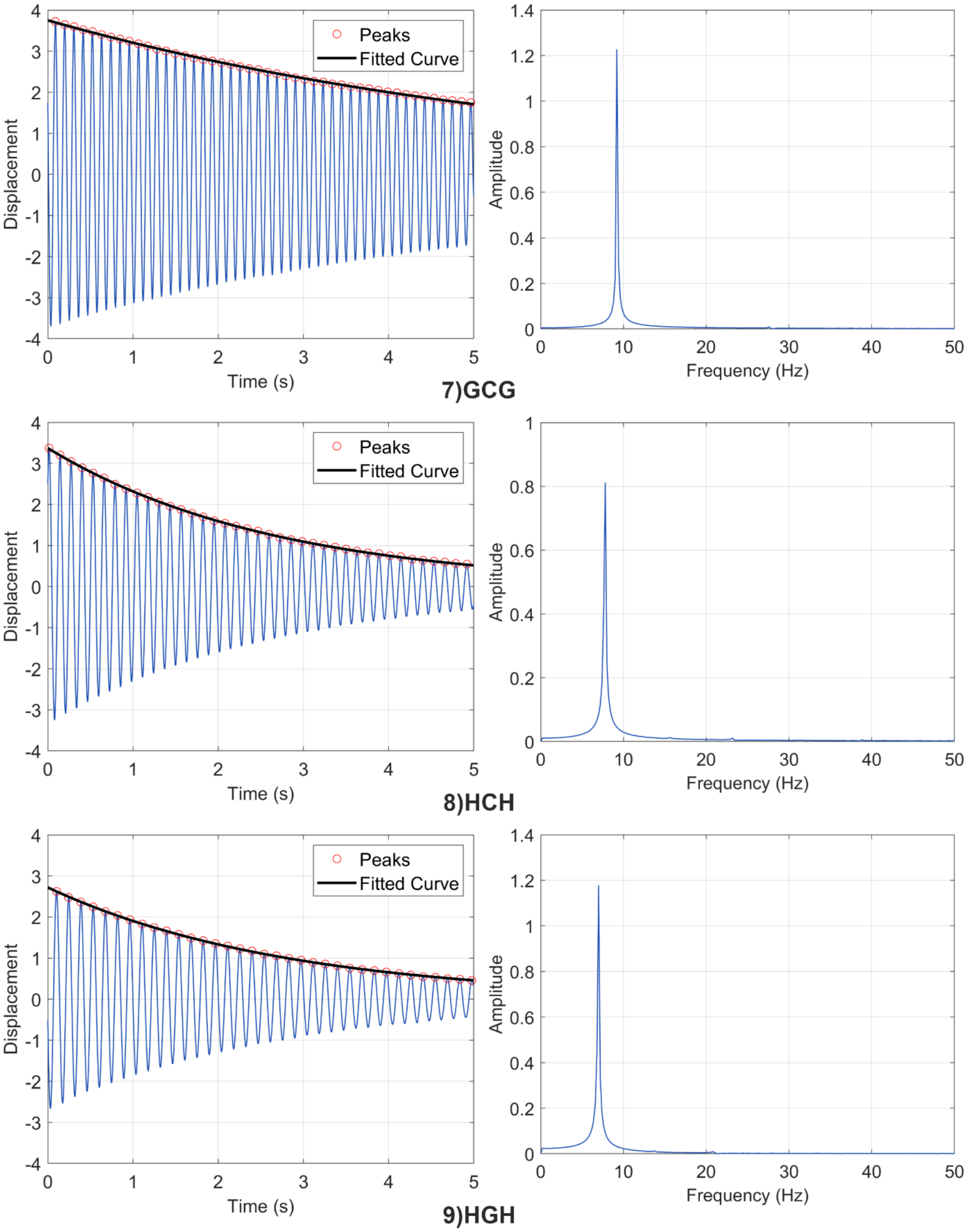

Figure 4.5. Time-displacement and Frequency domain graphs of composite beams

4.3. Free Vibration Results of Curved Beams

4.3.1. Validation Studies of Curved Beams

In order to check the validity of the proposed formulations and programming, in-plane free vibration studies of curved beams available in the literature were analyzed in this section. In Table 4.4, dimensionless frequency parameters $\Omega = \omega a^2 \sqrt{12\rho / E_1 h^2}$ of laminated composite curved beams are presented for different fiber orientation angles and curvature ratios (a/R). The geometry and material properties of the curved beams are $a=1$ m, $b=0.025$ m, $h=0.05$ m, $E_1=138$ Gpa, $E_2=8.96$ Gpa, $G_{12}=7.1$ Gpa, $G_{13}=G_{23}=3.3$ Gpa, $v_{12}=0.3$, $\rho=1580$ kg/m^3, and the curvature ratios are given as a/R=0.2, 0.6, and 1. As can be seen from the table, the present results are compatible with the exact solutions and FEM results presented in Ref. [124].

Table 4.4. Comparison of the frequency parameters Ω for clamped-clamped curved beams

Mode	$[0°,0°,0°,0°]$								
	$a/R=0.2$			$a/R=0.6$			$a/R=1$		
	FSDT (E_x) [124]	3D FEM [124]	Present	FSDT (E_x) [124]	3D FEM [124]	Present	FSDT (E_x) [124]	3D FEM [124]	Present
1	21.72	21.76	22.06	38.67	38.68	38.89	40.56	40.79	42.02
2	42.42	42.70	43.94	41.78	42.04	43.28	53.54	53.74	54.42
3	71.69	72.40	74.84	73.45	74.08	76.46	80.71	81.07	82.94
4	102.8	104.1	107.89	102.2	103.5	107.25	101.0	102.3	106.04
5	135.7	137.4	142.64	135.3	137.4	142.62	136.0	137.6	142.77
	$[0°,90°,90°,0°]$								
	$a/R=0.2$			$a/R=0.6$			$a/R=1$		
	FSDT (E_x) [124]	3D FEM [124]	Present	FSDT (E_x) [124]	3D FEM [124]	Present	FSDT (E_x) [124]	3D FEM [124]	Present
1	19.49	19.62	19.80	30.70	30.79	30.89	39.31	39.82	40.63
2	41.13	41.70	42.52	40.50	41.05	41.87	43.54	43.70	43.84
3	69.91	71.16	72.85	70.60	71.80	73.48	73.04	74.08	75.64
4	100.8	103.0	105.67	100.1	102.2	104.91	98.89	100.9	103.54
5	133.6	135.9	140.24	133.1	136.3	140.08	132.9	136.0	139.81
	$[0°,0°,90°,90°]$								
	$a/R=0.2$			$a/R=0.6$			$a/R=1$		
	FSDT	3D FEM	Present	FSDT	3D FEM	Present	FSDT	3D FEM	Present

	(E_x) [124]	[124]		(E_x) [124]	[124]		(E_x) [124]	[124]	
1	13.07	13.09	13.17	26.04	26.37	26.27	24.50	25.04	25.73
2	25.90	25.75	26.44	25.35	25.57	26.36	35.85	36.60	37.13
3	47.62	47.01	48.84	48.86	48.84	50.56	54.92	55.55	56.52
4	72.80	71.55	75.13	71.94	71.58	75.17	70.76	71.22	74.79
5	101.0	98.80	104.59	100.5	99.37	105.19	100.3	100.1	105.94
	$[45°, 45°, 45°, 45°]$								
	$a/R = 0.2$			$a/R = 0.6$			$a/R = 1$		
	FSDT (E_x) [124]	3D FEM [124]	Present	FSDT (E_x) [124]	3D FEM [124]	Present	FSDT (E_x) [124]	3D FEM [124]	Present
1	8.285	8.350	8.31	13.60	13.69	13.61	18.69	18.83	18.82
2	19.49	19.64	19.63	19.21	19.36	19.35	19.86	19.98	19.89
3	36.74	37.01	37.16	36.96	37.23	37.37	37.69	37.96	38.06
4	57.83	58.19	58.73	57.31	57.70	58.19	56.42	56.85	57.28
5	82.20	82.60	73.48	82.05	82.80	74.61	81.86	82.32	76.64
	$[30°, 30°, 60°, 60°]$								
	$a/R = 0.2$			$a/R = 0.6$			$a/R = 1$		
	FSDT (E_x) [124]	3D FEM [124]	Present	FSDT (E_x) [124]	3D FEM [124]	Present	FSDT (E_x) [124]	3D FEM [124]	Present
1	8.709	8.842	8.73	14.82	15.11	14.82	19.41	19.65	19.58
2	20.11	20.36	20.27	19.90	20.14	20.06	21.77	22.19	21.77
3	37.81	38.29	38.28	38.22	38.68	38.69	39.32	39.82	39.74
4	59.36	59.96	60.36	59.09	59.67	60.10	58.46	59.02	59.44
5	84.10	84.82	81.27	84.22	84.92	82.09	84.27	84.96	83.99

Another validation study was carried out for a two-layered, unsymmetrically laminated $[90°, 0°]$ curved beam with different boundary conditions and presented in Table 4.5. The material properties are given as $E_1 = 150$ Gpa, $E_2 = 10$ Gpa, $G_{12} = G_{13} = G_{23} = 5.5$ Gpa, $v_{12} = 0.3$, and $\rho = 1700$ kg/m^3. The geometric properties are defined as $h/a = 0.01$, $r/a = 2$, $h = 0.1$ m. From the table, it is seen that the present results agree well with the exact solutions published by Qatu [156] and with the FSDT results published by Ye et al. [157].

Table 4.5. Comparison of the frequency parameters Ω for a $[90°, 0°]$ laminated curved beam with different boundary conditions.

Boundary Conditions	Method	Mode Number					
		1	2	3	4	5	6
S-S	CBT [156]	18.434	37.935	74.549	99.888	143.10	169.68
	FSDT [157]	18.775	38.574	75.663	98.916	140.03	169.43
	Present	18.413	37.848	74.203	99.490	142.34	166.12
C-C	CBT [156]	29.015	51.348	94.637	111.64	149.21	198.58
	FSDT [157]	29.008	51.122	94.195	107.63	146.89	195.53
	Present	28.928	51.087	93.887	111.30	147.79	194.75

To further prove the validity of the present method, in Table 4.7, three-layered circular sandwich beams with aluminum face layers and soft foam core vibration results are presented. In this example, the effects of various boundary conditions were considered, such as both ends clamped (C-C), both ends simply supported (S-S), and clamped free (C-F). Present results are compared with both the GDQ method and FEM results in Refs. [128], [129], [158]. The material properties and the relevant dimensions of the curved beam are presented in Table 4.6. As can be seen in Table 4.7, there are slight differences between previous results. However, the present results are consistent with the previous ones. These slight differences can be attributed to the different methodologies employed in the solution procedure.

Table 4.6. Material properties and dimensions of sandwich beams

Face layers (Layers 1 and 3)	
Young's modulus	$E_1 = E_3 = 68.9\,\text{Gpa}$
Density	$\rho_1 = \rho_3 = 2680\,\text{kg/m}^3$
Thickness	$h_1 = h_3 = 0.4572\,\text{mm}$
Poisson's ratio	$v_1 = v_2 = 0.28$
Core layer (Layer 2)	
Shear modulus	$G_2 = 82.68\ \text{Mpa}$
Density	$\rho_2 = 32.8\ \text{kg/m}^3$
Thickness	$h_2 = 12.7\ \text{mm}$
Whole beam	
Length	$a = 711.2\ \text{mm}$
Midsection radius	$R_{mid} = 4.263\,\text{m}$

Table 4.7. The natural frequencies (Hz) of the circular sandwich beam for various boundary conditions

S-S	Mode Number							
	1	2	3	4	5	6	7	8
GDQ[128]	185.65	352.35	726.00	1158.31	1623.55	2099.75	2579.76	3057.69
FEM[128]	186.12	352.62	726.98	1160.5	1627.2	2105.0	2586.4	3065.6
GDQ[129]	186.22	352.35	726.05	1158.32	1623.59	2099.80	2579.84	3057.79
FEM[129]	186.00	353.03	727.49	1160.82	1627.13	2104.35	2585.20	3063.76
Ref. [158]	182.7	351.4	726.1	1162	1633	2118	2611	3104
Present	182.74	350.36	722.45	1153.56	1617.85	2093.28	2572.58	3049.68
C-C	Mode Number							
	1	2	3	4	5	6	7	8
GDQ[128]	247.10	486.38	859.07	1271.06	1714.09	2170.63	2636.16	3103.14
FEM[128]	247.64	487.64	860.41	1272.8	1716.3	2173.3	2639.3	3106.7
GDQ[129]	247.41	486.38	859.11	1271.10	1714.16	2170.72	2636.27	3103.32
FEM[129]	247.82	487.60	861.44	1274.79	1719.29	2177.27	2644.08	3112.13
Ref. [158]	244.6	485.6	859.8	1276	1725	2190	2668	3151
Present	244.33	483.60	854.10	1263.75	1704.22	2158.25	2621.35	3085.80
C-F	Mode Number							
	1	2	3	4	5	6	7	8
GDQ[128]	33.98	199.24	513.06	907.78	1349.05	1690.16	1816.79	2291.02
FEM[128]	34.02	199.47	513.65	908.83	1350.7	1691.6	1819.1	2294.1
GDQ[129]	33.98	199.24	513.07	907.80	1349.11	1696.02	1816.95	2291.11
FEM[129]	34.05	199.66	514.22	909.99	1352.52	1697.19	1821.57	2296.98
Ref. [158]	33.8	198.5	513	910	1356	1657	1831	2316
Present	33.76	198.04	510.17	902.96	1342.27	1655.62	1807.93	2280.76

In Table 4.8, natural frequency values for curved sandwich beams are presented with C-C boundary conditions. For this scenario, the material and geometric properties are all the same as presented in Table 4.6, except for the midsection radius. The midsection radius value is $R_{mid} = 0.57395$ m in this case. One of the primary advantages of the GDQ method is its computational efficiency, as it typically requires fewer nodes or grid points than other numerical methods. However, prior to implementing the GDQ method, it is typically necessary to conduct a mesh convergence study to identify the optimal number of grid points required to achieve accurate and reliable results. In the present study, 19 grid points were found to be sufficient for the convergence, as can be seen in Table 4.8.

Table 4.8. The natural frequencies (Hz) of the circular sandwich beam for C-C boundary conditions

	Mode Number							
	1	2	3	4	5	6	7	8
GDQ[129]	452.28	719.78	1234.51	1266.99	1750.22	2134.80	2626.82	3058.97
FEM[129]	456.04	724.69	1242.86	1270.62	1759.52	2146.85	2640.03	3072.85
GDQ[128]	455.16	722.79	1239.76	1266.21	1754.81	2141.01	2633.02	3064.62
FEM[128]	455.57	723.09	1240.4	1267.2	1755.9	2141.9	2634.0	3065.5
Ref. [158]	459.26	718.47	1200.11	1254.89	1764.60	2183.70	2696.03	3150.12
Present								
11 Grid	452.41	716.44	1232.95	1246.37	1749.83	2235.83	2731.67	3516.15
13 Grid	452.41	716.44	1232.12	1246.14	1742.19	2135.87	2625.80	3286.92
15 Grid	452.41	716.44	1232.11	1246.14	1741.95	2128.16	2617.58	3079.58
17 Grid	452.41	716.44	1232.11	1246.14	1741.95	2127.91	2617.46	3047.06
19 Grid	**452.41**	**716.44**	**1232.11**	**1246.14**	**1741.95**	**2127.91**	**2617.47**	**3044.68**
21 Grid	452.41	716.44	1232.11	1246.14	1741.95	2127.91	2617.47	3044.67

4.3.2. Parametric Study Results of Laminated Composite Curved Beams

In this section, a parametric study was carried out for curved beams to investigate the effects of hybridization, curvature ratio (a/R), stacking sequence, and boundary conditions on vibrational behavior. The geometrical properties of the curved beams were determined as $a=1$ m, $b=0.025$ m, $h=0.05$ m, and the material properties were presented in Table 4.1 previously. The fiber orientation of the plates was chosen to be cross-ply as $[0°,90°,0°,90°,0°]$ for all analyses, and the thickness of each layer was defined as 0.01 m. For the curved beam vibration analyses, 15 stacking sequences were determined, and they are presented in Figure 4.6. As can be seen from the figure, pure carbon, pure glass, pure hemp, and hybrid composites consisting of two different reinforcement materials were investigated. These 15 composite beams were given names based on their stacking sequences. C, G, and H stand for carbon, glass, and hemp layers, respectively. Natural frequency values of the straight and curved beams are presented in Tables 4.9-4.23 for six modes with clamped-free (C-F), simply supported (S-S), and clamped-clamped (C-C) boundary conditions, respectively. Straight beam results are presented to make a comparison with the curved beams. Vibration analyses were carried out for nine curvature ratios as a/R=0, 0.2, 0.4, 0.6, 0.8, 1, 1.2, 1.4, and $\pi/2$. However, to avoid presenting too much data, the results with curvature ratio values of 0, 0.4, 0.8, 1.2, and $\pi/2$ are presented as tables. The curvature ratio value of $\pi/2$ was chosen particularly because it represents a special case in curved beams, which is commonly encountered in structural applications. It is presented in Figure 4.7.

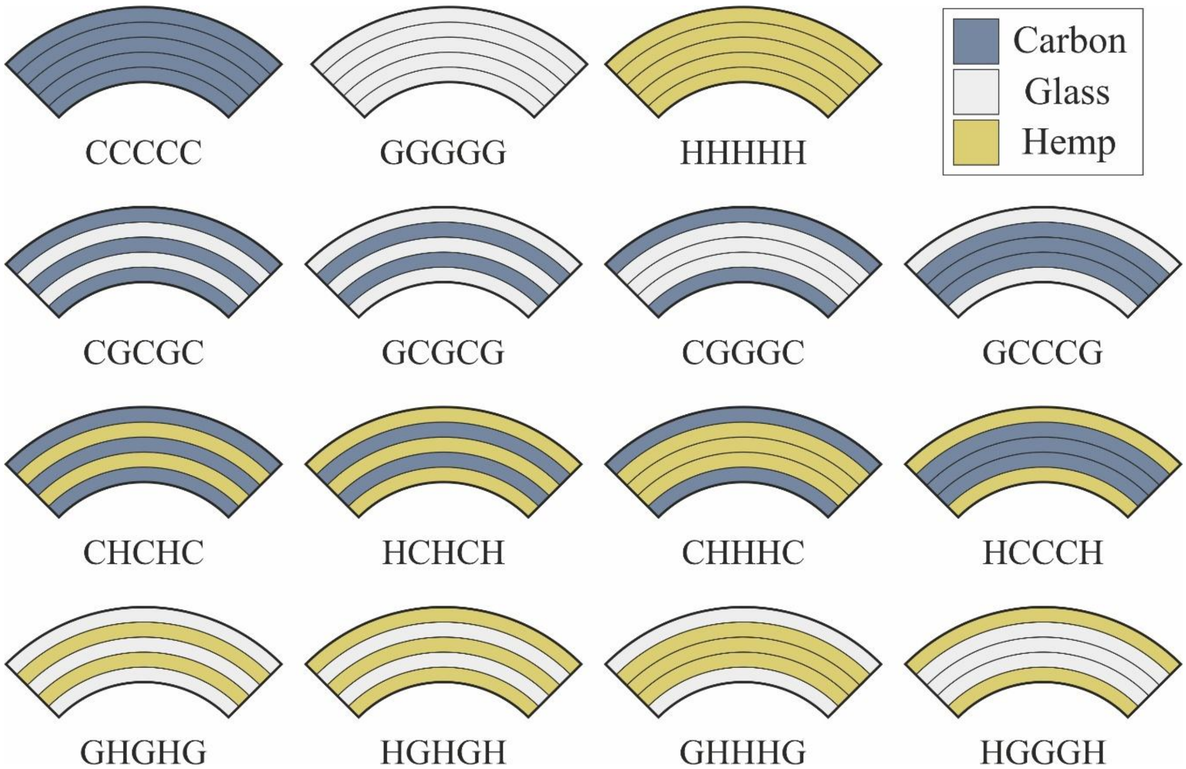

Figure 4.6. Stacking sequences of laminated composite curved beams

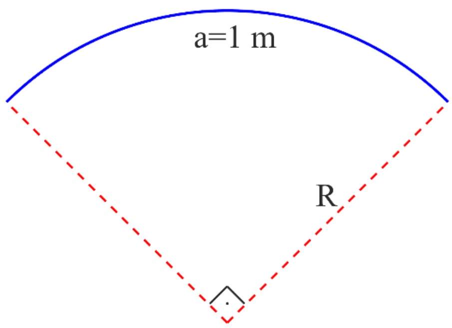

Figure 4.7. Curvature ratio of $a/R = \pi/2$

In Tables 4.9-4.13, natural frequency values of straight and curved beams are presented for different curvature ratios with C-F boundary conditions. It is seen that as the curvature ratio increases, the fundamental frequency values of beams increase. However, these increments are relatively small considering the increase in curvature ratio. Considering modes 2, 3, and 4, as the curvature ratio increases, the frequency values indicate a decrease. There is an increase in the fifth mode as the curvature ratio increases. On the other hand, the sixth mode indicates a decrease, for curvature ratios up to 0,8, then it increases with the curvature ratio. However, even though frequency values change with the curvature ratio, these changes are relatively small for the C-F boundary condition, especially for lower modes. In Figure 4.8, fundamental mode frequency values of beams with C-F boundary conditions are shown. The small increment can be seen from the figure as the curvature ratio increases. It is clearly seen that the highest natural frequency value is observed for the pure carbon composite beam (CCCCC) and the smallest one for the pure hemp composite beam (HHHHH). Although the pure hemp composite beam has the lowest natural frequency values, the hybridization of hemp fiber with carbon fiber has an increasing effect on natural frequency values for certain stacking sequences. Hybrid carbon/hemp composites with stacking sequences of CHHHC and CHCHC have the highest frequency values after the pure carbon CCCCC stacking sequences, respectively. The frequency values of CHHHC and CHCHC are even higher than those of the carbon/glass hybrid composites with stacking sequences of CGGGC and CGCGC. On the other hand, stacking sequences HCCCH and HCHCH have almost the same frequency values, but these values are lower compared to the frequency values of GCCCG and GCGCG stacking sequences. The GHHHG stacking sequence has almost identical frequency values to pure glass composite (GGGGG), and compared to pure hemp composite, there is a significant increase in frequency value. In general, placing the higher mechanical property fiber material on the outer layers has a favorable effect on increasing the natural frequency values, which is also stated in earlier studies [73], [159], [160].

Table 4.9. Natural frequency values of clamped-free straight beams (Hz), ($a / R = 0$)

Stacking Sequence	Mode Number 1	2	3	4	5	6
C C C C C	52.32	322.47	880.08	1624.15	1665.56	2642.00
G G G G G	25.79	159.00	434.22	800.39	822.44	1305.79
H H H H H	21.39	131.60	358.25	664.21	675.77	1068.13
C G C G C	46.64	286.72	779.67	1326.63	1468.65	2317.84
G C G C G	32.81	202.92	556.70	1060.72	1167.49	1695.30
C G G G C	45.71	279.91	757.02	1167.49	1416.36	2219.25
G C C C G	33.57	208.03	572.30	1094.38	1326.63	1756.30
C H C H C	48.65	298.83	811.51	1352.24	1526.15	2404.44
H C H C H	30.98	191.60	525.61	1001.36	1179.45	1600.18
C H H H C	49.05	299.55	806.91	1179.45	1502.44	2342.58
H C C C H	30.90	191.63	527.72	1010.53	1352.24	1624.28
G H G H G	25.79	158.77	432.55	757.97	816.75	1292.41
H G H G H	21.96	135.39	369.74	700.27	731.74	1111.72
G H H H G	26.50	162.75	442.05	731.74	831.51	1310.42
H G G G H	21.40	132.15	361.78	687.38	757.97	1098.91

Table 4.10. Natural frequency values of clamped-free curved beams (Hz), ($a / R = 0.4$)

Stacking Sequence	Mode Number 1	2	3	4	5	6
C C C C C	52.49	316.49	872.22	1609.88	1718.19	2640.78
G G G G G	25.87	156.05	430.34	794.20	847.54	1305.18
H H H H H	21.46	129.16	355.05	655.43	700.23	1067.68
C G C G C	46.79	281.37	772.35	1344.74	1482.69	2316.29
G C G C G	32.92	199.20	552.01	1049.14	1205.57	1695.32
C G G G C	45.85	274.62	749.34	1192.10	1421.09	2217.32
G C C C G	33.68	204.24	567.63	1086.04	1363.85	1757.49
C H C H C	48.81	293.24	803.79	1373.84	1537.54	2402.73
H C H C H	31.08	188.10	521.27	993.01	1213.85	1600.92
C H H H C	49.21	293.85	798.27	1206.88	1505.41	2340.32
H C C C H	31.01	188.14	523.51	1004.21	1385.63	1627.84
G H G H G	25.88	155.82	428.58	764.74	828.16	1291.64
H G H G H	22.03	132.89	366.54	689.45	759.50	1111.48
G H H H G	26.58	159.71	437.83	743.93	837.21	1309.47
H G G G H	21.47	129.72	358.72	679.89	782.67	1095.13

Table 4.11. Natural frequency values of clamped-free curved beams (Hz), ($a/R = 0.8$)

Stacking Sequence	Mode Number					
	1	2	3	4	5	6
C C C C C	53.01	300.74	851.91	1592.98	1840.17	2638.48
G G G G G	26.12	148.29	420.32	786.27	907.27	1303.99
H H H H H	21.67	122.73	346.78	647.34	751.23	1066.91
C G C G C	47.25	267.28	753.78	1369.05	1546.22	2312.47
G C G C G	33.24	189.36	539.66	1030.77	1296.00	1697.15
C G G G C	46.30	260.74	730.42	1246.90	1445.76	2212.08
G C C C G	34.01	194.21	555.22	1068.90	1457.42	1765.06
C H C H C	49.29	278.53	784.28	1408.92	1592.48	2398.39
H C H C H	31.39	178.83	509.77	976.76	1299.75	1606.08
C H H H C	49.69	278.92	777.45	1272.52	1521.35	2334.10
H C C C H	31.31	178.92	512.26	989.70	1464.06	1649.52
G H G H G	26.13	148.04	418.41	770.04	872.60	1289.83
H G H G H	22.25	126.30	358.18	677.16	818.03	1111.65
G H H H G	26.84	151.70	427.18	764.78	865.12	1307.05
H G G G H	21.68	123.30	350.66	667.94	841.38	1096.45

Table 4.12. Natural frequency values of clamped-free curved beams (Hz), ($a/R = 1.2$)

Stacking Sequence	Mode Number					
	1	2	3	4	5	6
C C C C C	53.87	279.94	824.66	1573.37	2007.25	2640.63
G G G G G	26.55	138.03	406.88	776.75	989.55	1304.91
H H H H H	22.02	114.23	335.67	638.89	819.68	1068.27
C G C G C	48.02	248.71	729.30	1369.83	1669.74	2309.54
G C G C G	33.78	176.33	522.75	1012.85	1410.17	1709.24
C G G G C	47.06	242.51	706.20	1284.93	1519.97	2205.58
G C C C G	34.57	180.89	538.05	1049.90	1564.74	1800.09
C H C H C	50.09	259.16	758.71	1417.21	1711.66	2394.43
H C H C H	31.89	166.53	493.90	959.33	1402.13	1630.85
C H H H C	50.50	259.36	751.36	1332.41	1576.06	2325.70
H C C C H	31.82	166.67	496.54	972.26	1521.99	1734.11
G H G H G	26.55	137.78	404.91	765.91	947.05	1289.01
H G H G H	22.61	117.57	346.83	666.04	892.56	1116.07
G H H H G	27.28	141.16	413.24	770.90	928.07	1304.71
H G G G H	22.03	114.80	339.64	656.25	915.12	1104.83

Table 4.13. Natural frequency values of clamped-free curved beams (Hz), ($a / R = \pi / 2$)

Stacking Sequence	Mode Number					
	1	2	3	4	5	6
C C C C C	55.01	259.91	796.08	1550.86	2173.53	2661.00
G G G G G	27.11	128.16	392.78	765.71	1071.77	1314.58
H H H H H	22.49	106.05	324.02	629.53	886.68	1077.88
C G C G C	49.04	230.87	703.88	1356.78	1810.01	2315.03
G C G C G	34.49	163.76	504.79	995.52	1502.45	1753.16
C G G G C	48.05	225.06	681.41	1289.12	1633.50	2202.60
G C C C G	35.30	168.01	519.68	1031.23	1621.03	1896.84
C H C H C	51.15	240.57	732.23	1406.40	1853.83	2397.89
H C H C H	32.57	154.66	476.98	942.33	1464.30	1705.36
C H H H C	51.57	240.67	724.93	1351.67	1677.60	2319.49
H C C C H	32.49	154.81	479.64	954.68	1532.19	1874.61
G H G H G	27.12	127.92	390.83	757.01	1027.05	1294.02
H G H G H	23.09	109.17	334.84	655.14	959.20	1134.74
G H H H G	27.86	131.04	398.83	765.65	1004.74	1306.15
H G G G H	22.50	106.60	327.95	644.96	973.54	1134.86

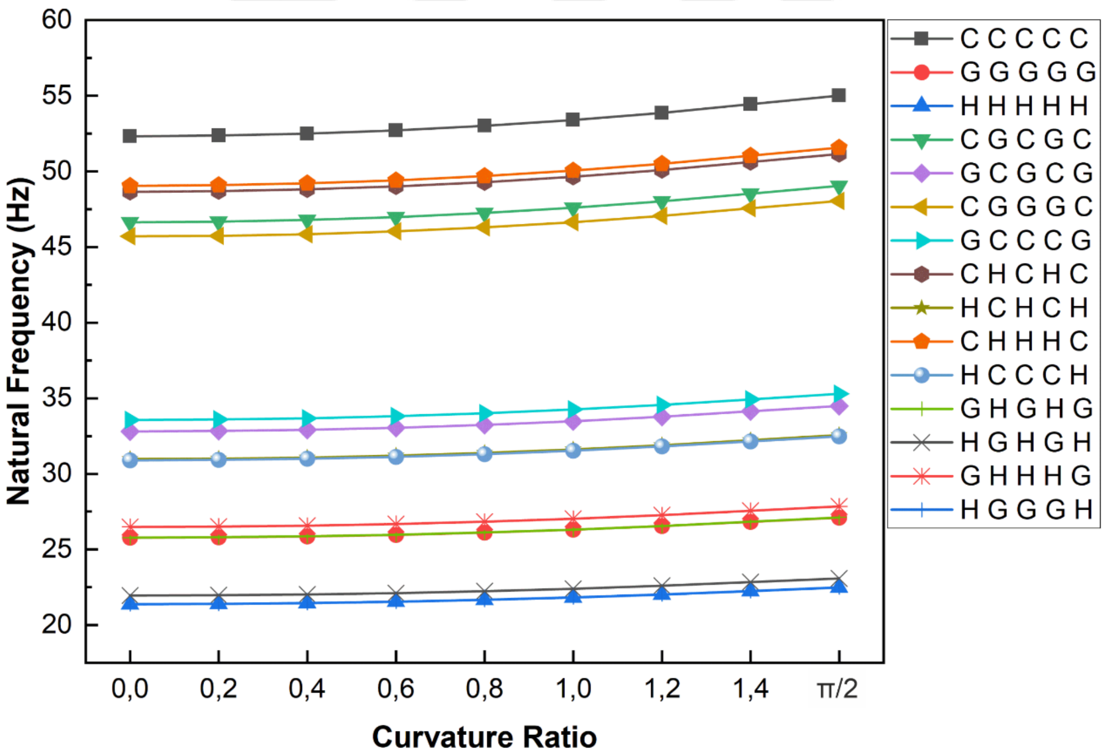

Figure 4.8. Fundamental mode frequency values of the beams with C-F boundary conditions

In Tables 4.14-4.18, natural frequency values of straight and curved beams are presented for different curvature ratios with S-S boundary conditions. As in C-F boundary conditions, the CCCCC composite beam has the highest frequency values, while the HHHHH composite beam has the lowest with S-S boundary conditions. As the curvature ratio increases from 0 to 0.4, second mode frequency values decrease slightly, and then the frequency values increase with the curvature ratio. For the third and sixth modes, there is an increment in the frequency values as the curvature ratio increases. For the fourth and fifth modes, there is a small decrement as the curvature ratio increases. And lastly, the natural frequency values for fundamental modes with respect to curvature ratio are presented in Figures 4.9 and 4.10. In Figure 4.9, it is seen that the CHCHC stacking sequence has the highest frequency values for all curvature ratios after the pure carbon composite. For curvature ratio values of 0.2, 0.4, and 0.6, the CHHHC stacking sequence has lower frequency values than the CHCHC and CGCGC stacking sequences. On the other hand, for higher curvature ratios (from 0.8 to $\pi / 2$), the CHHHC beam has almost identical frequency values with the CHCHC beam and higher frequency values than the CGCGC beam. GHGHG and GHHHG beams have nearly the same frequency values as the GGGGG beam and higher frequency values than the HHHHH beam. In hybrid composite beams where fibers with low mechanical properties are placed on the outer surface, GCCCG and GCGCG beams have higher frequency values than HCCCH and HCHCH, especially at higher curvature ratios.

Table 4.14. Natural frequency values of simply supported straight beams (Hz), ($a / R = 0$)

Stacking Sequence	Mode Number					
	1	2	3	4	5	6
C C C C C	146.41	575.42	1259.37	2160.13	3236.78	3248.30
G G G G G	72.16	283.75	621.44	1066.83	1600.03	1600.78
H H H H H	59.84	234.74	512.34	875.87	1307.71	1328.42
C G C G C	130.44	511.34	1114.73	1902.97	2653.27	2836.80
G C G C G	91.87	362.40	797.59	1377.53	2079.90	2334.98
C G G G C	127.73	498.75	1080.99	1832.69	2334.98	2712.14
G C C C G	94.04	371.69	820.46	1422.26	2156.35	2653.27
C H C H C	136.05	532.82	1159.93	1976.90	2704.49	2941.99
H C H C H	86.75	342.18	753.02	1300.38	1963.06	2358.90
C H H H C	137.01	533.41	1151.23	1942.38	2358.90	2860.41
H C C C H	86.58	342.43	756.73	1313.61	1994.71	2704.49
G H G H G	72.16	283.24	618.72	1058.84	1515.93	1582.72
H G H G H	61.45	241.62	529.15	908.32	1362.13	1463.49
G H H H G	74.09	290.20	631.88	1077.21	1463.49	1603.64
H G G G H	59.90	235.93	518.05	892.14	1342.59	1515.93

Table 4.15. Natural frequency values of simply supported curved beams (Hz), ($a / R = 0.4$)

Stacking Sequence	Mode Number					
	1	2	3	4	5	6
C C C C C	397.41	569.51	1262.21	2152.98	3233.60	3271.50
G G G G G	195.85	280.83	622.83	1063.29	1598.45	1612.24
H H H H H	162.50	232.33	513.53	872.99	1306.44	1337.83
C G C G C	328.99	506.06	1116.28	1896.15	2673.37	2833.83
G C G C G	280.59	358.70	800.76	1373.35	2078.06	2350.12
C G G G C	295.08	493.56	1081.56	1825.13	2354.30	2709.09
G C C C G	315.09	367.92	825.18	1418.15	2154.65	2668.12
C H C H C	336.62	527.31	1161.31	1969.65	2725.29	2938.86
H C H C H	281.25	338.70	756.90	1296.56	1961.45	2372.75
C H H H C	301.69	527.82	1151.38	1933.48	2379.70	2857.08
H C C C H	317.85	338.97	762.84	1309.94	1993.33	2704.45
G H G H G	186.99	280.33	619.76	1055.17	1527.16	1581.10
H G H G H	177.31	239.15	530.82	905.46	1360.87	1473.38
G H H H G	182.34	287.20	632.59	1073.23	1474.80	1601.93
H G G G H	182.27	233.52	520.11	889.43	1341.41	1525.70

Table 4.16. Natural frequency values of simply supported curved beams (Hz), ($a/R = 0.8$)

Stacking Sequence	Mode Number					
	1	2	3	4	5	6
C C C C C	552.36	733.60	1281.67	2132.70	3224.35	3338.46
G G G G G	272.38	361.57	632.38	1053.26	1593.87	1645.31
H H H H H	225.33	299.86	521.65	864.81	1302.74	1364.95
C G C G C	490.74	604.96	1127.72	1877.07	2731.19	2825.14
G C G C G	347.97	517.79	822.85	1361.33	2072.82	2393.49
C G G G C	478.50	538.09	1087.65	1804.65	2409.18	2700.13
G C C C G	356.95	577.05	860.50	1406.25	2149.88	2708.75
C H C H C	511.33	618.06	1171.91	1949.46	2785.03	2929.72
H C H C H	328.59	516.60	785.10	1285.53	1956.92	2411.34
C H H H C	511.66	546.68	1155.57	1910.04	2437.89	2847.28
H C C C H	328.89	572.27	813.72	1299.26	1989.64	2701.07
G H G H G	271.86	344.47	627.16	1044.84	1559.53	1576.37
H G H G H	231.97	327.46	542.18	897.29	1357.23	1501.84
G H H H G	278.50	334.67	638.14	1062.17	1507.28	1596.93
H G G G H	226.52	336.22	534.47	881.62	1338.02	1553.60

Table 4.17. Natural frequency values of simply supported curved beams (Hz), ($a/R = 1.2$)

Stacking Sequence	Mode Number					
	1	2	3	4	5	6
C C C C C	525.53	988.61	1383.75	2101.91	3210.01	3442.03
G G G G G	259.14	487.48	682.43	1038.04	1586.76	1696.49
H H H H H	214.38	403.33	564.23	852.37	1297.02	1406.80
C G C G C	466.80	833.84	1188.34	1848.34	2811.47	2820.54
G C G C G	331.15	663.17	936.61	1342.73	2065.06	2458.77
C G G G C	455.01	755.14	1122.62	1775.40	2492.76	2685.86
G C C C G	339.76	703.08	1030.53	1387.66	2143.33	2761.56
C H C H C	486.36	855.86	1228.55	1919.64	2877.20	2915.30
H C H C H	312.73	639.80	924.64	1268.34	1950.55	2664.45
C H H H C	486.46	772.15	1182.95	1877.74	2525.15	2831.63
H C C C H	313.07	661.71	1027.11	1282.46	1985.42	2692.21
G H G H G	258.62	471.42	666.09	1029.34	1568.97	1609.64
H G H G H	220.72	429.95	601.43	884.74	1351.73	1545.33
G H H H G	264.90	464.13	667.89	1045.88	1557.34	1589.03
H G G G H	215.56	430.59	608.30	869.53	1333.03	1595.28

Table 4.18. Natural frequency values of simply supported curved beams (Hz), ($a / R = \pi / 2$)

Stacking Sequence	Mode Number 1	2	3	4	5	6
C C C C C	493.87	1066.50	1629.69	2066.32	3194.07	3561.59
G G G G G	243.53	526.14	803.37	1020.45	1578.83	1755.67
H H H H H	201.47	434.31	665.65	837.97	1290.73	1454.82
C G C G C	438.58	926.33	1358.74	1816.48	2795.67	2924.60
G C G C G	311.28	689.23	1144.74	1320.83	2057.51	2528.59
C G G G C	427.38	870.05	1236.82	1743.24	2589.62	2668.94
G C C C G	319.43	716.49	1283.44	1365.56	2138.68	2800.93
C H C H C	456.94	958.33	1393.54	1885.97	2898.51	2984.55
H C H C H	294.00	655.53	1145.54	1247.96	1945.45	2509.76
C H H H C	456.84	906.13	1278.97	1843.07	2625.41	2812.89
H C C C H	294.36	665.67	1262.35	1293.24	1985.75	2679.54
G H G H G	243.02	518.08	770.00	1011.62	1560.50	1667.96
H G H G H	207.45	453.59	724.17	870.06	1346.00	1593.80
G H H H G	248.88	521.09	755.60	1027.51	1579.81	1615.69
H G G G H	202.62	447.52	743.30	855.31	1328.24	1639.03

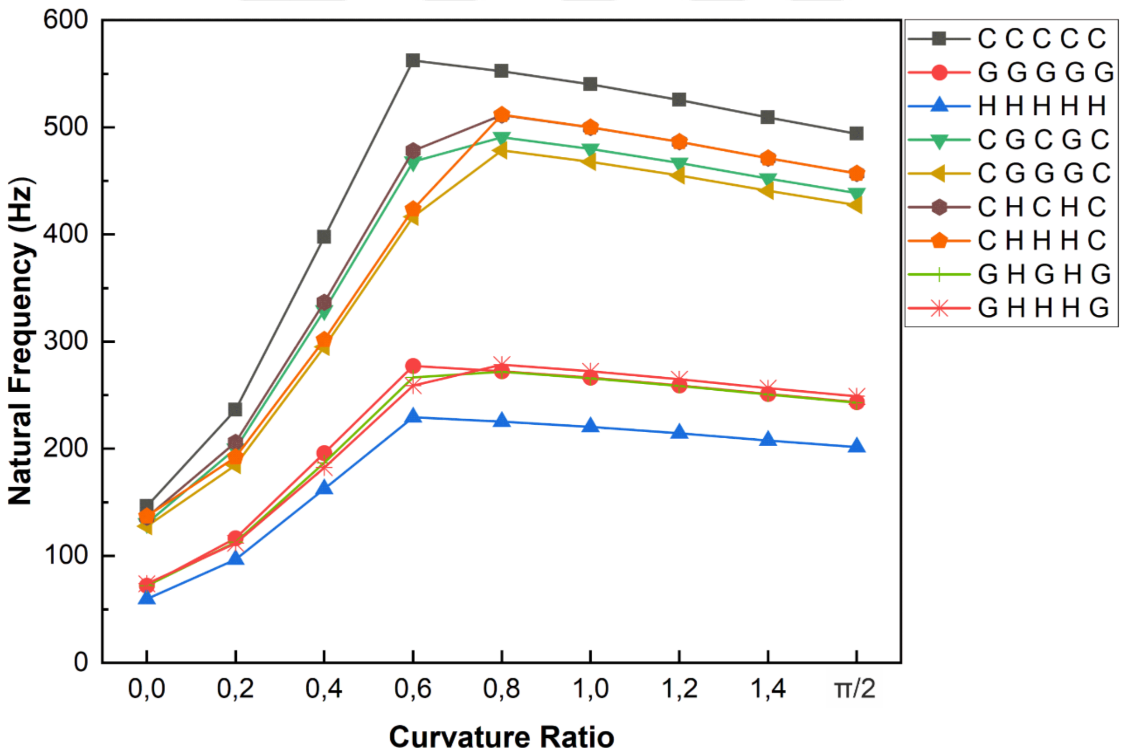

Figure 4.9. Fundamental mode frequency values of the beams with S-S boundary conditions

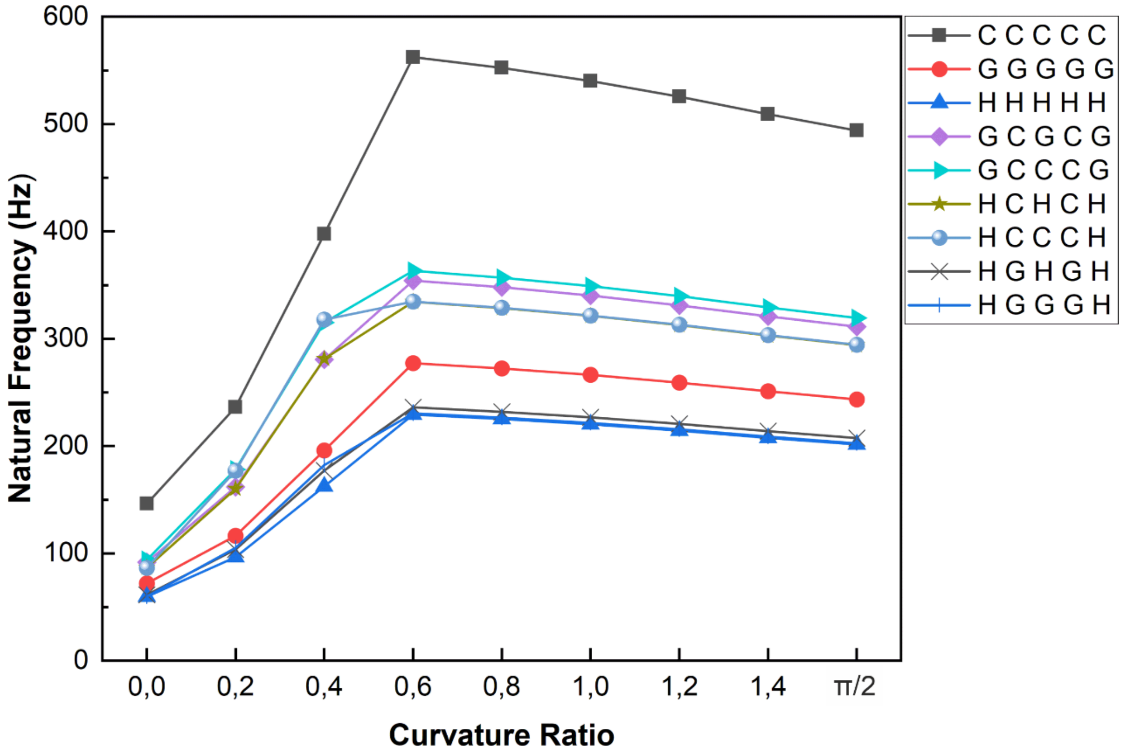

Figure 4.10. Fundamental mode frequency values of the beams with S-S boundary conditions

In Tables 4.19-4.23, natural frequency values of straight and curved beams are presented for different curvature ratios with C-C boundary conditions. As in C-F and S-S boundary conditions, the CCCCC composite beam has the highest frequency values, while the HHHHH composite beam has the lowest with C-C boundary conditions. As the curvature ratio increases from 0 to 0.8, second mode frequency values decrease slightly, and then frequency values increase with the curvature ratio. For the third and fifth modes, the frequency values are increasing while the curvature ratio increases. For the fourth and sixth modes, as the curvature ratio increases, there are slight decreases in frequency values. In Figures 4.11 and 4.12, the fundamental mode frequency change of the beams with the curvature ratio is presented. In general, hybrid composite beams, where a higher mechanical property fabric is located on outer surfaces, have higher frequency values for C-C boundary conditions. After the CCCCC stacking sequence, the highest frequency values are observed for the CHCHC stacking sequence. CGCGC stacking sequence has higher frequency values than CHHHC for curvature ratio values of 0.4, 0.6, 0.8, and 1.0. On the other hand, for higher curvature ratios (from 1 to

$\pi/2$), the CHHHC beam has almost identical frequency values with the CHCHC beam and higher frequency values than the CGCGC beam. As in S-S boundary conditions, GHGHG and GHHHG beams have nearly the same frequency values as the GGGGG beam and higher frequency values than the HHHHH beam. Comparing hybrid composite beams where fabrics with low mechanical properties are placed on the outer surface, GCCCG and GCGCG have higher frequency values than HCCCH and HCHCH, especially for higher curvature ratios.

Table 4.19. Natural frequency values of clamped-clamped straight beams (Hz), ($a/R=0$)

Stacking Sequence	Mode Number					
	1	2	3	4	5	6
C C C C C	325.36	869.41	1640.41	2594.78	3248.30	3695.10
G G G G G	160.46	429.14	810.47	1283.26	1600.78	1829.19
H H H H H	132.64	353.27	664.11	1046.49	1328.42	1484.74
C G C G C	288.83	768.12	1441.66	2267.99	2653.27	3212.66
G C G C G	205.19	552.07	1049.75	1674.21	2334.98	2403.80
C G G G C	281.31	742.91	1383.89	2160.66	2334.98	3038.80
G C C C G	210.62	568.75	1086.05	1740.06	2510.08	2653.27
C H C H C	300.92	799.02	1497.07	2351.00	2704.49	3324.70
H C H C H	193.70	521.03	990.49	1579.30	2266.94	2358.90
C H H H C	300.67	790.21	1464.51	2275.14	2358.90	3185.24
H C C C H	194.01	524.48	1002.90	1609.33	2325.24	2704.49
G H G H G	160.11	426.91	803.51	1267.73	1515.93	1800.83
H G H G H	136.61	365.29	689.76	1091.94	1463.49	1556.20
G H H H G	163.95	435.51	816.30	1282.43	1463.49	1814.28
H G G G H	133.45	357.93	678.26	1077.74	1515.93	1541.64

Table 4.20. Natural frequency values of clamped-clamped curved beams (Hz), ($a / R = 0.4$)

Stacking Sequence	Mode Number 1	2	3	4	5	6
C C C C C	471.49	863.16	1644.51	2582.37	3273.88	3692.35
G G G G G	232.43	426.06	812.47	1277.07	1613.46	1827.82
H H H H H	192.58	350.73	665.85	1041.62	1338.65	1483.66
C G C G C	401.55	762.53	1444.33	2254.44	2677.88	3210.00
G C G C G	319.51	548.17	1053.67	1667.79	2350.29	2402.32
C G G G C	373.50	737.40	1385.54	2140.35	2365.32	3035.96
G C C C G	348.69	564.78	1091.46	1734.12	2508.81	2668.40
C H C H C	414.03	793.18	1499.62	2335.91	2730.92	3321.88
H C H C H	314.13	517.37	995.10	1573.73	2265.73	2372.80
C H H H C	389.93	784.27	1465.80	2242.62	2401.69	3182.10
H C C C H	343.01	520.84	1009.57	1604.27	2324.36	2716.51
G H G H G	225.86	423.82	805.16	1260.78	1529.14	1799.39
H G H G H	205.64	362.68	691.98	1087.41	1473.74	1555.16
G H H H G	224.84	432.33	817.64	1273.91	1478.15	1812.73
H G G G H	207.65	355.40	680.85	1073.62	1525.78	1540.70

Table 4.21. Natural frequency values of clamped-clamped curved beams (Hz), ($a / R = 0.8$)

Stacking Sequence	Mode Number 1	2	3	4	5	6
C C C C C	742.95	845.02	1662.07	2549.52	3344.97	3684.47
G G G G G	366.20	417.11	821.05	1260.74	1648.67	1823.89
H H H H H	303.61	343.35	673.30	1028.64	1367.17	1480.57
C G C G C	619.07	746.29	1455.86	2220.83	2743.69	3202.32
G C G C G	518.88	536.84	1070.75	1650.00	2393.70	2398.18
C G G G C	559.47	721.41	1392.97	2099.35	2435.53	3027.73
G C C C G	553.22	577.13	1115.76	1717.36	2505.39	2711.16
C H C H C	634.46	776.25	1510.68	2299.43	2800.42	3313.74
H C H C H	506.72	516.64	1015.59	1558.09	2262.45	2412.12
C H H H C	574.29	767.09	1471.90	2193.71	2480.52	3172.94
H C C C H	510.24	575.55	1040.93	1589.82	2322.20	2748.98
G H G H G	351.06	414.85	812.27	1243.07	1565.04	1795.25
H G H G H	329.46	355.11	701.57	1075.04	1502.66	1552.23
G H H H G	343.88	423.10	823.46	1253.59	1516.34	1808.25
H G G G H	336.98	348.03	692.16	1062.18	1538.08	1553.68

Table 4.22. Natural frequency values of clamped-clamped curved beams (Hz), ($a / R = 1.2$)

Stacking Sequence	Mode Number 1	2	3	4	5	6
C C C C C	816.58	1007.05	1714.41	2505.47	3449.64	3672.64
G G G G G	403.07	496.52	846.60	1238.39	1700.46	1817.99
H H H H H	331.77	411.01	695.50	1010.67	1409.28	1475.97
C G C G C	720.89	839.01	1490.10	2177.98	2837.02	3190.54
G C G C G	519.03	698.84	1123.22	1624.07	2392.33	2458.81
C G G G C	696.48	755.29	1415.58	2054.72	2526.05	3014.92
G C C C G	535.03	767.53	1193.04	1692.27	2501.10	2774.21
C H C H C	749.76	859.40	1543.58	2254.07	2897.56	3301.20
H C H C H	489.97	689.32	1080.05	1534.76	2258.21	2470.20
C H H H C	740.33	772.43	1491.16	2146.46	2574.76	3158.64
H C C C H	493.54	748.66	1143.67	1567.79	2320.44	2791.35
G H G H G	400.81	476.09	833.34	1219.83	1616.77	1788.94
H G H G H	343.22	444.92	730.57	1057.33	1545.81	1548.00
G H H H G	408.67	465.82	840.79	1228.65	1569.33	1801.34
H G G G H	336.44	453.18	726.94	1045.46	1534.42	1595.36

Table 4.23. Natural frequency values of clamped-clamped curved beams (Hz), ($a / R = \pi / 2$)

Stacking Sequence	Mode Number 1	2	3	4	5	6
C C C C C	782.94	1183.25	1832.37	2457.13	3566.19	3660.16
G G G G G	386.48	583.80	904.26	1214.96	1758.14	1811.73
H H H H H	318.09	481.61	745.30	991.65	1456.09	1471.22
C G C G C	690.94	998.22	1568.50	2135.08	2939.15	3177.48
G C G C G	497.91	799.83	1236.46	1595.41	2387.16	2531.16
C G G G C	667.16	908.04	1468.47	2013.33	2621.60	3000.25
G C C C G	513.41	856.51	1349.01	1663.83	2498.85	2840.97
C H C H C	718.54	1025.18	1619.19	2209.33	3003.18	3287.19
H C H C H	470.08	774.21	1212.48	1508.55	2255.60	2532.15
C H H H C	708.95	932.09	1537.01	2104.21	2672.55	3142.09
H C C C H	473.66	812.77	1329.54	1542.38	2322.67	2826.59
G H G H G	384.23	564.39	881.37	1196.16	1673.82	1782.04
H G H G H	329.15	514.73	794.34	1038.09	1543.96	1593.81
G H H H G	391.66	556.37	880.69	1204.24	1626.78	1793.59
H G G G H	322.70	517.63	801.56	1026.96	1531.32	1641.29

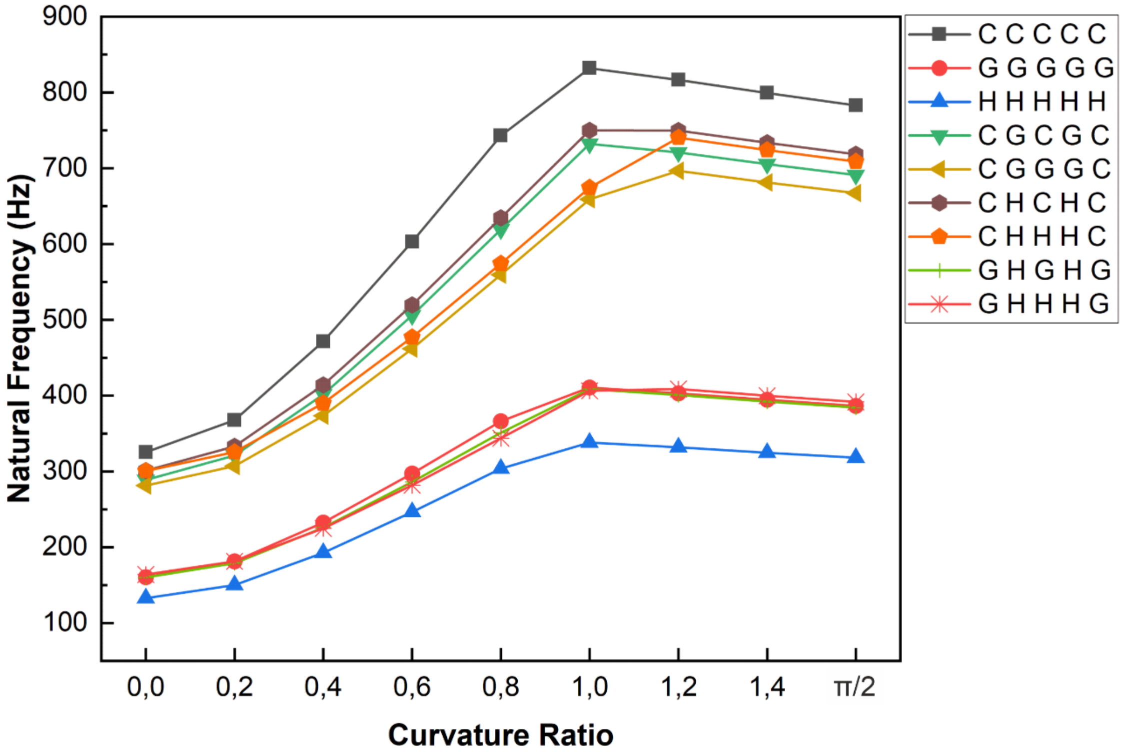

Figure 4.11. Fundamental mode frequency values of the beams with C-C boundary conditions

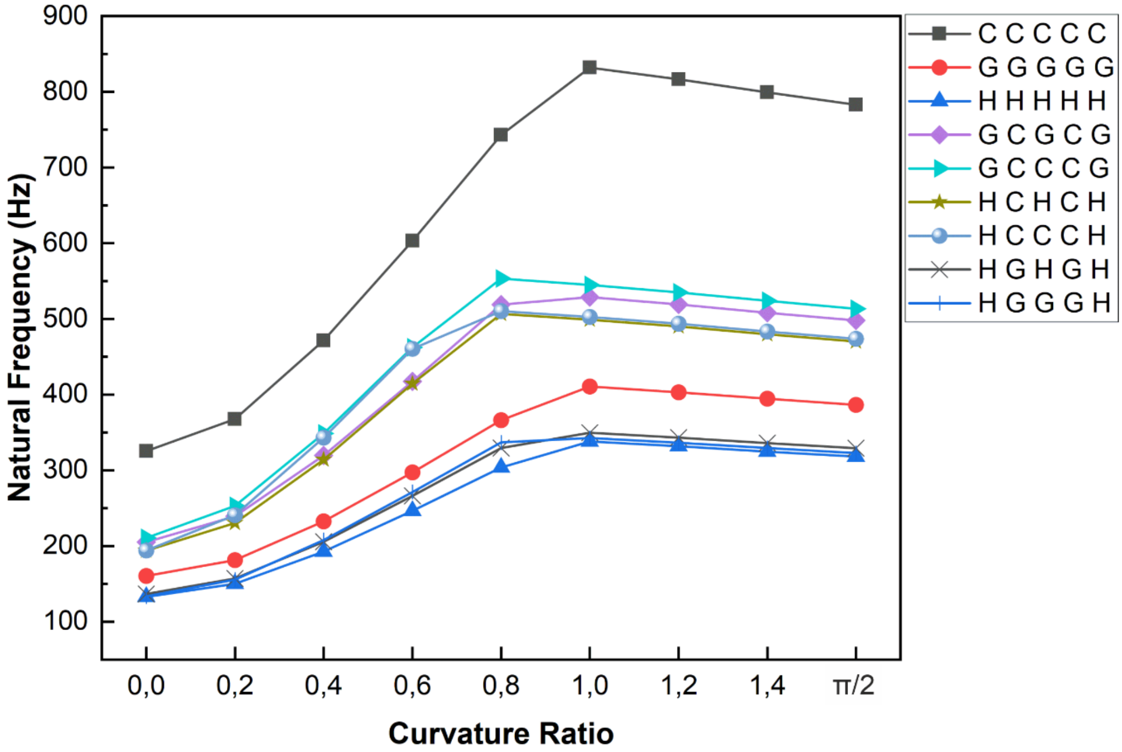

Figure 4.12. Fundamental mode frequency values of the beams with C-C boundary conditions

When all tables and figures are examined, boundary condition C-F has the lowest effect on frequency values. Fundamental mode frequency values increase as the curvature ratio increases, but no significant change is observed for C-F boundary conditions. For S-S and C-C boundary conditions, in general, there are slight changes in frequency values in the second, third, fourth, fifth, and sixth modes. However, S-S and C-C boundary conditions have a significant effect on the frequency values of fundamental modes. In general, fundamental frequency values increase with the curvature ratio up to a certain value, and then slight decreases are observed for further increases in curvature ratios. For S-S boundary conditions, the decrement of fundamental frequency values generally begins between curvature ratio values of 0.6-0.8. For C-C, the value where the decrement of the fundamental frequency values begins is between 0.8 and 1. Regardless of the boundary conditions, the pure carbon composite beam (CCCCC) has the highest frequency values, whereas the pure hemp composite beam has the lowest for all curvature ratios. On the other hand, hybridization of the hemp fiber with carbon fiber has an increasing effect on the frequency parameter. Even higher frequency values are achieved for carbon/hemp hybrid composites than for carbon/glass hybrid composites for certain stacking sequences. For C-F boundary conditions, CHHHC and CHCHC beams have the highest natural frequency values after the CCCCC beam. For S-S and C-C boundary conditions, the highest frequency values are observed for the CHCHC beam after the CCCCC beam. For S-S and C-C boundary conditions, CHHHC and CGCGC beams have the highest frequency values after the CCCCC and CHCHC beams. Generally, irrespective of the stacking sequence, combining lower mechanical property fibers with those of higher strength leads to an increase in natural frequency values. This effect is further amplified when the higher-strength fibers are placed on the outer layers.

4.4. Free Vibration Results of Laminated Composite Plates

4.4.1. Validation Studies of Plates

In the present study, a computer program was developed to perform linear and nonlinear modal analysis for laminated plates using the GDQ method. To validate the accuracy and applicability of the computer program, several validation studies from the literature were considered. In the first validation study, the linear free vibration behavior of a laminated composite plate made of glass fiber/epoxy and aluminum layers (GLARE) was analyzed. The results are presented in

Table 4.25 and compared with the studies of Maraş and Yaman, as well as Harras et al., which employed FEM, DQM, GDQ, HDQ, Rayleigh-Ritz, ESDU, and experimental methods [130], [161]. The plate has dimensions of 300 mm in length (a) and 450 mm in width (b), with a total thickness of 1.4 mm. It consists of five layers with a stacking sequence of [Al, 0/90, Al, 0/90, Al], where aluminum sheets are 0.3 mm thick and glass fiber/epoxy layers are 0.25 mm thick. The material properties used in this study are provided in Table 4.24. The plate is subjected to clamped boundary conditions along all its edges.

Table 4.24. Mechanical and physical properties of materials used in GLARE plates [130]

Material	E_x (Gpa)	E_y (Gpa)	E_z (Gpa)	G_{xy} (Gpa)	G_{yz} (Gpa)	G_{xz} (Gpa)	v_{xy}	v_{xy}	v_{xy}	ρ (kg/m^3)
Glass/Epoxy	31.17	31.17	9.41	5.54	5.54	5.54	0.098	0.057	0.057	2,000
Al 2024-T3	72.30			27.60			0.33			2,700

Table 4.25 shows that the present results based on the GDQ method indicate strong agreement with the findings of Harras et al. and Maraş and Yaman. One of the key advantages of the GDQ method is that it requires less computational time, as it utilizes fewer nodes or grid points compared to other numerical approaches. However, before applying the GDQ method, a convergence study for the mesh is often necessary to determine the appropriate number of grids to yield accurate results. In this study, the number of grids in the *x* and *y* directions ($n_x = n_y = 15$) was found to be sufficient for the convergence of the results.

Table 4.25. Comparison of the natural frequency results for GLARE plates obtained using the GDQ method with previous results

$a=300$ mm, $b=450$ mm, $t_{Al}=0.3$ mm, $t_{E-Glass}(0^{\circ}\,90^{\circ})=0.25$ mm, $h=1.4$ mm							
Methods	n_x x n_y	Mode Number (Hz)					
		1	2	3	4	5	6
FEM [130]		104.51	161.03	256.16	257.04	307.96	-
DQM [130]		104.62	161.50	256.63	257.65	309.11	-
GDQ [130]		104.72	161.54	256.55	257.67	309.07	-
HDQ [130]		104.73	161.53	256.66	257.81	309.10	-
ESDU [161]		105.60	162.90	259.40	260.30	311.90	-
FEM [161]		105.37	162.31	258.34	259.13	310.45	-
Rayleigh-Ritz [161]		104.64	161.26	256.63	257.52	308.63	-
Experimental [161]		93.50	153.00	245.00	253.00	298.00	-
Present Study	9x9	104.56	161.23	256.33	257.37	308.50	398.05
	11x11	104.56	161.20	256.26	257.28	308.37	392.06
	13x13	104.56	161.20	256.26	257.28	308.36	390.24
	15x15	**104.56**	**161.20**	**256.26**	**257.28**	**308.36**	**290.20**
	17x17	104.56	161.20	256.26	257.28	308.36	390.20

To verify the nonlinear free vibration analysis method, a second validation study was carried out for a 400 mm steel square plate with a thickness of 2.5 mm, having $E=210$ Gpa, $\rho=7850$ kg/m^3, and $v=0.3$ for all edges clamped. The geometrically nonlinear free vibration analysis results were compared with those of numerous researchers and are presented in Table 4.26. As can be seen from the table, there are slight variations between different methods. However, the present results are compatible with the previous findings. Slight variations between different methods can be attributed to the different methodologies employed in the solutions. The dimensionless amplitude ($w^*=w_{\max}/h$) was defined as the ratio of the maximum deflection of the plate to its thickness. Meanwhile, the nonlinear frequency was expressed in a normalized form (ω_{NL}/ω_L) by dividing it by the corresponding fundamental linear frequency (ω_L).

Table 4.26. Comparison of nonlinear frequency ratios of a isotropic square plate with all edges clamped

	w_{max}/h					
	0.2	0.4	0.6	0.8	1.0	1.5
Ref. [162]	1.0129	1.0306	1.0665	1.1157	1.1684	1.3613
Ref. [163]	1.0073	1.0291	1.0648	1.1138	1.1762	---
Ref. [164]	1.0070	1.0276	1.0607	1.1044	1.1573	1.3499
Ref. [165](a)	1.0068	1.0271	1.0600	1.1047	1.1599	1.3355
Ref. [165](b)	1.0105	1.0411	1.0894	1.1521	1.2260	1.4431
Ref. [166](c)	1.0112	1.0368	1.0815	1.1356	1.2005	1.3896
Ref. [166](d)	1.0113	1.0387	1.0873	1.1508	1.2264	1.4615
Present Study	1.0072	1.0285	1.0629	1.1098	1.1670	1.3459

(a) Following the HFEM method.
(b) Following the HFEM method, without considering in-plane displacements.
(c) For deflection profile corresponding to concentrated load.
(d) For deflection profile corresponding to uniformly distributed loading.

In the third validation study, four-layer laminated composite plates with varying fiber orientations, all under simply supported boundary conditions, were presented. The results of these configurations are provided in Table 4.27, and the results were compared with those of Singh et al. and Pirbodaghi et al. [167], [168]. The thickness of each ply was assumed to be equal, and the material properties are as follows: $E_1 = 206.84$ Gpa, $E_2 = E_3 = 5.171$ Gpa, $G_{12} = 2.855$ Gpa, $v_{12} = 0.25$, $a = b = 0.254$ m, and $\rho = 2564.8$ kg/m^3. The nonlinear-to-linear frequency ratios were obtained according to only fundamental frequencies for different w_{max}/h values. Although there are slight differences in the results, the current study agrees better with that of Pirbodaghi et al. [168]. The nonlinear natural frequency varies based on the vibration amplitude. As the amplitude of vibration increases, the gap between the nonlinear frequency and the linear frequency increases. Generally, higher vibration amplitudes lead to a greater frequency ratio, meaning the nonlinear frequency becomes significantly higher compared to the linear frequency.

Table 4.27. Comparison of nonlinear-to-linear frequency ratio (ω_{NL} / ω_L) for square thin cross-ply laminated plates (*a*/*h*=40)

w_{max} / h	$[0°,90°,90°,0°]$			$[0°,90°,0°,90°]$		
	Ref. [167]	Ref. [168]	Present Study	Ref. [167]	Ref. [168]	Present Study
0.25	1.0535	1.0501	1.0421	1.0634	1.0514	1.0410
0.5	1.2038	1.1879	1.1622	1.2388	1.1924	1.1621
0.75	1.4172	1.3874	1.3497	1.4832	1.3961	1.3433
1.0	1.6691	1.6245	1.5872	1.7679	1.6392	1.5717
1.5	2.2355	2.1659	2.1419	2.4000	2.1899	2.1220

4.4.2. Parametric Study Results of Laminated Composite Plates

In this section, linear and nonlinear free vibration analysis results of carbon, glass, and hemp fiber-reinforced composite plates were presented. The effects of hybridization of different fibers, stacking sequence, aspect ratio, and boundary conditions were studied. The stacking sequences of the composite plates are presented in Figure 4.13. Carbon, glass, and hemp layers are denoted as C, G, and H, respectively, and all plates were designated according to the respective layer stacking order. As can be seen from the stacking sequence arrangement, carbon, glass, and hemp fiber-reinforced composite plates were analyzed in the first stage. Afterward, carbon, glass, and hemp fibers were combined in a binary manner to form a hybrid composite material, and further analyses were performed. Both linear and nonlinear free vibration analyses were carried out for simply supported and fully clamped boundary conditions. All laminae were postulated to have the same thickness of 2 mm, and the total thickness of the plates was taken as 10 mm. Dimensions of the square plates were taken as $a = b = 1000$ mm, and for the different aspect ratios of rectangular plates, b length was decreased while a length was kept constant. The fiber orientation of the plates was chosen to be cross-ply as $[0°,90°,0°,90°,0°]$ for all analyses.

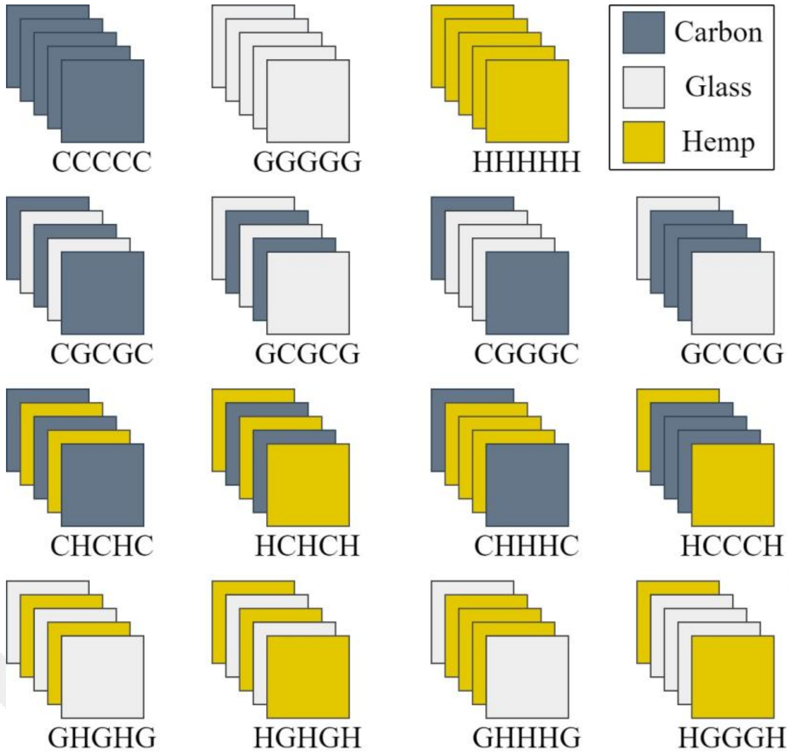

Figure 4.13. Stacking sequences of laminated composite plates.

4.4.2.1. Linear Free Vibration Analysis Results

In this section, linear free vibration analysis results of the composite plates are presented for six modes. In Tables 4.28-4.31, natural frequencies of the composite plates under simply supported boundary conditions are presented for different aspect ratios. The reduction of b length leads to a decrease in the mass of the composite plates, which results in an increase in the natural frequency values as the aspect ratio increases. As can be seen in Tables 4.28 and 4.32, the natural frequencies of the second and third modes and the fifth and sixth modes are identical for square plates. This situation results from the bidirectional fiber utilization ($E_1 = E_2$) and the cross-ply fiber configuration of the composite plates. As the aspect ratio increases, natural frequencies exhibit different values for each of the six modes. In Tables 4.28-4.31, as expected, the highest natural frequency values are obtained for the composite plate with pure carbon fiber (CCCCC). Composite plates with pure glass and pure hemp fibers exhibit lower natural frequency values than the carbon fiber-reinforced composite plate. However, the hemp fiber-reinforced composite plate exhibits relatively close natural frequency values to those of the glass fiber-reinforced composite plate. Therefore, in terms of vibration performance, hemp fiber-reinforced composites can be a suitable alternative to glass fiber-reinforced composites, which are widely used in various applications. When different stacking sequences are compared, it is seen that the highest natural frequency values are obtained in the scenarios where the carbon fiber layer is on the bottom and top surfaces of the plates. This result supports the fact that, given the superior mechanical properties of carbon compared to other materials, using a stronger material in the bottom and top layers (farthest from the neutral axis) increases the natural frequency of composite plates. In this context, the present results are compatible with earlier studies [73], [160]. Considering the hybridization effect of different fibers, carbon/hemp fiber-reinforced composite plates exhibit slightly higher natural frequency values than those of carbon/glass fiber-reinforced composite plates for certain stacking sequences. Among carbon/hemp hybrid composite plates, CHCHC and CHHHC stacking sequences exhibit higher frequency values than CGCGC and CGGGC stacking sequences of carbon/glass hybrid composites. On the contrary, HCHCH and HCCCH stacking sequences exhibit lower frequency values than GCGCG and GCCCG stacking sequences. Besides, among glass/hemp hybrid composite plates, GHGHG and GHHHG sequences have higher frequency values than HGHGH and HGGGH, and their frequency values are even higher than those of the GGGGG sequence. Configurations with the highest natural frequencies are suitable for applications requiring high structural stiffness, while those with the lowest natural frequencies are better suited for applications requiring flexibility. Thus, the material combination can provide an optimal balance of lightness and durability. Hybridizing hemp fiber with carbon and glass fibers and positioning the stacking sequence so that the hemp fiber is closer to the neutral axis while carbon or glass fibers are in the outer layers has a favorable effect on natural frequencies. The aforementioned interpretations about linear free vibration results are not only valid for simply supported plates but also for fully clamped plates with different aspect ratios, as shown in Tables 4.32-4.35. The only difference is that, for the fully clamped boundary conditions, frequency values are relatively higher than those of simply supported plates. Lastly, mode shapes (first six modes) of square and rectangular plates with different aspect ratios are presented in Figures 4.14 and 4.15 for simply supported and fully clamped boundary conditions, respectively. For a given aspect ratio and boundary condition, the stacking sequence does not affect mode shapes. However, aspect ratio and boundary condition have a significant influence on mode shapes, as can be seen in Figures 4.14 and 4.15.

Table 4.28. Natural Frequencies of simply supported square plates (Hz), ($a/b=1$)

Stacking Sequence	Mode Number 1	2	3	4	5	6
C C C C C	60.20	150.64	150.64	240.37	301.26	301.26
G G G G G	29.40	73.58	73.58	117.40	147.17	147.17
H H H H H	26.04	65.13	65.13	103.95	130.17	130.17
C G C G C	53.58	134.12	134.12	213.89	268.25	268.25
G C G C G	37.71	94.24	94.24	150.62	188.32	188.32
C G G G C	52.48	131.38	131.38	209.40	262.76	262.76
G C C C G	38.61	96.48	96.48	154.27	192.80	192.80
C H C H C	56.12	140.41	140.41	224.00	280.71	280.71
H C H C H	35.93	90.33	90.33	143.53	181.30	181.30
C H H H C	56.55	141.52	141.52	225.57	282.88	282.88
H C C C H	35.83	90.06	90.06	143.15	180.78	180.78
G H G H G	29.74	74.35	74.35	118.74	148.55	148.55
H G H G H	25.94	65.11	65.11	103.59	130.48	130.48
G H H H G	30.56	76.39	76.39	121.97	152.62	152.62
H G G G H	25.26	63.39	63.39	100.87	127.06	127.06

Table 4.29. Natural Frequencies of simply supported rectangular plates (Hz), ($a/b=2$)

Stacking Sequence	Mode Number 1	2	3	4	5	6
C C C C C	150.26	239.41	388.98	511.00	598.35	598.38
G G G G G	73.38	116.90	189.97	249.65	292.27	292.29
H H H H H	65.00	103.62	168.26	220.71	258.60	258.61
C G C G C	133.75	212.96	346.01	454.91	532.26	532.30
G C G C G	94.02	150.07	243.76	319.44	374.79	374.81
C G G G C	130.99	208.40	338.56	445.40	520.70	520.74
G C C C G	96.28	153.76	249.75	327.09	383.99	384.01
C H C H C	140.02	223.01	362.25	475.91	557.04	557.07
H C H C H	90.16	143.12	232.99	308.23	359.38	359.39
C H H H C	141.07	224.45	364.50	479.25	560.32	560.37
H C C C H	89.92	142.79	232.49	307.46	358.65	358.66
G H G H G	74.14	118.23	192.00	251.82	295.14	295.16
H G H G H	64.98	103.26	167.95	221.60	258.73	258.74
G H H H G	76.17	121.41	197.15	258.65	303.03	303.05
H G G G H	63.27	100.57	163.60	215.85	252.06	252.07

Table 4.30. Natural Frequencies of simply supported rectangular plates (Hz), ($a/b=3$)

Stacking Sequence	Mode Number					
	1	2	3	4	5	6
C C C C C	300.44	387.78	535.11	742.42	1008.90	1106.46
G G G G G	146.75	189.35	261.27	362.55	492.77	540.71
H H H H H	129.89	167.85	231.64	321.18	436.04	477.21
C G C G C	267.47	344.87	475.66	659.82	896.53	984.26
G C G C G	187.85	243.05	335.73	465.85	633.00	692.25
C G G G C	261.92	337.34	464.98	644.80	875.82	962.47
G C C C G	192.35	249.08	344.19	477.63	649.09	709.23
C H C H C	279.88	361.04	497.99	690.65	938.13	1029.19
H C H C H	180.95	232.46	320.40	445.07	606.01	669.02
C H H H C	281.94	363.13	500.43	693.68	941.71	1034.44
H C C C H	180.47	232.00	319.90	444.49	605.38	667.96
G H G H G	148.11	191.36	264.12	366.32	497.55	544.86
H G H G H	130.21	167.54	230.98	320.61	436.06	480.14
G H H H G	152.15	196.47	271.08	375.90	510.45	559.24
H G G G H	126.81	163.21	225.06	312.45	425.06	467.98

Table 4.31. Natural Frequencies of simply supported rectangular plates (Hz), ($a/b=4$)

Stacking Sequence	Mode Number					
	1	2	3	4	5	6
C C C C C	510.21	595.67	740.09	944.16	1207.51	1529.45
G G G G G	249.24	290.89	361.35	460.98	589.65	747.02
H H H H H	220.44	257.69	320.38	408.67	522.28	660.86
C G C G C	454.15	529.70	657.58	838.50	1072.07	1357.53
G C G C G	318.97	373.23	464.49	593.06	758.72	961.21
C G G G C	444.58	517.96	642.38	818.60	1046.13	1324.03
G C C C G	326.65	382.52	476.37	608.44	778.56	986.53
C H C H C	475.10	554.32	688.27	877.60	1121.83	1420.13
H C H C H	307.88	358.20	444.05	566.33	725.00	919.72
C H H H C	478.34	557.23	690.95	880.19	1124.31	1422.16
H C C C H	307.15	357.60	443.57	565.96	724.79	919.80
G H G H G	251.40	293.72	365.08	465.74	595.47	753.90
H G H G H	221.33	257.82	319.82	407.82	521.69	661.11
G H H H G	258.19	301.49	374.55	477.66	610.55	772.77
H G G G H	215.60	251.21	311.72	397.59	508.74	644.88

Table 4.32. Natural Frequencies of fully clamped square plates (Hz), ($a/b=1$)

Stacking Sequence	Mode Number 1	2	3	4	5	6
C C C C C	110.14	224.29	224.29	330.21	401.21	401.21
G G G G G	53.81	109.58	109.58	161.34	196.04	196.04
H H H H H	47.58	96.85	96.85	142.55	173.17	173.17
C G C G C	98.11	199.73	199.73	293.95	357.18	357.18
G C G C G	68.84	140.21	140.21	206.68	250.83	250.83
C G G G C	96.15	195.66	195.66	287.85	349.71	349.71
G C C C G	70.45	143.52	143.52	211.61	256.83	256.83
C H C H C	102.69	209.02	209.02	307.70	373.68	373.68
H C H C H	66.15	134.85	134.85	197.80	241.80	241.80
C H H H C	103.56	210.67	210.67	309.95	376.30	376.30
H C C C H	65.94	134.45	134.45	197.25	241.19	241.19
G H G H G	54.34	110.62	110.62	163.01	197.76	197.76
H G H G H	47.65	97.07	97.07	142.53	173.85	173.85
G H H H G	55.85	113.67	113.67	167.46	203.14	203.14
H G G G H	46.39	94.52	94.52	138.80	169.34	169.34

Table 4.33. Natural Frequencies of fully clamped rectangular plates (Hz), ($a/b=2$)

Stacking Sequence	Mode Number 1	2	3	4	5	6
C C C C C	299.78	387.73	544.49	768.42	775.32	860.28
G G G G G	146.48	189.46	266.08	375.55	378.95	420.50
H H H H H	129.38	167.30	234.85	331.26	334.11	370.63
C G C G C	266.87	345.06	484.43	683.43	689.49	764.82
G C G C G	187.42	242.69	340.99	481.36	485.33	539.09
C G G G C	261.28	337.73	473.94	668.27	673.92	747.35
G C C C G	191.90	248.53	349.27	493.18	497.33	552.51
C H C H C	279.19	361.09	506.91	714.97	720.92	799.90
H C H C H	180.72	232.85	326.90	462.10	468.71	518.32
C H H H C	281.13	363.46	509.92	718.61	724.14	803.16
H C C C H	180.27	232.29	326.21	461.30	468.09	517.68
G H G H G	147.76	191.28	268.61	378.92	381.81	423.99
H G H G H	129.91	167.58	235.22	332.20	336.25	372.19
G H H H G	151.77	196.45	275.82	388.95	391.83	435.07
H G G G H	126.54	163.23	229.17	323.74	327.78	362.83

Table 4.34. Natural Frequencies of fully clamped rectangular plates (Hz), ($a/b=3$)

Stacking Sequence	Mode Number 1	2	3	4	5	6
C C C C C	632.46	704.29	836.02	1034.00	1298.77	1629.34
G G G G G	309.13	344.25	408.67	505.48	634.98	796.70
H H H H H	272.53	303.41	360.04	445.13	558.82	700.59
C G C G C	562.41	626.12	743.00	918.68	1153.52	1446.48
G C G C G	395.92	441.32	524.33	648.90	815.42	1023.46
C G G G C	549.66	611.78	725.75	896.99	1125.68	1410.55
G C C C G	405.73	452.32	537.50	665.33	836.30	1050.04
C H C H C	588.04	654.81	777.16	960.89	1206.30	1512.25
H C H C H	382.41	424.56	502.80	621.52	781.30	981.64
C H H H C	590.61	657.43	779.91	963.70	1208.85	1513.81
H C C C H	381.92	424.06	502.29	621.06	781.02	981.82
G H G H G	311.45	347.07	412.20	509.85	640.24	802.83
H G H G H	274.30	304.80	361.18	446.42	560.83	703.94
G H H H G	319.61	356.13	422.89	522.97	656.50	822.90
H G G G H	267.40	297.14	352.13	435.32	547.03	686.86

Table 4.35. Natural Frequencies of fully clamped rectangular plates (Hz), ($a/b=4$)

Stacking Sequence	Mode Number 1	2	3	4	5	6
C C C C C	1095.18	1158.50	1273.04	1446.84	1684.72	1988.96
G G G G G	535.52	566.51	622.55	707.59	823.99	972.89
H H H H H	470.89	498.00	547.07	621.54	723.44	853.65
C G C G C	972.37	1028.36	1129.72	1283.58	1494.17	1763.39
G C G C G	687.05	727.29	799.89	909.79	1060.02	1252.11
C G G G C	948.09	1002.47	1100.95	1250.47	1455.06	1716.35
G C C C G	704.89	746.28	820.92	933.90	1088.34	1285.91
C H C H C	1016.07	1074.73	1180.82	1341.73	1561.81	1842.96
H C H C H	663.86	700.88	768.48	872.02	1014.85	1198.63
C H H H C	1016.96	1075.32	1180.97	1341.24	1560.32	1839.77
H C C C H	664.10	701.22	768.98	872.77	1016.00	1200.45
G H G H G	538.86	570.27	626.97	712.80	830.05	979.78
H G H G H	475.00	501.75	550.44	624.80	727.08	858.32
G H H H G	552.31	584.44	642.46	730.27	850.21	1003.27
H G G G H	463.54	489.67	537.24	609.88	709.84	838.18

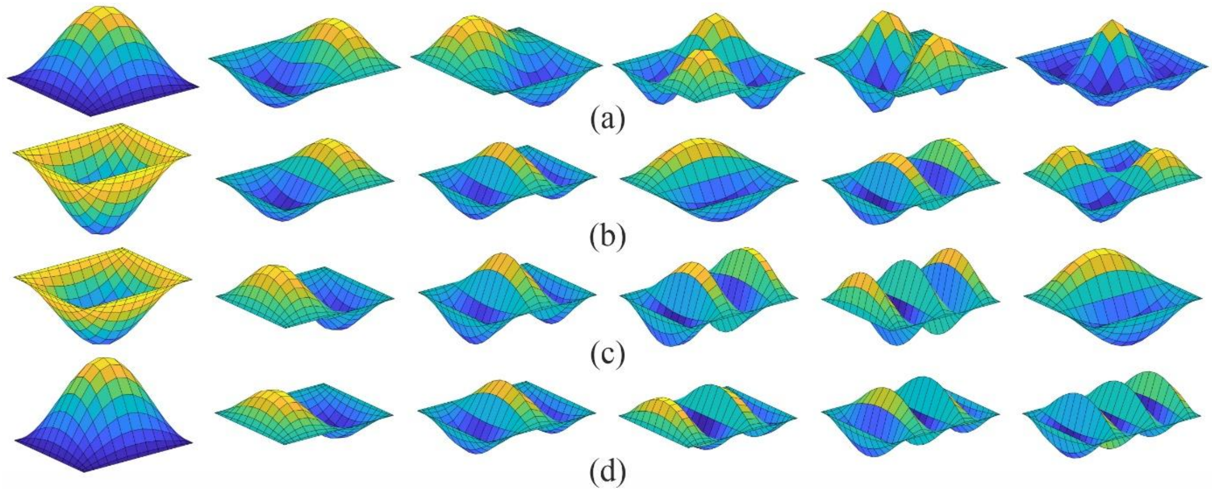

Figure 4.14. Mode shapes (first six modes) for simply supported plates, **a)** $a/b=1$, **b)** $a/b=2$, **c)** $a/b=3$, **d)** $a/b=4$

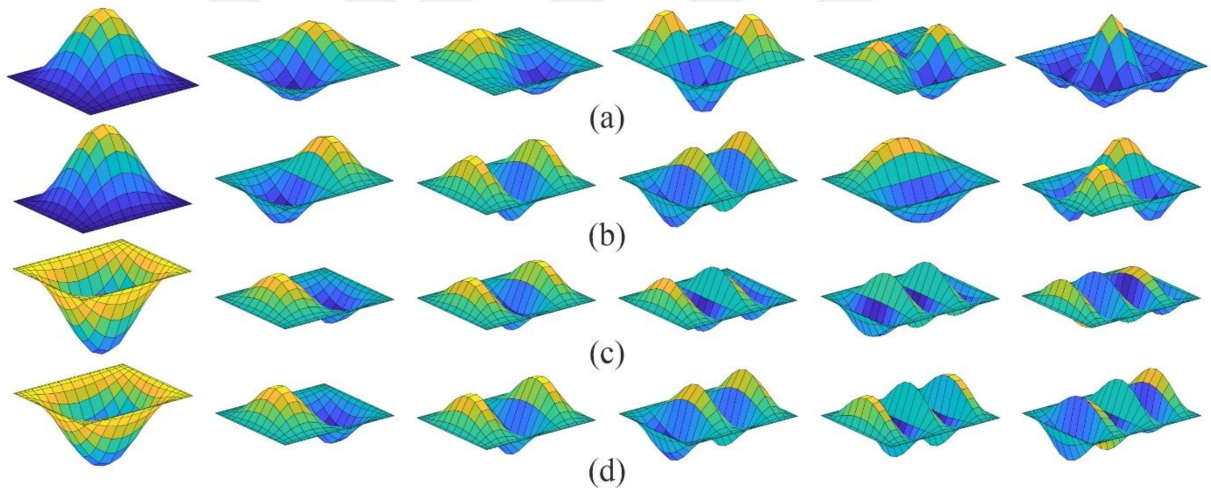

Figure 4.15. Mode shapes (first six modes) for fully clamped plates, **a)** $a/b=1$, **b)** $a/b=2$, **c)** $a/b=3$, **d)** $a/b=4$

4.4.2.2. Nonlinear Free Vibration Analysis Results

Nonlinear free vibration analysis results of the composite plates are presented in this section for the same stacking sequences, aspect ratios, and boundary conditions as in the linear vibration analysis section. The nonlinear-to-linear frequency ratios (ω_{NL}/ω_L) for fundamental frequencies are presented as a function of the maximum amplitude-to-thickness ratio ($w_{\max}/h$

) in Tables 4.36-4.43. In these tables, fundamental linear frequency values (ω_L) are also presented to interpret the results and frequency ratios more clearly. In Figures 4.16-4.23, the frequency ratio values of the relevant plates are also presented as graphs to see the effects of amplitude on the frequency parameter clearly. As the dimensionless amplitude increases, the frequency ratios also increase for all plates, regardless of the aspect ratios and boundary conditions. However, when looking at the simply supported plate results, the nonlinear fundamental frequency rises at a noticeably faster rate compared to the fully clamped plate results as the amplitude increases. Thus, changes in the amplitude have a more significant impact on the nonlinear frequencies for the simply supported cases than for fully clamped ones, and this situation is consistent with previous studies [145], [169]. Also, as the aspect ratio increases, the frequency ratios increase for all plates. The effect of stacking sequence and material properties on frequency ratios at lower amplitudes is relatively small, with only slight differences between the results. When the amplitude increases, the effect of the stacking sequence and material type becomes more apparent. Pure carbon, glass, and hemp fiber-reinforced composite plates exhibit relatively close frequency ratio values, regardless of the aspect ratio and boundary condition. However, the hybridization of different fibers has a significant effect on frequency ratios. As can be seen from the tables, carbon/glass hybrid composite plates and carbon/hemp hybrid plates have relatively close frequency ratios for CGCGC and CHCHC stacking sequences. There are also slight differences between the frequency ratio values of CGGGC and CHHHC stacking sequences. On the other hand, when the stacking sequences of GCGCG and HCHCH are compared, the difference in frequency ratio values becomes more apparent, as it does in the stacking sequences of GCCCG and HCCCH, especially at higher amplitudes. Moreover, regardless of the aspect ratio and boundary condition, each table shows that the CHHHC sequence has the lowest frequency ratio value, while the HCCCH sequence has the highest for all amplitude values. Lastly, glass/hemp hybrid plates have slightly higher frequency ratio values than those of CHCHC and CHHHC sequences, while they have lower frequency ratio values than those of HCHCH and HCCCH sequences.

Table 4.36. Frequency ratios of fundamental mode for simply supported square plates

Stacking Sequence	ω_L (Hz)	Frequency Ratios (ω_{NL}/ω_L) ($a/b=1$)							
		$w_{\max}/h$							
		0.2	0.4	0.6	0.8	1.0	1.2	1.4	1.6
C C C C C	60.20	1.0157	1.0617	1.1346	1.2311	1.3480	1.4812	1.6270	1.7842
G G G G G	29.40	1.0154	1.0607	1.1326	1.2277	1.3429	1.4745	1.6185	1.7738
H H H H H	26.04	1.0165	1.0650	1.1415	1.2426	1.3648	1.5039	1.6557	1.8209
C G C G C	53.58	1.0131	1.0518	1.1144	1.1961	1.2958	1.4117	1.5400	1.6770
G C G C G	37.71	1.0203	1.0800	1.1731	1.2946	1.4407	1.6042	1.7825	1.9767
C G G G C	52.48	1.0106	1.0418	1.0925	1.1597	1.2423	1.3387	1.4461	1.5636
G C C C G	38.61	1.0252	1.0983	1.2111	1.3578	1.5309	1.7225	1.9338	2.1558
C H C H C	56.12	1.0127	1.0502	1.1109	1.1903	1.2873	1.4001	1.5251	1.6590
H C H C H	35.93	1.0238	1.0932	1.2005	1.3393	1.5058	1.6898	1.8923	2.1052
C H H H C	56.55	1.0097	1.0384	1.0852	1.1473	1.2240	1.3127	1.4136	1.5234
H C C C H	35.83	1.0309	1.1201	1.2555	1.4301	1.6325	1.8587	2.1003	2.3567
G H G H G	29.74	1.0143	1.0565	1.1235	1.2126	1.3198	1.4445	1.5821	1.7279
H G H G H	25.94	1.0181	1.0713	1.1548	1.2646	1.3969	1.5471	1.7097	1.8871
G H H H G	30.56	1.0131	1.0519	1.1144	1.1961	1.2958	1.4118	1.5401	1.6771
H G G G H	25.26	1.0197	1.0775	1.1679	1.2861	1.4284	1.5893	1.7622	1.9517

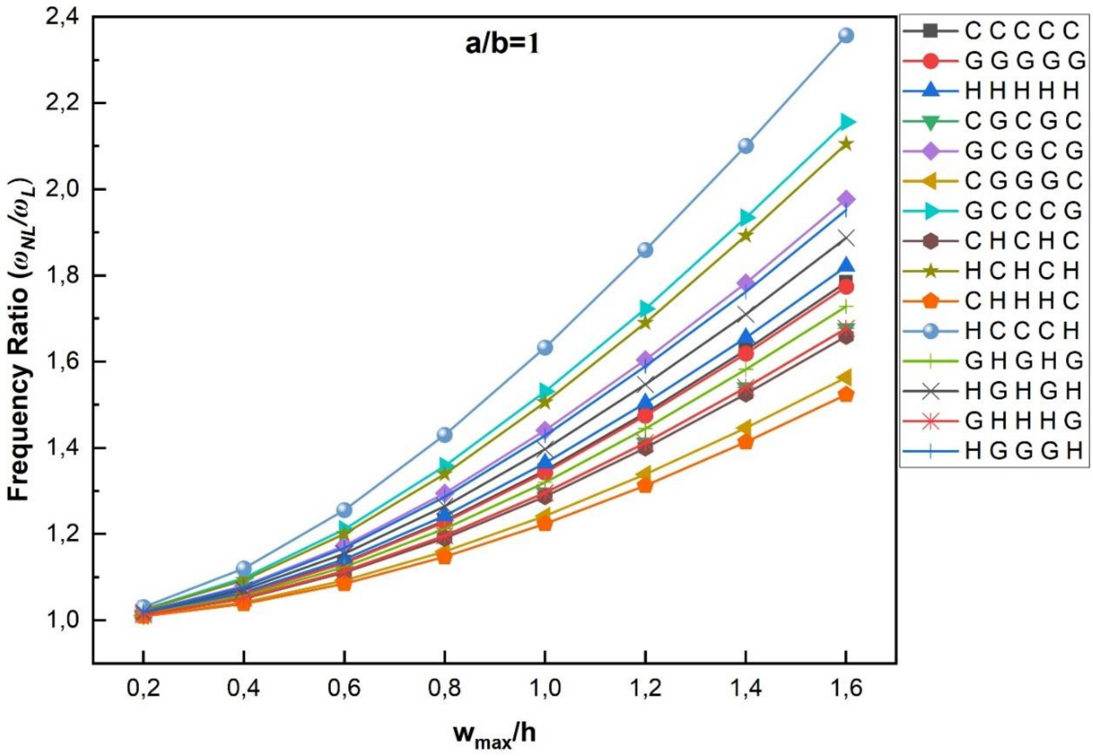

Figure 4.16. Frequency ratios of fundamental mode for simply supported square plates

Table 4.37. Frequency ratios of fundamental mode for simply supported rectangular plates

Stacking Sequence	ω_L (Hz)	Frequency Ratios (ω_{NL} / ω_L) ($a / b = 2$)							
		$w_{\max} / h$							
		0.2	0.4	0.6	0.8	1.0	1.2	1.4	1.6
C C C C C	150.26	1.0197	1.0786	1.1726	1.2978	1.4502	1.6256	1.8210	2.0317
G G G G G	73.38	1.0196	1.0769	1.1715	1.2959	1.4474	1.6219	1.8162	2.0261
H H H H H	65.00	1.0201	1.0800	1.1756	1.3029	1.4579	1.6358	1.8343	2.0477
C G C G C	133.75	1.0166	1.0651	1.1460	1.2528	1.3837	1.5354	1.7052	1.8905
G C G C G	94.02	1.0261	1.1022	1.2228	1.3811	1.5734	1.7928	2.0298	2.2851
C G G G C	130.99	1.0133	1.0526	1.1184	1.2062	1.3142	1.4405	1.5828	1.7390
G C C C G	96.28	1.0319	1.1254	1.2716	1.4629	1.6903	1.9472	2.2248	2.5174
C H C H C	140.02	1.0160	1.0629	1.1410	1.2443	1.3711	1.5182	1.6831	1.8633
H C H C H	90.16	1.0296	1.1166	1.2532	1.4326	1.6469	1.8902	2.1546	2.4339
C H H H C	141.07	1.0121	1.0479	1.1081	1.1886	1.2878	1.4043	1.5358	1.6806
H C C C H	89.92	1.0385	1.1505	1.3244	1.5496	1.8148	2.1115	2.4284	2.7581
G H G H G	74.14	1.0180	1.0708	1.1582	1.2734	1.4142	1.5768	1.7581	1.9554
H G H G H	64.98	1.0225	1.0891	1.1952	1.3357	1.5062	1.7011	1.9174	2.1490
G H H H G	76.17	1.0164	1.0645	1.1445	1.2502	1.3799	1.5301	1.6983	1.8818
H G G G H	63.27	1.0247	1.0977	1.2133	1.3661	1.5508	1.7610	1.9933	2.2406

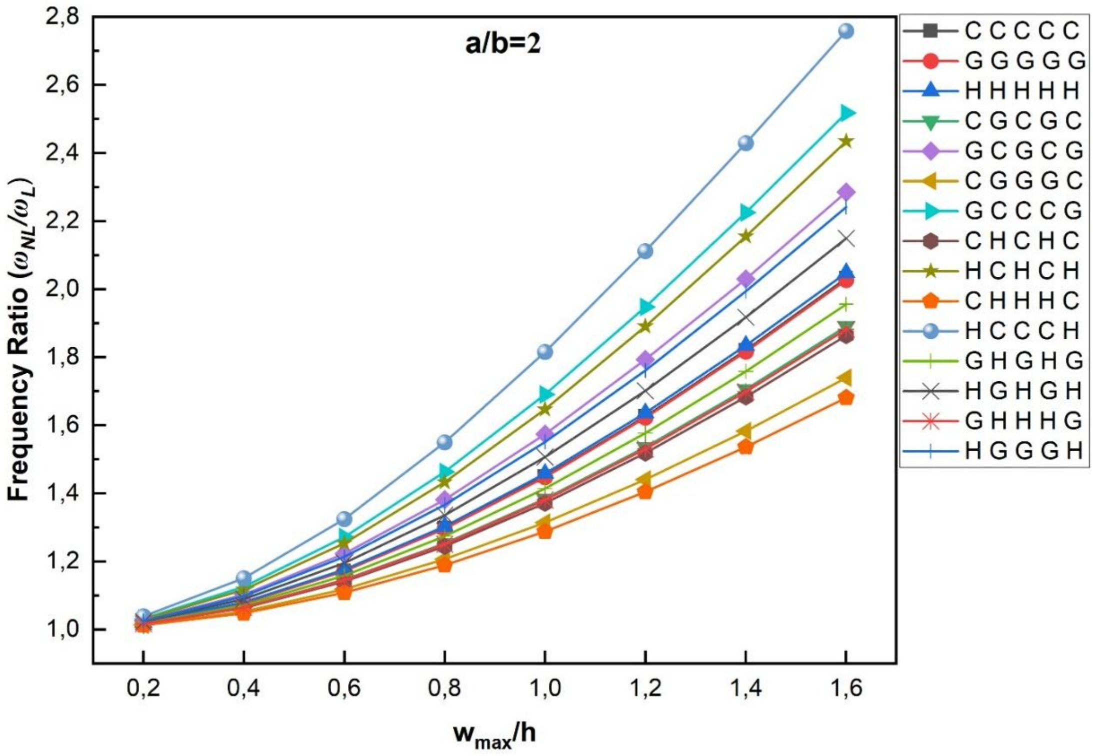

Figure 4.17. Frequency ratios of fundamental mode for simply supported rectangular plates

Table 4.38. Frequency ratios of fundamental mode for simply supported rectangular plates

Stacking Sequence	ω_L (Hz)	Frequency Ratios (ω_{NL} / ω_L) ($a/b=3$)							
		$w_{\max} / h$							
		0.2	0.4	0.6	0.8	1.0	1.2	1.4	1.6
C C C C C	300.44	1.0236	1.0939	1.2109	1.3724	1.5739	1.8037	2.0501	2.3068
G G G G G	146.75	1.0235	1.0936	1.2104	1.3715	1.5728	1.8024	2.0487	2.3038
H H H H H	129.89	1.0237	1.0942	1.2117	1.3738	1.5763	1.8056	2.0545	2.3138
C G C G C	267.47	1.0198	1.0789	1.1776	1.3144	1.4864	1.6883	1.9067	2.1380
G C G C G	187.85	1.0310	1.1229	1.2750	1.4827	1.7347	2.0128	2.3057	2.6064
C G G G C	261.92	1.0159	1.0637	1.1435	1.2548	1.3960	1.5648	1.7513	1.9520
G C C C G	192.35	1.0383	1.1513	1.3374	1.5882	1.8832	2.2023	2.5335	2.8729
C H C H C	279.88	1.0190	1.0760	1.1710	1.3030	1.4691	1.6648	1.8771	2.1032
H C H C H	180.95	1.0351	1.1389	1.3108	1.5443	1.8217	2.1249	2.4390	2.7617
C H H H C	281.94	1.0144	1.0586	1.1302	1.2314	1.3603	1.5150	1.6878	1.8746
H C C C H	180.47	1.0458	1.1808	1.4023	1.6953	2.0302	2.3867	2.7550	3.1311
G H G H G	148.11	1.0215	1.0857	1.1927	1.3406	1.5264	1.7407	1.9721	2.2154
H G H G H	130.21	1.0266	1.1057	1.2372	1.4184	1.6421	1.8928	2.1604	2.4353
G H H H G	152.15	1.0195	1.0777	1.1749	1.3097	1.4790	1.6780	1.8933	2.1225
H G G G H	126.81	1.0293	1.1165	1.2611	1.4594	1.7017	1.9702	2.2539	2.5447

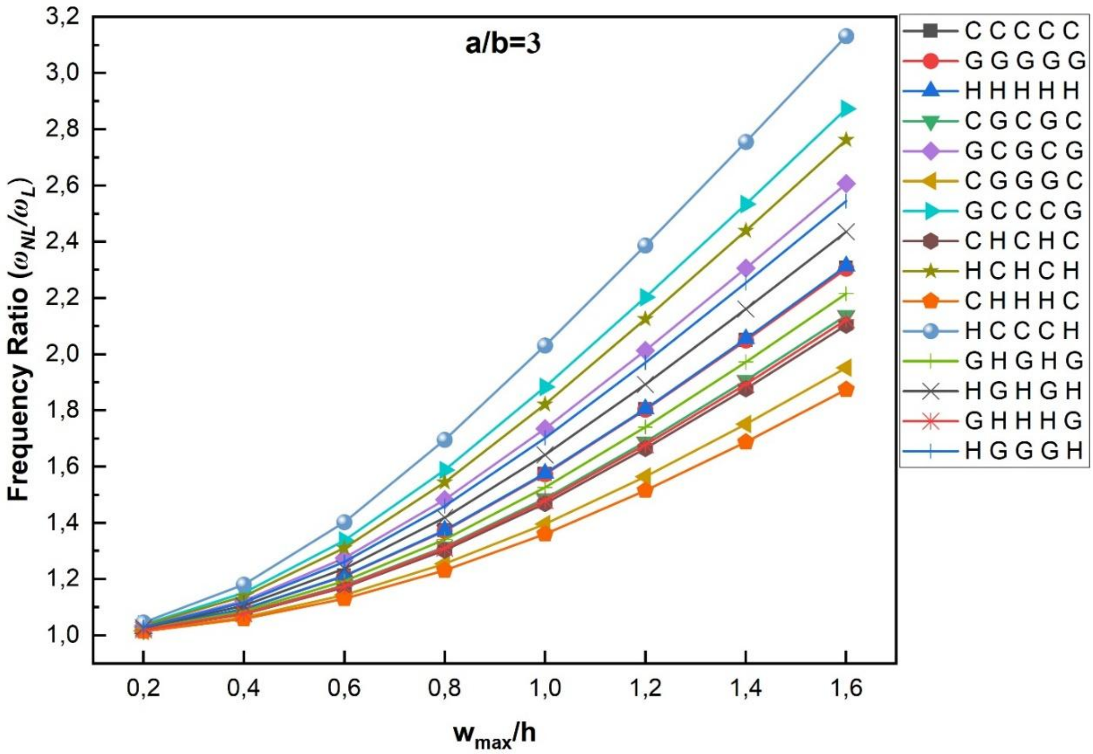

Figure 4.18. Frequency ratios of fundamental mode for simply supported rectangular plates

Table 4.39. Frequency ratios of fundamental mode for simply supported rectangular plates

		Frequency Ratios (ω_{NL} / ω_L) ($a/b=4$)							
		$w_{\max}/h$							
Stacking Sequence	ω_L (Hz)	0.2	0.4	0.6	0.8	1.0	1.2	1.4	1.6
C C C C C	510.21	1.0258	1.1054	1.2450	1.4416	1.6700	1.9204	2.1803	2.4389
G G G G G	249.24	1.0257	1.1053	1.2447	1.4413	1.6694	1.9198	2.1784	2.4358
H H H H H	220.44	1.0258	1.1055	1.2451	1.4418	1.6720	1.9210	2.1835	2.4408
C G C G C	454.15	1.0216	1.0883	1.2052	1.3728	1.5747	1.7956	2.0261	2.2580
G C G C G	318.97	1.0340	1.1393	1.3222	1.5684	1.8458	2.1419	2.4457	2.7601
C G G G C	444.58	1.0174	1.0709	1.1647	1.3009	1.4710	1.6614	1.8670	2.0710
G C C C G	326.65	1.0421	1.1724	1.3972	1.6845	2.0044	2.3401	2.6904	3.0233
C H C H C	475.10	1.0208	1.0849	1.1973	1.3588	1.5553	1.7706	2.0012	2.2244
H C H C H	307.88	1.0384	1.1574	1.3648	1.6331	1.9344	2.2518	2.4629	2.8455
C H H H C	478.34	1.0158	1.0642	1.1489	1.2723	1.4284	1.6068	1.7981	1.9865
H C C C H	307.15	1.0495	1.2069	1.4716	1.7977	2.1530	2.5286	2.8993	3.2724
G H G H G	251.40	1.0235	1.0960	1.2231	1.4039	1.6179	1.8529	2.1008	2.3438
H G H G H	221.33	1.0290	1.1189	1.2762	1.4936	1.7421	2.0125	2.2694	2.3708
G H H H G	258.19	1.0213	1.0868	1.2016	1.3664	1.5656	1.7845	2.0044	2.2452
H G G G H	215.60	1.0321	1.1315	1.3051	1.5408	1.8076	2.0931	2.3018	2.5367

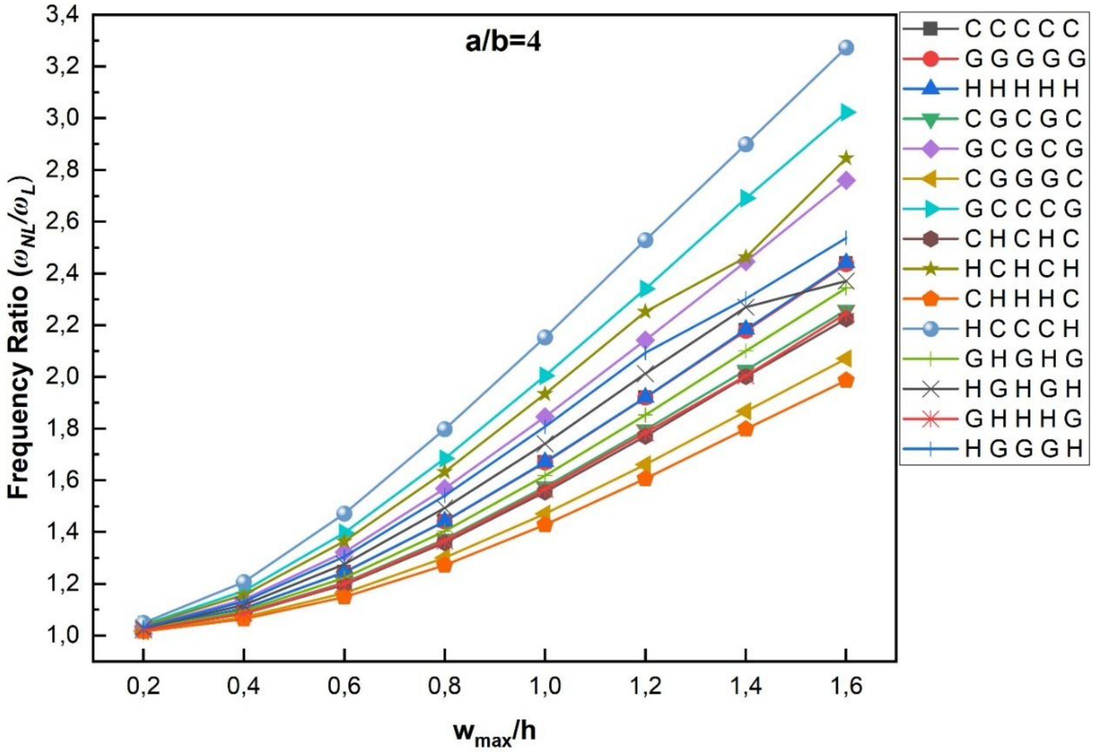

Figure 4.19. Frequency ratios of fundamental mode for simply supported rectangular plates

Table 4.40. Frequency ratios of fundamental mode for fully clamped square plates

		Frequency Ratios (ω_{NL} / ω_L) ($a/b=1$)							
		w_{max} / h							
Stacking Sequence	ω_L (Hz)	0.2	0.4	0.6	0.8	1.0	1.2	1.4	1.6
C C C C C	110.14	1.0071	1.0281	1.0619	1.1080	1.1642	1.2294	1.3012	1.3798
G G G G G	53.81	1.0070	1.0278	1.0613	1.1069	1.1626	1.2272	1.2983	1.3761
H H H H H	47.58	1.0072	1.0288	1.0635	1.1108	1.1685	1.2355	1.3093	1.3901
C G C G C	98.11	1.0059	1.0235	1.0521	1.0912	1.1392	1.1951	1.2581	1.3258
G C G C G	68.84	1.0093	1.0367	1.0805	1.1396	1.2108	1.2916	1.3811	1.4773
C G G G C	96.15	1.0048	1.0190	1.0421	1.0736	1.1132	1.1594	1.2118	1.2696
G C C C G	70.45	1.0115	1.0452	1.0992	1.1702	1.2555	1.3510	1.4562	1.5704
C H C H C	102.69	1.0057	1.0228	1.0505	1.0883	1.1348	1.1892	1.2505	1.3165
H C H C H	66.15	1.0106	1.0416	1.0915	1.1576	1.2373	1.3271	1.4362	1.5340
C H H H C	103.56	1.0044	1.0173	1.0385	1.0674	1.1039	1.1466	1.1951	1.2488
H C C C H	65.94	1.0138	1.0539	1.1178	1.2012	1.2996	1.4105	1.5326	1.6622
G H G H G	54.34	1.0065	1.0257	1.0569	1.0993	1.1512	1.2117	1.2786	1.3520
H G H G H	47.65	1.0081	1.0318	1.0700	1.1219	1.1848	1.2576	1.3372	1.4240
G H H H G	55.85	1.0059	1.0235	1.0520	1.0909	1.1388	1.1947	1.2576	1.3252
H G G G H	46.39	1.0088	1.0348	1.0764	1.1328	1.2009	1.2784	1.3645	1.4574

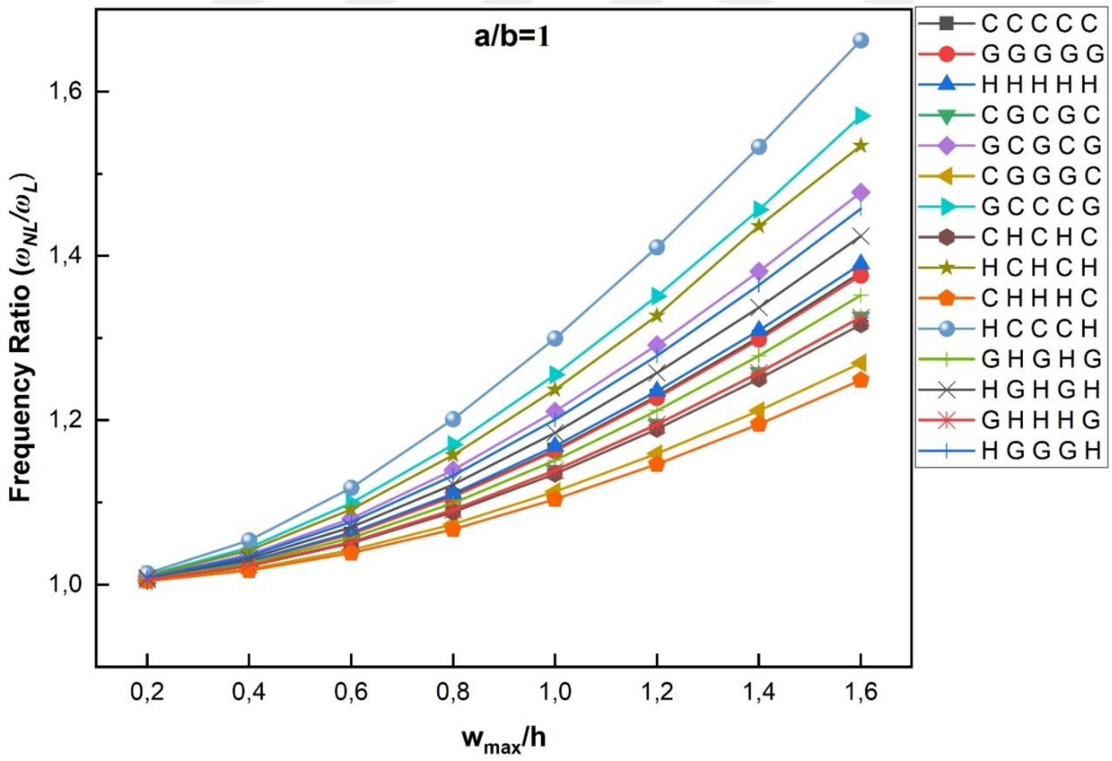

Figure 4.20. Frequency ratios of fundamental mode for fully clamped square plates

Table 4.41. Frequency ratios of fundamental mode for fully clamped rectangular plates

Stacking Sequence	ω_L (Hz)	Frequency Ratios (ω_{NL} / ω_L) ($a/b=2$)							
		$w_{\max}/h$							
		0.2	0.4	0.6	0.8	1.0	1.2	1.4	1.6
C C C C C	299.78	1.0074	1.0291	1.0641	1.1175	1.1811	1.2562	1.3407	1.4338
G G G G G	146.48	1.0073	1.0289	1.0638	1.1170	1.1802	1.2550	1.3391	1.4318
H H H H H	129.38	1.0074	1.0293	1.0648	1.1185	1.1827	1.2586	1.3440	1.4380
C G C G C	266.87	1.0062	1.0244	1.0539	1.0939	1.1530	1.2172	1.2907	1.3709
G C G C G	187.42	1.0097	1.0381	1.0838	1.1529	1.2344	1.3298	1.4350	1.5511
C G G G C	261.28	1.0050	1.0197	1.0435	1.0759	1.1242	1.1768	1.2375	1.3046
G C C C G	191.90	1.0120	1.0470	1.1029	1.1871	1.2854	1.3981	1.5239	1.6575
C H C H C	279.19	1.0060	1.0235	1.0520	1.0906	1.1478	1.2099	1.2811	1.3590
H C H C H	180.72	1.0111	1.0440	1.0982	1.1717	1.2627	1.3675	1.4846	1.6114
C H H H C	281.13	1.0045	1.0179	1.0396	1.0692	1.1133	1.1614	1.2170	1.2789
H C C C H	180.27	1.0145	1.0573	1.1272	1.2211	1.3351	1.4658	1.6094	1.7613
G H G H G	147.76	1.0067	1.0266	1.0587	1.1021	1.1661	1.2355	1.3138	1.4005
H G H G H	129.91	1.0083	1.0327	1.0721	1.1319	1.2029	1.2866	1.3800	1.4836
G H H H G	151.77	1.0061	1.0242	1.0534	1.0930	1.1514	1.2150	1.2878	1.3672
H G G G H	126.54	1.0092	1.0360	1.0792	1.1447	1.2221	1.3132	1.4140	1.5257

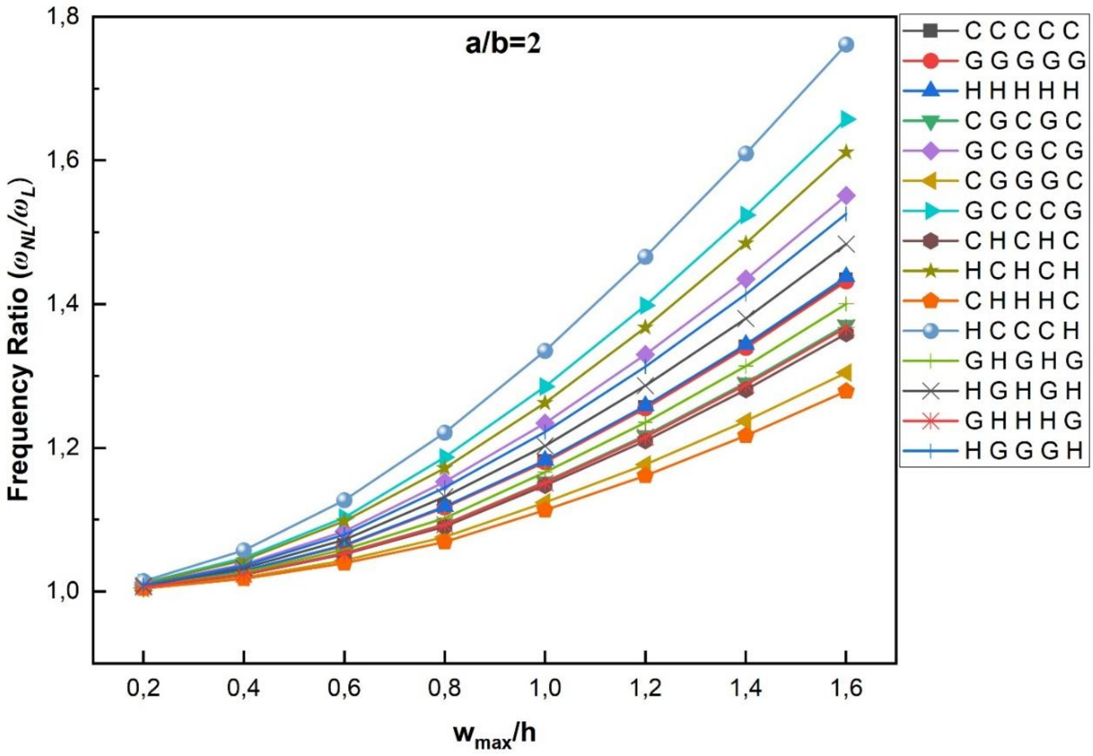

Figure 4.21. Frequency ratios of fundamental mode for fully clamped rectangular plates

Table 4.42. Frequency ratios of fundamental mode for fully clamped rectangular plates

Stacking Sequence	ω_L (Hz)	Frequency Ratios (ω_{NL} / ω_L) ($a/b=3$) w_{max}/h 0.2	0.4	0.6	0.8	1.0	1.2	1.4	1.6
C C C C C	632.46	1.0076	1.0302	1.0675	1.1341	1.2108	1.3044	1.4069	1.5170
G G G G G	309.13	1.0075	1.0301	1.0673	1.1337	1.2103	1.3037	1.4061	1.5160
H H H H H	272.53	1.0078	1.0320	1.0736	1.1341	1.2123	1.3047	1.4070	1.5190
C G C G C	562.41	1.0064	1.0253	1.0565	1.1121	1.1772	1.2571	1.3457	1.4428
G C G C G	395.92	1.0103	1.0421	1.0973	1.1763	1.2759	1.3906	1.5155	1.6476
C G G G C	549.66	1.0051	1.0203	1.0454	1.0899	1.1427	1.2079	1.2825	1.3657
G C C C G	405.73	1.0124	1.0492	1.1207	1.2168	1.3378	1.4713	1.6170	1.7661
C H C H C	588.04	1.0061	1.0243	1.0544	1.1079	1.1706	1.2478	1.3338	1.4282
H C H C H	382.41	1.0112	1.0448	1.1098	1.1981	1.3102	1.4352	1.5721	1.7128
C H H H C	590.61	1.0047	1.0184	1.0411	1.0814	1.1298	1.1879	1.2577	1.3326
H C C C H	381.92	1.0151	1.0621	1.1439	1.2582	1.3966	1.5484	1.7114	1.8782
G H G H G	311.45	1.0072	1.0292	1.0670	1.1219	1.1933	1.2779	1.3737	1.4778
H G H G H	274.30	1.0085	1.0339	1.0762	1.1512	1.2377	1.3388	1.4508	1.5713
G H H H G	319.61	1.0065	1.0264	1.0606	1.1102	1.1751	1.2525	1.3413	1.4360
H G G G H	267.40	1.0094	1.0375	1.0917	1.1661	1.2617	1.3709	1.4926	1.6181

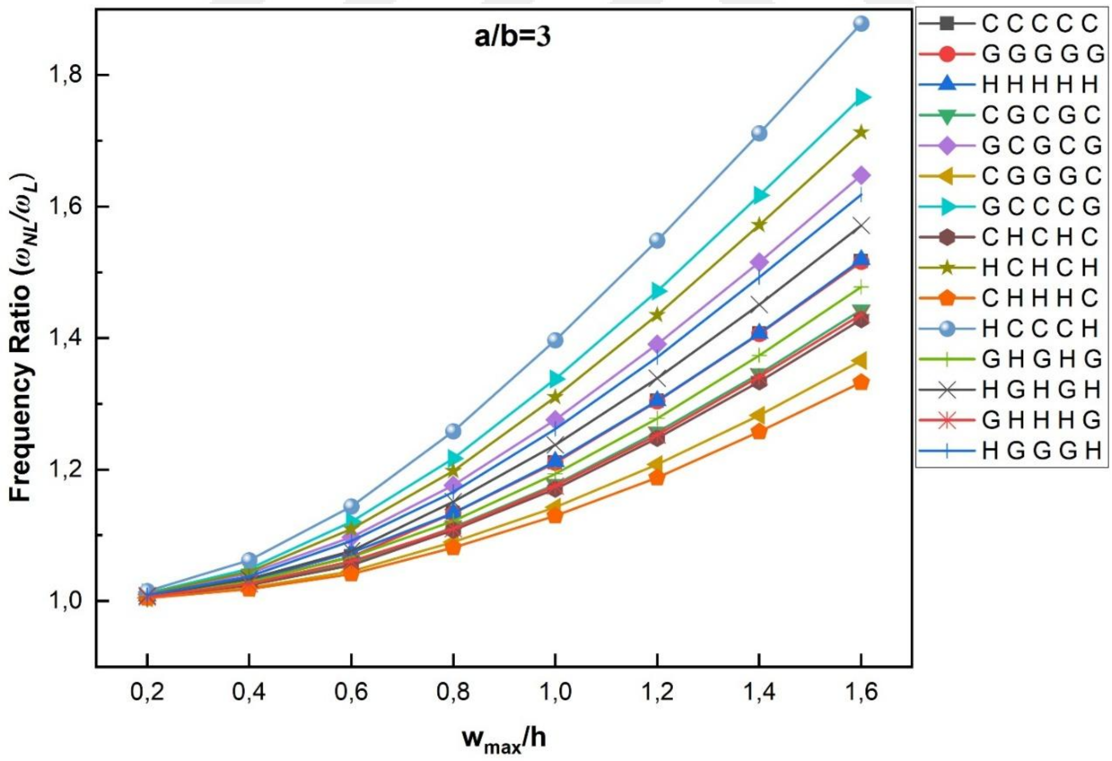

Figure 4.22. Frequency ratios of fundamental mode for fully clamped rectangular plates

Table 4.43. Frequency ratios of fundamental mode for fully clamped rectangular plates

Stacking Sequence	ω_L (Hz)	Frequency Ratios (ω_{NL}/ω_L) ($a/b=4$) w_{max}/h 0.2	0.4	0.6	0.8	1.0	1.2	1.4	1.6
C C C C C	1095.2	1.0082	1.0344	1.0829	1.1536	1.2422	1.3420	1.4411	1.5381
G G G G G	535.52	1.0081	1.0343	1.0828	1.1533	1.2421	1.3417	1.4390	1.5369
H H H H H	470.89	1.0082	1.0345	1.0835	1.1550	1.2432	1.3436	1.4536	1.5405
C G C G C	972.37	1.0068	1.0287	1.0689	1.1283	1.2056	1.2928	1.3843	1.4463
G C G C G	687.05	1.0107	1.0457	1.1106	1.2026	1.3125	1.4341	1.5589	1.6525
C G G G C	948.09	1.0052	1.0208	1.0550	1.1025	1.1653	1.2395	1.3185	1.3886
G C C C G	704.89	1.0126	1.0516	1.1367	1.2476	1.3765	1.5184	1.6616	1.7748
C H C H C	1016.1	1.0063	1.0250	1.0664	1.1239	1.1981	1.2822	1.3734	1.4259
H C H C H	663.86	1.0115	1.0468	1.1245	1.2274	1.3466	1.4736	1.5479	1.6192
C H H H C	1017.0	1.0050	1.0209	1.0494	1.0931	1.1494	1.2189	1.2921	1.3509
H C C C H	664.10	1.0158	1.0688	1.1646	1.2913	1.4374	1.5895	1.7635	1.9346
G H G H G	538.86	1.0074	1.0313	1.0752	1.1397	1.2225	1.3152	1.4158	1.4861
H G H G H	475.00	1.0087	1.0351	1.0936	1.1732	1.2709	1.3729	1.4341	1.4975
G H H H G	552.31	1.0064	1.0256	1.0679	1.1266	1.2023	1.2875	1.3789	1.4360
H G G G H	463.54	1.0096	1.0389	1.1038	1.1909	1.2966	1.4098	1.4859	1.5356

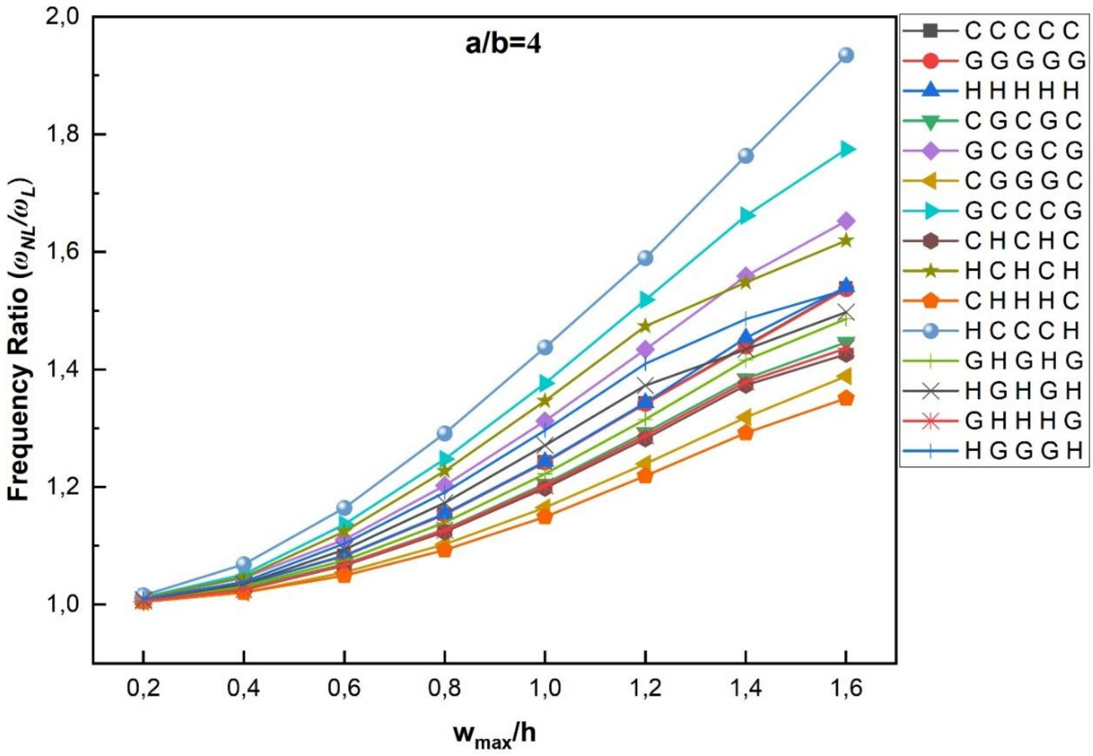

Figure 4.23. Frequency ratios of fundamental mode for fully clamped rectangular plates

5. CONCLUSIONS

In this study, the free vibration behavior of hemp-based laminated composite structures was investigated both numerically and experimentally. The scope included two main structural configurations: curved composite beams and rectangular laminated composite plates. The research aimed to evaluate the dynamic performance of pure and hybrid hemp fiber-reinforced composites and to explore the potential of hemp fibers as a sustainable alternative to traditional synthetic reinforcements, especially glass fiber. The governing equations for the free vibration of curved beams and laminated rectangular plates, formulated within the framework of FSDT, were derived employing the principle of virtual work. The large amplitude free vibration equation of plates was derived using the nonlinear Green-Lagrange strains. Spatial derivatives within the vibration equation were calculated using the GDQ method. Parametric studies were conducted to assess the effects of curvature ratio, aspect ratio, stacking sequence, boundary conditions, and hybridization on natural frequencies. The numerical models were validated through experimental testing and comparison with results reported in the literature, demonstrating strong consistency and reliability. Experimental tensile tests were conducted on hemp, carbon, and glass fiber laminates to determine their mechanical properties. Vibration tests were then carried out on nine different composite specimens produced using the VARTM method. The first-mode natural frequencies and damping ratios of these specimens were obtained using a vibration measurement setup. The experimental results were in strong agreement with numerical calculations for test specimens, verifying the accuracy of the GDQ-based models.

Key findings obtained from this study are summarized below:

- Among all vibration test specimens, the pure hemp composite beam exhibited the highest damping ratio, while the pure carbon composite beam showed the lowest. This aligns with prior literature and highlights the intrinsic vibration-damping advantage of hemp fibers.
- For vibration test specimens, placing hemp fibers on the outer layers (e.g., in HCH and HGH configurations), higher damping ratios were obtained compared to when they

were located centrally (CHC and GHG). This indicates that the outer layer material plays a dominant role in energy dissipation.

- Among vibration test specimens, the pure carbon composite beam (CCC) had the highest fundamental natural frequency, while the pure hemp composite (HHH) had the lowest. However, the carbon/hemp fiber hybrid beam CHC had the second highest natural frequency value after the CCC beam, and this value was slightly higher than that of the carbon/glass hybrid beam CGC, demonstrating the advantage of carbon-hemp hybridization.
- Pure glass and pure hemp fiber-reinforced composite beams and plates exhibited comparable frequency values. This suggests that hemp fiber-reinforced composites could serve as a practical alternative to traditional glass fiber-reinforced composites in vibration-related applications.
- Hybridizing hemp fibers with carbon or glass fibers and arranging the layers such that the hemp fibers are placed near the neutral axis, while carbon or glass fibers are placed on the outer layers, leads to an increase in natural frequency values compared to pure hemp composite curved beams and rectangular plates.
- Hybrid composite curved beams and rectangular plates reinforced with carbon/hemp fibers exhibit slightly higher natural frequency values compared to those reinforced with carbon/glass fibers, especially for CHCHC and CHHHC stacking sequences, regardless of the boundary conditions.
- S-S and C-C boundary conditions have a more significant effect on fundamental modes than the others for curved beams. In general, fundamental frequency values increase as the curvature ratio rises, up to a certain threshold (0.6-0.8 for S-S and 0.8-1 for C-C). Beyond this point, a slight decline in frequency values is observed with further increases in curvature ratio.
- Aspect ratio and boundary condition have a remarkable effect on both linear and nonlinear vibration behaviors of the composite plates.
- The nonlinear fundamental frequency values for simply supported plates increase at a noticeably faster rate compared to fully clamped plates as the amplitude increases.
- For nonlinear modal analyses, composite plates consisting of pure carbon, glass, and hemp fibers have relatively close frequency ratios (ω_{NL} / ω_{L}) values, for all amplitude

values, irrespective of the aspect ratio and boundary conditions. Furthermore, the CHHHC sequence has the lowest frequency ratio, whereas the HCCCH sequence has the highest.

- For nonlinear modal analyses, the hybridization of different fibers significantly impacts the frequency ratios (ω_{NL} / ω_{L}). Carbon/glass and carbon/hemp hybrid composite plates exhibit very similar frequency ratio values for CGCGC and CHCHC stacking sequences, as in the stacking sequences of CGGGC and CHHHC.
- In general, regardless of the stacking sequences, hybridizing the lower mechanical property fiber material with a higher one has an increasing effect on the natural frequency values. For further increase, positioning fiber materials with higher mechanical properties on the outer layers tends to enhance the natural frequency values.

With these results, it was demonstrated that hemp fiber-reinforced composites, especially in hybrid form, can be considered a viable material choice for dynamic structural applications. The GDQ method proves to be an efficient and accurate approach for vibration analysis, offering lower computational cost compared to conventional methods like FEM.

This research contributes to the existing literature by addressing the dynamic performance of hemp-based composites in both beam and plate configurations, a relatively underexplored area. The combined experimental and numerical approach presented here offers valuable insights for the development and optimization of environmentally friendly composite materials in engineering design.

REFERENCES

[1] S. Mazumdar, *Composites Manufacturing*, 1st Edition. Boca Raton: CRC Press, 2001. doi: 10.1201/9781420041989.

[2] A. K. Kaw, *Mechanics of Composite Materials*. Boca Raton: CRC Press, 2005. doi: 10.1201/9781420058291.

[3] A. W. McFarland, M. A. Poggi, L. A. Bottomley, and J. S. Colton, "Production and characterization of polymer microcantilevers," *Review of Scientific Instruments*, vol. 75, no. 8, pp. 2756–2758, Aug. 2004, doi: 10.1063/1.1777387.

[4] M. M. Dawoud and H. M. Saleh, "Introductory Chapter: Background on Composite Materials," in *Characterizations of Some Composite Materials*, IntechOpen, 2019. doi: 10.5772/intechopen.80960.

[5] H. Abramovich, *Stability and Vibrations of Thin-Walled Composite Structures*. Woodhead Publishing, 2017.

[6] S. A. Bello, J. O. Agunsoye, S. E. A. Hassan, and M. Z. Kana, "Epoxy resin based composites, mechanical and tribological properties: A review.," *Tribology in Industry*, vol. 37, no. 4, pp. 500–524, 2015.

[7] N. CHAWLA, R. SIDHU, and V. GANESH, "Three-dimensional visualization and microstructure-based modeling of deformation in particle-reinforced composites," *Acta Mater*, vol. 54, no. 6, pp. 1541–1548, Apr. 2006, doi: 10.1016/j.actamat.2005.11.027.

[8] P. S, S. KM, N. K, and S. S, "Fiber Reinforced Composites - A Review," *Journal of Material Science & Engineering*, vol. 06, no. 03, 2017, doi: 10.4172/2169-0022.1000341.

[9] G. Yang, M. Park, and S.-J. Park, "Recent progresses of fabrication and characterization of fibers-reinforced composites: A review," *Composites Communications*, vol. 14, pp. 34–42, Aug. 2019, doi: 10.1016/j.coco.2019.05.004.

[10] E. Omanović-Mikličanin, A. Badnjević, A. Kazlagić, and M. Hajlovac, "Nanocomposites: a brief review," *Health Technol (Berl)*, vol. 10, no. 1, pp. 51–59, Jan. 2020, doi: 10.1007/s12553-019-00380-x.

[11] K. U. Kainer, Ed., *Metal Matrix Composites*. Wiley, 2006. doi: 10.1002/3527608117.

[12] J. Binner *et al.*, "Selection, processing, properties and applications of ultra-high temperature ceramic matrix composites, UHTCMCs – a review," *International*

Materials Reviews, vol. 65, no. 7, pp. 389–444, Oct. 2020, doi: 10.1080/09506608.2019.1652006.

[13] A. Crosky, N. Soatthiyanon, D. Ruys, S. Meatherall, and S. Potter, “Thermoset matrix natural fibre-reinforced composites,” in *Natural Fibre Composites*, Elsevier, 2014, pp. 233–270. doi: 10.1533/9780857099228.2.233.

[14] Y. Qiao, L. D. Fring, M. R. Pallaka, and K. L. Simmons, “A review of the fabrication methods and mechanical behavior of continuous thermoplastic polymer fiber–thermoplastic polymer matrix composites,” *Polym Compos*, vol. 44, no. 2, pp. 694–733, Feb. 2023, doi: 10.1002/pc.27139.

[15] E. J. Barbero, *Introduction to Composite Materials Design, Third Edition*. CRC Press, 2017. doi: 10.1201/9781315296494.

[16] A. Vinod *et al.*, “Jute/Hemp bio-epoxy hybrid bio-composites: Influence of stacking sequence on adhesion of fiber-matrix,” *Int J Adhes Adhes*, vol. 113, p. 103050, Mar. 2022, doi: 10.1016/j.ijadhadh.2021.103050.

[17] M. Durante, A. Langella, A. Formisano, L. Boccarusso, and L. Carrino, “Dynamic-Mechanical Behaviour of Bio-composites,” *Procedia Eng*, vol. 167, pp. 231–236, 2016, doi: 10.1016/j.proeng.2016.11.692.

[18] M. C. Khoathane, O. C. Vorster, and E. R. Sadiku, “Hemp Fiber-Reinforced 1-Pentene/Polypropylene Copolymer: The Effect of Fiber Loading on the Mechanical and Thermal Characteristics of the Composites,” *Journal of Reinforced Plastics and Composites*, vol. 27, no. 14, pp. 1533–1544, Sep. 2008, doi: 10.1177/0731684407086325.

[19] A. Lotfi, H. Li, D. V. Dao, and G. Prusty, “Natural fiber–reinforced composites: A review on material, manufacturing, and machinability,” *Journal of Thermoplastic Composite Materials*, vol. 34, no. 2, pp. 238–284, Feb. 2021, doi: 10.1177/0892705719844546.

[20] T. H. Mokhothu and M. J. John, “Review on hygroscopic aging of cellulose fibres and their biocomposites,” *Carbohydr Polym*, vol. 131, pp. 337–354, Oct. 2015, doi: 10.1016/j.carbpol.2015.06.027.

[21] F. I. Mahir, K. N. Keya, B. Sarker, K. M. Nahiun, and R. A. Khan, “A brief review on natural fiber used as a replacement of synthetic fiber in polymer composites,” *Materials Engineering Research*, vol. 1, no. 2, pp. 88–99, 2019, doi: 10.25082/MER.2019.02.007.

[22] B. Dahlke, H. Larbig, H. D. Scherzer, and R. Poltrock, “Natural Fiber Reinforced Foams Based on Renewable Resources for Automotive Interior Applications,” *Journal of Cellular Plastics*, vol. 34, no. 4, pp. 361–379, Jul. 1998, doi: 10.1177/0021955X9803400406.

[23] M. Brebu, “Environmental Degradation of Plastic Composites with Natural Fillers—A Review,” *Polymers (Basel)*, vol. 12, no. 1, p. 166, Jan. 2020, doi: 10.3390/polym12010166.

[24] B. Rashid, Z. Leman, M. Jawaid, M. R. Ishak, and F. M. Al-Oqla, “Eco-Friendly Composites for Brake Pads From Agro Waste: A Review,” in *Encyclopedia of Materials: Composites*, Elsevier, 2017, pp. 209–228. doi: 10.1016/B978-0-12-803581-8.10159-6.

[25] E. Sarikaya, H. Çallioğlu, and H. Demirel, “Production of epoxy composites reinforced by different natural fibers and their mechanical properties,” *Compos B Eng*, vol. 167, pp. 461–466, Jun. 2019, doi: 10.1016/j.compositesb.2019.03.020.

[26] P. Wambua, J. Ivens, and I. Verpoest, “Natural fibres: can they replace glass in fibre reinforced plastics?,” *Compos Sci Technol*, vol. 63, no. 9, pp. 1259–1264, Jul. 2003, doi: 10.1016/S0266-3538(03)00096-4.

[27] K. G. Satyanarayana, G. G. C. Arizaga, and F. Wypych, “Biodegradable composites based on lignocellulosic fibers—An overview,” *Prog Polym Sci*, vol. 34, no. 9, pp. 982–1021, Sep. 2009, doi: 10.1016/j.progpolymsci.2008.12.002.

[28] M. J. Mochane *et al.*, “Recent progress on natural fiber hybrid composites for advanced applications: A review,” *Express Polym Lett*, vol. 13, no. 2, pp. 159–198, 2019, doi: 10.3144/expresspolymlett.2019.15.

[29] F. M. AL-Oqla and S. M. Sapuan, “Natural fiber reinforced polymer composites in industrial applications: feasibility of date palm fibers for sustainable automotive industry,” *J Clean Prod*, vol. 66, pp. 347–354, Mar. 2014, doi: 10.1016/j.jclepro.2013.10.050.

[30] H. Hajiha and M. Sain, “High toughness hybrid biocomposite process optimization,” *Compos Sci Technol*, vol. 111, pp. 44–49, May 2015, doi: 10.1016/j.compscitech.2015.03.002.

[31] P. Sature and Ashok Mache, “Mechanical characterization and water absorption studies on jute/hemp reinforced hybrid composites,” *American Journal of Materials Science*, vol. 5, no. 3C, pp. 133–139, 2015.

[32] M. M. Kabir, H. Wang, K. T. Lau, and F. Cardona, "Tensile properties of chemically treated hemp fibres as reinforcement for composites," *Compos B Eng*, vol. 53, pp. 362–368, Oct. 2013, doi: 10.1016/j.compositesb.2013.05.048.

[33] L. Pil, F. Bensadoun, J. Pariset, and I. Verpoest, "Why are designers fascinated by flax and hemp fibre composites?," *Compos Part A Appl Sci Manuf*, vol. 83, pp. 193–205, Apr. 2016, doi: 10.1016/j.compositesa.2015.11.004.

[34] H. N. Dhakal and Z. Zhang, "The use of hemp fibres as reinforcements in composites," *Biofiber Reinforcements in Composite Materials*, pp. 86–103, Jan. 2015, doi: 10.1533/9781782421276.1.86.

[35] M. M. Kabir, H. Wang, K. T. Lau, and F. Cardona, "Effects of chemical treatments on hemp fibre structure," *Appl Surf Sci*, vol. 276, pp. 13–23, Jul. 2013, doi: 10.1016/j.apsusc.2013.02.086.

[36] D. G. Hepworth, R. N. Hobson, D. M. Bruce, and J. W. Farrent, "The use of unretted hemp fibre in composite manufacture," *Compos Part A Appl Sci Manuf*, vol. 31, no. 11, pp. 1279–1283, Nov. 2000, doi: 10.1016/S1359-835X(00)00098-1.

[37] T. Thamae, S. Aghedo, C. Baillie, and D. Matovic, "Tensile properties of hemp and Agave americana fibres," in *Handbook of Tensile Properties of Textile and Technical Fibres*, Elsevier, 2009, pp. 73–99. doi: 10.1533/9781845696801.1.73.

[38] M. Z. H. Kazmi, A. Karmakar, V. K. Michaelis, and F. J. Williams, "Separation of cellulose/hemicellulose from lignin in white pine sawdust using boron trihalide reagents," *Tetrahedron*, vol. 75, no. 11, pp. 1465–1470, Mar. 2019, doi: 10.1016/j.tet.2019.02.009.

[39] A. Stamboulis, C. A. Baillie, and T. Peijs, "Effects of environmental conditions on mechanical and physical properties of flax fibers," *Compos Part A Appl Sci Manuf*, vol. 32, no. 8, pp. 1105–1115, Aug. 2001, doi: 10.1016/S1359-835X(01)00032-X.

[40] E. A. Agustiany *et al.*, "Recent developments in lignin modification and its application in lignin-based green composites: A review," *Polym Compos*, vol. 43, no. 8, pp. 4848–4865, Aug. 2022, doi: 10.1002/pc.26824.

[41] L. Mohammed, M. N. M. Ansari, G. Pua, M. Jawaid, and M. S. Islam, "A Review on Natural Fiber Reinforced Polymer Composite and Its Applications," *Int J Polym Sci*, vol. 2015, pp. 1–15, 2015, doi: 10.1155/2015/243947.

[42] K. L. Pickering, M. G. A. Efendy, and T. M. Le, "A review of recent developments in natural fibre composites and their mechanical performance," *Compos Part A Appl Sci Manuf*, vol. 83, pp. 98–112, Apr. 2016, doi: 10.1016/j.compositesa.2015.08.038.

[43] J. P. Manaia, A. T. Manaia, and L. Rodriges, “Industrial Hemp Fibers: An Overview,” *Fibers*, vol. 7, no. 12, p. 106, Dec. 2019, doi: 10.3390/fib7120106.

[44] J. P. Manaia, F. A. Pires, A. M. P. de Jesus, and S. Wu, “Yield behaviour of high-density polyethylene: Experimental and numerical characterization,” *Eng Fail Anal*, vol. 97, pp. 331–353, Mar. 2019, doi: 10.1016/j.engfailanal.2019.01.001.

[45] A. Shahzad, “Hemp fiber and its composites – a review,” *J Compos Mater*, vol. 46, no. 8, pp. 973–986, Apr. 2012, doi: 10.1177/0021998311413623.

[46] M. Sain, P. Suhara, S. Law, and A. Bouilloux, “Interface Modification and Mechanical Properties of Natural Fiber-Polyolefin Composite Products,” *Journal of Reinforced Plastics and Composites*, vol. 24, no. 2, pp. 121–130, Jan. 2005, doi: 10.1177/0731684405041717.

[47] G. Koronis, A. Silva, and M. Fontul, “Green composites: A review of adequate materials for automotive applications,” *Compos B Eng*, vol. 44, no. 1, pp. 120–127, Jan. 2013, doi: 10.1016/j.compositesb.2012.07.004.

[48] X. Peng, M. Fan, J. Hartley, and M. Al-Zubaidy, “Properties of natural fiber composites made by pultrusion process,” *J Compos Mater*, vol. 46, no. 2, pp. 237–246, Jan. 2012, doi: 10.1177/0021998311410474.

[49] S.-L. Bai, G.-T. Wang, J.-M. Hiver, and C. G’Sell, “Microstructures and mechanical properties of polypropylene/polyamide 6/polyethelene-octene elastomer blends,” *Polymer (Guildf)*, vol. 45, no. 9, pp. 3063–3071, Apr. 2004, doi: 10.1016/j.polymer.2004.02.070.

[50] Adrian Marius Tomuta, “New and improved thermosets based on epoxy resins and dendritic polyesters,” Doctoral dissertation, Universitat Rovira i Virgili, 2013.

[51] S.R. Sandler W. K, *Chemistry and Technology of Epoxy Resins*, 1st edition. Springer-Science Business Media, 1993.

[52] D. B. Dittenber and H. V. S. GangaRao, “Critical review of recent publications on use of natural composites in infrastructure,” *Compos Part A Appl Sci Manuf*, vol. 43, no. 8, pp. 1419–1429, Aug. 2012, doi: 10.1016/j.compositesa.2011.11.019.

[53] B. Middleton, “Composites: Manufacture and Application,” in *Design and Manufacture of Plastic Components for Multifunctionality*, Elsevier, 2016, pp. 53–101. doi: 10.1016/B978-0-323-34061-8.00003-X.

[54] D. W. Radford, “3.14 Development of Composite Chassis for Motorsports,” in *Comprehensive Composite Materials II*, Elsevier, 2018, pp. 350–419. doi: 10.1016/B978-0-12-803581-8.10351-0.

[55] M. Quanjin *et al.*, "Design of portable 3-axis filament winding machine with inexpensive control system," *Journal of Mechanical Engineering and Sciences*, vol. 12, no. 1, pp. 3479–3493, Mar. 2018, doi: 10.15282/jmes.12.1.2018.15.0309.

[56] H.-C. Wu and C. D. Eamon, "Provisions for installation, quality control, and maintenance," in *Strengthening of Concrete Structures using Fiber Reinforced Polymers (FRP)*, Elsevier, 2017, pp. 143–189. doi: 10.1016/B978-0-08-100636-8.00005-3.

[57] D. Dai and M. Fan, "Wood fibres as reinforcements in natural fibre composites: structure, properties, processing and applications," in *Natural Fibre Composites*, Elsevier, 2014, pp. 3–65. doi: 10.1533/9780857099228.1.3.

[58] M. O. W. Richardson and Z. Y. Zhang, "Experimental investigation and flow visualisation of the resin transfer mould filling process for non-woven hemp reinforced phenolic composites," *Compos Part A Appl Sci Manuf*, vol. 31, no. 12, pp. 1303–1310, Dec. 2000, doi: 10.1016/S1359-835X(00)00008-7.

[59] J. Summerscales and T. J. Searle, "Low-pressure (vacuum infusion) techniques for moulding large composite structures," *Proceedings of the Institution of Mechanical Engineers, Part L: Journal of Materials: Design and Applications*, vol. 219, no. 1, pp. 45–58, Jan. 2005, doi: 10.1243/146442005X10238.

[60] D. Bender, J. Schuster, and D. Heider, "Flow rate control during vacuum-assisted resin transfer molding (VARTM) processing," *Compos Sci Technol*, vol. 66, no. 13, pp. 2265–2271, Oct. 2006, doi: 10.1016/j.compscitech.2005.12.008.

[61] J. N. Reddy, *Mechanics of Laminated Composite Plates and Shells: Theory and Analysis*, 2nd Edition. CRC Press, 2003. doi: 10.1201/b12409.

[62] Adel S. Saada, *Elasticity Theory and Applications*. Pergamon Press Inc., 1974.

[63] S. Maiti, M. R. Islam, M. A. Uddin, S. Afroj, S. J. Eichhorn, and N. Karim, "Sustainable Fiber-Reinforced Composites: A Review," *Adv Sustain Syst*, vol. 6, no. 11, Nov. 2022, doi: 10.1002/adsu.202200258.

[64] D. K. Rajak, P. H. Wagh, and E. Linul, "Manufacturing Technologies of Carbon/Glass Fiber-Reinforced Polymer Composites and Their Properties: A Review," *Polymers (Basel)*, vol. 13, no. 21, p. 3721, Oct. 2021, doi: 10.3390/polym13213721.

[65] P. F. Chu, S. Iwasawa, P. L. Schell, and C. Y. Lin, "Carbon fiber versus glass fiber reinforcements: A novel, true comparison in thermoplastics," *Polym Compos*, vol. 42, no. 11, pp. 6173–6181, Nov. 2021, doi: 10.1002/PC.26294.

[66] J. Summerscales, N. P. J. Dissanayake, A. S. Virk, and W. Hall, “A review of bast fibres and their composites. Part 1 – Fibres as reinforcements,” *Compos Part A Appl Sci Manuf*, vol. 41, no. 10, pp. 1329–1335, Oct. 2010, doi: 10.1016/j.compositesa.2010.06.001.

[67] L. Yan, N. Chouw, and K. Jayaraman, “Flax fibre and its composites – A review,” *Compos B Eng*, vol. 56, pp. 296–317, Jan. 2014, doi: 10.1016/j.compositesb.2013.08.014.

[68] F. H. M. M. Costa and J. R. M. D’Almeida, “Effect of Water Absorption on the Mechanical Properties of Sisal and Jute Fiber Composites,” *Polym Plast Technol Eng*, vol. 38, no. 5, pp. 1081–1094, Nov. 1999, doi: 10.1080/03602559909351632.

[69] M. R. Bambach, “Compression strength of natural fibre composite plates and sections of flax, jute and hemp,” *Thin-Walled Structures*, vol. 119, pp. 103–113, Oct. 2017, doi: 10.1016/j.tws.2017.05.034.

[70] T. Prade, S.-E. Svensson, A. Andersson, and J. E. Mattsson, “Biomass and energy yield of industrial hemp grown for biogas and solid fuel,” *Biomass Bioenergy*, vol. 35, no. 7, pp. 3040–3049, Jul. 2011, doi: 10.1016/j.biombioe.2011.04.006.

[71] F. Iucolano, L. Boccarusso, and A. Langella, “Hemp as eco-friendly substitute of glass fibres for gypsum reinforcement: Impact and flexural behaviour,” *Compos B Eng*, vol. 175, p. 107073, Oct. 2019, doi: 10.1016/j.compositesb.2019.107073.

[72] L. Boccarusso, L. Carrino, M. Durante, A. Formisano, A. Langella, and F. Memola Capece Minutolo, “Hemp fabric/epoxy composites manufactured by infusion process: Improvement of fire properties promoted by ammonium polyphosphate,” *Compos B Eng*, vol. 89, pp. 117–126, Mar. 2016, doi: 10.1016/j.compositesb.2015.10.045.

[73] F. Pinto, L. Boccarusso, D. De Fazio, S. Cuomo, M. Durante, and M. Meo, “Carbon/hemp bio-hybrid composites: Effects of the stacking sequence on flexural, damping and impact properties,” *Compos Struct*, vol. 242, p. 112148, Jun. 2020, doi: 10.1016/j.compstruct.2020.112148.

[74] S. Uppalapati, J. Bensam Raj, N. Natarajan, and M. A. Khan, “Development and assessment on hemp–carbon–basalt fibre base hybrid composite with organic fillers for structural applications,” *International Journal of Polymer Analysis and Characterization*, vol. 28, no. 4, pp. 383–395, May 2023, doi: 10.1080/1023666X.2023.2221483.

[75] S. S. Pulleti and S. B. Singh, “Development and characterization of hemp/carbon and hemp/glass hybrid and novel functionally graded hybrid composites for structural

applications," *Polym Compos*, vol. 45, no. 12, pp. 11178–11199, Aug. 2024, doi: 10.1002/pc.28540.

[76] K. Inthavong, A. P. Mouritz, J. Dong, and J. Y. Tu, "Inhalation and deposition of carbon and glass composite fibre in the respiratory airway," *J Aerosol Sci*, vol. 65, pp. 58–68, Nov. 2013, doi: 10.1016/j.jaerosci.2013.07.003.

[77] F. Quadrini, D. Bellisario, and L. Santo, "Molding articles made of 100% recycled fiberglass," *J Compos Mater*, vol. 50, no. 21, pp. 2959–2969, Sep. 2016, doi: 10.1177/0021998315615199.

[78] M. Ramesh, C. Deepa, G. R. Arpitha, and V. Gopinath, "Effect of hybridization on properties of hemp-carbon fibre-reinforced hybrid polymer composites using experimental and finite element analysis," *World Journal of Engineering*, vol. 16, no. 2, pp. 248–259, Apr. 2019, doi: 10.1108/WJE-04-2018-0125.

[79] J. Pach, N. Frączek, and J. Kaczmar, "The Effects of Hybridisation of Composites Consisting of Aramid, Carbon, and Hemp Fibres in a Quasi-Static Penetration Test," *Materials*, vol. 13, no. 20, p. 4686, Oct. 2020, doi: 10.3390/ma13204686.

[80] N. Shah, J. Fehrenbach, and C. A. Ulven, "Hybridization of Hemp Fiber and Recycled-Carbon Fiber in Polypropylene Composites," *Sustainability*, vol. 11, no. 11, p. 3163, Jun. 2019, doi: 10.3390/su11113163.

[81] J. Sangilimuthukumar *et al.*, "Quasi-static Indentation Behavior of Kevlar-Hemp and Kevlar-PALF Composites: Influence of Weaving Architecture and Intra-ply Hybridization," *Applied Composite Materials*, vol. 30, no. 3, pp. 937–953, Jun. 2023, doi: 10.1007/s10443-023-10124-w.

[82] S. Jeyaguru *et al.*, "Effect of various weaving architectures on mechanical, vibration and acoustic behavior of Kevlar-Hemp intra-ply hybrid composites," *Compos Part A Appl Sci Manuf*, vol. 176, p. 107845, Jan. 2024, doi: 10.1016/j.compositesa.2023.107845.

[83] A. Ghiaskar and M. D. Nouri, "Numerical and experimental investigation of impact strength and fracture mechanism of Kevlar and Hemp elastomeric thin biocomposite laminate under high-velocity impact: A comparative study," *Mater Today Commun*, vol. 37, p. 106935, Dec. 2023, doi: 10.1016/j.mtcomm.2023.106935.

[84] S. Boria, C. Santulli, E. Raponi, F. Sarasini, and J. Tirillò, "Analytical modeling and experimental validation of the low-velocity impact response of hemp and hemp/glass thermoset composites," *J Compos Mater*, vol. 54, no. 3, pp. 409–421, Feb. 2020, doi: 10.1177/0021998319862856.

[85] J. Flynn, A. Amiri, and C. Ulven, "Hybridized carbon and flax fiber composites for tailored performance," *Mater Des*, vol. 102, pp. 21–29, Jul. 2016, doi: 10.1016/j.matdes.2016.03.164.

[86] V. Gopalan *et al.*, "Dynamic Characteristics of Woven Flax/Epoxy Laminated Composite Plate," *Polymers (Basel)*, vol. 13, no. 2, p. 209, Jan. 2021, doi: 10.3390/polym13020209.

[87] L. Mercedes, E. Bernat-Maso, and L. Gil, "Bending and compression performance of full-scale sandwich panels of hemp fabric reinforced cementitious matrix," *Eng Struct*, vol. 275, p. 115241, Jan. 2023, doi: 10.1016/j.engstruct.2022.115241.

[88] A. Etaati, S. A. Mehdizadeh, H. Wang, and S. Pather, "Vibration damping characteristics of short hemp fibre thermoplastic composites," *Journal of Reinforced Plastics and Composites*, vol. 33, no. 4, pp. 330–341, Feb. 2014, doi: 10.1177/0731684413512228.

[89] S. Chinnasamy, K. V. Kowsik, and R. Raviram, "Mechanical and Vibration Properties of Epoxy Composites Reinforced with Sisal, Areca, and Hemp Fibers, Enhanced by Sugarcane Bagasse and Coconut Husk Fillers," *Materials Circular Economy*, vol. 6, no. 1, p. 24, Dec. 2024, doi: 10.1007/s42824-024-00118-9.

[90] M. Mehdi Jalili, S. Yahya Mousavi, and A. S. Pirayeshfar, "Investigating the acoustical properties of carbon fiber-, glass fiber-, and hemp fiber-reinforced polyester composites," *Polym Compos*, vol. 35, no. 11, pp. 2103–2111, Nov. 2014, doi: 10.1002/pc.22872.

[91] M. M. Jalili, S. Y. Mousavi, and A. S. Pirayeshfar, "Flexural free vibration as a non-destructive test for evaluation of viscoelastic properties of polymeric composites in bending direction," *Iranian Polymer Journal*, vol. 23, no. 5, pp. 327–333, May 2014, doi: 10.1007/s13726-014-0227-x.

[92] Q. J. Singh C and G. Rajamurugan, "Vibration and tribological behaviour of flax/wire mesh/hemp composite reinforced with WCFC particles," *J Manuf Process*, vol. 77, pp. 525–538, May 2022, doi: 10.1016/j.jmapro.2022.03.036.

[93] J. Zhang *et al.*, "Effect of natural fibre reinforcement on the sound and vibration damping properties of bio-composites compression moulded by nonwoven mats," *Composites Communications*, vol. 13, pp. 12–17, Jun. 2019, doi: 10.1016/j.coco.2019.02.002.

[94] L. Di Landro and W. Lorenzi, "Mechanical Properties and Dynamic Mechanical Analysis of Thermoplastic-Natural Fiber/Glass Reinforced Composites," *Macromol Symp*, vol. 286, no. 1, pp. 145–155, Nov. 2009, doi: 10.1002/masy.200951218.

[95] S. Chakraborty, N. H. Padmaraj, T. R. I V, and S. Hegde, “Effect of fibre treatment and moisture content on the vibration and acoustic properties of the basalt/hemp hybrid composites,” *Mater Res Express*, vol. 11, no. 3, p. 035101, Mar. 2024, doi: 10.1088/2053-1591/ad2f7f.

[96] H. Hadiji *et al.*, “Damping analysis of nonwoven natural fibre-reinforced polypropylene composites used in automotive interior parts,” *Polym Test*, vol. 89, p. 106692, Sep. 2020, doi: 10.1016/j.polymertesting.2020.106692.

[97] S. P. Singh, A. Dutt, and C. K. Hirwani, “Mechanical, Modal and Harmonic Behavior Analysis of Jute and Hemp Fiber Reinforced Polymer Composite,” *Journal of Natural Fibers*, vol. 20, no. 1, Apr. 2023, doi: 10.1080/15440478.2022.2140328.

[98] R. El Alaoui, H. Mounir, A. El Marjani, and B. El Mostapha, “Investigation and Analysis of Static and Dynamic Behaviour of a New Natural Composite Material of a Wind Turbine Blade Using the Finite Element Method,” 2018.

[99] P. P. Borah, S. Kashyap, S. Kirtania, and S. Banerjee, “Finite element and numerical analysis for structural responses of natural fibre-based epoxy composites,” *International Journal on Interactive Design and Manufacturing (IJIDeM)*, vol. 18, no. 4, pp. 1955–1967, May 2024, doi: 10.1007/s12008-022-00915-z.

[100] S. P. Singh, A. Dutt, and C. K. Hirwani, “Experimental and numerical analysis of different natural fiber polymer composite,” *Materials and Manufacturing Processes*, vol. 38, no. 3, pp. 322–332, Feb. 2023, doi: 10.1080/10426914.2022.2136379.

[101] R. Bellman, B. G. Kashef, and J. Casti, “Differential quadrature: A technique for the rapid solution of nonlinear partial differential equations,” *J Comput Phys*, vol. 10, no. 1, pp. 40–52, Aug. 1972, doi: 10.1016/0021-9991(72)90089-7.

[102] C. Shu, *Differential Quadrature and Its Application in Engineering*, 1st Edition. Springer London, 2000. doi: 10.1007/978-1-4471-0407-0.

[103] A. Alibeigloo and M. Shakeri, “Elasticity solution for static analysis of laminated cylindrical panel using differential quadrature method,” *Eng Struct*, vol. 31, no. 1, pp. 260–267, Jan. 2009, doi: 10.1016/j.engstruct.2008.08.012.

[104] F. Tornabene, N. Fantuzzi, E. Viola, and E. Carrera, “Static analysis of doubly-curved anisotropic shells and panels using CUF approach, differential geometry and differential quadrature method,” *Compos Struct*, vol. 107, pp. 675–697, Jan. 2014, doi: 10.1016/j.compstruct.2013.08.038.

[105] P. Malekzadeh, “Differential quadrature large amplitude free vibration analysis of laminated skew plates based on FSDT,” *Compos Struct*, vol. 83, no. 2, pp. 189–200, Apr. 2008, doi: 10.1016/j.compstruct.2007.04.007.

[106] S. MARAŞ and A. T. ŞENSOY, “Estimating the effect of certain manufacturing parameters for fiber laminated composites: A validated DQM model integrated with RSM,” *Eng Anal Bound Elem*, vol. 155, pp. 169–181, Oct. 2023, doi: 10.1016/j.enganabound.2023.06.007.

[107] S. Maraş, M. Yaman, M. F. Şansveren, and S. K. Reyhan, “Free Vibration Analysis of Fiber Metal Laminated Straight Beam,” *Open Chem*, vol. 16, no. 1, pp. 944–948, Oct. 2018, doi: 10.1515/chem-2018-0101.

[108] S. MARAŞ and M. YAMAN, “Vibration Behaviors of Antisymmetric Fiber Metal Laminated Composite Plates,” *Gazi Journal of Engineering Sciences*, vol. 9, no. 2, pp. 264–276, Aug. 2023, doi: 10.30855/gmbd.0705069.

[109] A. Heshmati, R.-A. Jafari-Talookolaei, P. S. Valvo, and M. Saadatmorad, “Free and forced vibration analysis of laminated composite beams with through-the-width delamination by considering the in-plane and out-of-plane deformations,” *Mechanics of Advanced Materials and Structures*, vol. 31, no. 23, pp. 5953–5972, Dec. 2024, doi: 10.1080/15376494.2023.2222399.

[110] M. S. Qatu, “IN-PLANE VIBRATION OF SLIGHTLY CURVED LAMINATED COMPOSITE BEAMS,” *J Sound Vib*, vol. 159, no. 2, pp. 327–338, 1991.

[111] C. S. HUANG, Y. P. TSENG, A. W. LEISSA, and K. Y. NIEH, “AN EXACT SOLUTION FOR IN-PLANE VIBRATIONS OF AN ARCH HAVING VARIABLE CURVATURE AND CROSS SECTION,” *Int. J. Mech. Sci.*, vol. 40, no. 11, pp. 1159–1173, 1998.

[112] F. KADIOGLU and C. IYIDOGAN, “Free Vibration of Laminated Composite Curved BeamsUsing Mixed Finite Element Formulation,” *Science and Engineering of Composite Materials*, vol. 16, no. 4, pp. 247–258, 2009.

[113] X. Li and C. Guedes Soares, “Spectral finite element analysis of in-plane free vibration of laminated composite shallow arches,” *Compos Struct*, vol. 132, pp. 484–494, Nov. 2015, doi: 10.1016/j.compstruct.2015.05.060.

[114] Q. Lü and C. F. Lü, “Exact two-dimensional solutions for in-plane natural frequencies of laminated circular arches,” *J Sound Vib*, vol. 318, no. 4–5, pp. 982–990, Dec. 2008, doi: 10.1016/j.jsv.2008.05.011.

[115] F. Yang, R. Sedaghati, and E. Esmailzadeh, "Free in-plane vibration of general curved beams using finite element method," *J Sound Vib*, vol. 318, no. 4–5, pp. 850–867, Dec. 2008, doi: 10.1016/j.jsv.2008.04.041.

[116] V. YILDIRIM, "ROTARY INERTIA, AXIAL AND SHEAR DEFORMATION EFFECTS ON THE IN-PLANE NATURAL FREQUENCIES OF SYMMETRIC CROSS-PLY LAMINATED CIRCULAR ARCHES," *J Sound Vib*, vol. 224, no. 4, pp. 575–589, Jul. 1999, doi: 10.1006/jsvi.1999.2201.

[117] Y.P. Tseng, C.S. Huang, and M.S. Kao, "In-plane vibration of laminated curved beams with variable curvature by dynamic stiffness analysis," *Compos Struct*, vol. 50, no. 2, pp. 103–114, 2000.

[118] C.-N. Chen, "DQEM analysis of in-plane vibration of curved beam structures," *Advances in Engineering Software*, vol. 36, no. 6, pp. 412–424, Jun. 2005, doi: 10.1016/j.advengsoft.2004.12.006.

[119] P. Malekzadeh, "In-plane Free Vibration Analysis of Laminated Thick Circular Deep Arches," *Journal of Reinforced Plastics and Composites*, vol. 26, no. 18, pp. 1943–1951, Dec. 2007, doi: 10.1177/0731684407081770.

[120] P. Malekzadeh and A. R. Setoodeh, "DQM in-plane free vibration of laminated moderately thick circular deep arches," *Advances in Engineering Software*, vol. 40, no. 9, pp. 798–803, Sep. 2009, doi: 10.1016/j.advengsoft.2009.01.011.

[121] P. Malekzadeh, A. R. Setoodeh, and E. Barmshouri, "A hybrid layerwise and differential quadrature method for in-plane free vibration of laminated thick circular arches," *J Sound Vib*, vol. 315, no. 1–2, pp. 212–225, Aug. 2008, doi: 10.1016/j.jsv.2008.02.005.

[122] K. M. Fard, J. Estiri, and A. Davar, "A new two-dimensional refined higher order theory for in-plane free vibrations of sandwich and composite thick curved beams with flexible cores," *Journal of Sandwich Structures & Materials*, vol. 14, no. 3, pp. 247–280, May 2012, doi: 10.1177/1099636212444746.

[123] A.-T. Luu, N.-I. Kim, and J. Lee, "NURBS-based isogeometric vibration analysis of generally laminated deep curved beams with variable curvature," *Compos Struct*, vol. 119, pp. 150–165, Jan. 2015, doi: 10.1016/j.compstruct.2014.08.014.

[124] M. Hajianmaleki and M. S. Qatu, "Static and vibration analyses of thick, generally laminated deep curved beams with different boundary conditions," *Compos B Eng*, vol. 43, no. 4, pp. 1767–1775, Jun. 2012, doi: 10.1016/j.compositesb.2012.01.019.

[125] F. Yang, R. Sedaghati, and E. Esmailzadeh, “Free in-plane vibration of curved beam structures: A tutorial and the state of the art,” *Journal of Vibration and Control*, vol. 24, no. 12, pp. 2400–2417, Jun. 2018, doi: 10.1177/1077546317728148.

[126] J. Guo, D. Shi, Q. Wang, F. Pang, and Q. Liang, “A domain decomposition approach for static and dynamic analysis of composite laminated curved beam with general elastic restrains,” *Mechanics of Advanced Materials and Structures*, vol. 26, no. 16, pp. 1390–1402, Aug. 2019, doi: 10.1080/15376494.2018.1432810.

[127] Y. Yan, E. Carrera, and A. Pagani, “Free vibration analysis of curved metallic and composite beam structures using a novel variable-kinematic DQ method,” *Mechanics of Advanced Materials and Structures*, vol. 29, no. 25, pp. 3743–3762, Oct. 2022, doi: 10.1080/15376494.2021.1909784.

[128] O. Demir, D. Balkan, R. C. Peker, M. Metin, and A. Arikoglu, “Vibration analysis of curved composite sandwich beams with viscoelastic core by using differential quadrature method,” *Journal of Sandwich Structures & Materials*, vol. 22, no. 3, pp. 743–770, Mar. 2020, doi: 10.1177/1099636218767491.

[129] A. Arikoglu and A. G. Ozturk, “A novel approach for in-plane vibration and damping analysis of arbitrarily curved laminated composite and sandwich beams,” *Compos Struct*, vol. 253, p. 112781, Dec. 2020, doi: 10.1016/j.compstruct.2020.112781.

[130] S. Maraş and M. Yaman, “Free vibration analysis of fiber-metal laminated composite plates using differential, generalized and harmonic quadrature methods: experimental and numerical studies,” *Eng Comput (Swansea)*, vol. 39, no. 6, pp. 2326–2349, Jun. 2022, doi: 10.1108/EC-08-2021-0490.

[131] M. Bacciocchi, M. Eisenberger, N. Fantuzzi, F. Tornabene, and E. Viola, “Vibration analysis of variable thickness plates and shells by the Generalized Differential Quadrature method,” *Compos Struct*, vol. 156, pp. 218–237, Nov. 2016, doi: 10.1016/j.compstruct.2015.12.004.

[132] M. A. De Rosa, N. M. Auciello, and M. Lippiello, “Dynamic stability analysis and DQM for beams with variable cross-section,” *Mech Res Commun*, vol. 35, no. 3, pp. 187–192, Apr. 2008, doi: 10.1016/j.mechrescom.2007.10.010.

[133] S. A. Eftekhari, “Differential quadrature procedure for in-plane vibration analysis of variable thickness circular arches traversed by a moving point load,” *Appl Math Model*, vol. 40, no. 7–8, pp. 4640–4663, Apr. 2016, doi: 10.1016/j.apm.2015.11.046.

[134] F. Tornabene and E. Viola, “Vibration analysis of spherical structural elements using the GDQ method,” *Computers & Mathematics with Applications*, vol. 53, no. 10, pp. 1538–1560, May 2007, doi: 10.1016/j.camwa.2006.03.039.

[135] S. Süsler, H. Kurtaran, H. S. Türkmen, Z. Kazancı, and V. Lopresto, "An experimentally validated numerical method for investigating the air blast response of basalt composite plates," *Mechanics of Advanced Materials and Structures*, vol. 27, no. 6, pp. 441–454, Mar. 2020, doi: 10.1080/15376494.2018.1478049.

[136] S. Maraş and M. Yaman, "Investigation of dynamic properties of GLARE and CARALL hybrid composites: Numerical and experimental results," *Eng Anal Bound Elem*, vol. 155, pp. 484–499, Oct. 2023, doi: 10.1016/j.enganabound.2023.06.026.

[137] Ö. Civalek, "Nonlinear dynamic response of laminated plates resting on nonlinear elastic foundations by the discrete singular convolution-differential quadrature coupled approaches," *Compos B Eng*, vol. 50, pp. 171–179, Jul. 2013, doi: 10.1016/j.compositesb.2013.01.027.

[138] P. Malekzadeh and A. R. Vosoughi, "Large Amplitude Free Vibration Analysis of Composite Plates with Rotationally Restrained Edges using DQM," *Journal of Reinforced Plastics and Composites*, vol. 27, no. 4, pp. 409–430, Mar. 2008, doi: 10.1177/0731684407084123.

[139] M. K. Singha and M. Ganapathi, "Large amplitude free flexural vibrations of laminated composite skew plates," *Int J Non Linear Mech*, vol. 39, no. 10, pp. 1709–1720, Dec. 2004, doi: 10.1016/j.ijnonlinmec.2004.04.003.

[140] M. K. Singha and R. Daripa, "Nonlinear vibration of symmetrically laminated composite skew plates by finite element method," *Int J Non Linear Mech*, vol. 42, no. 9, pp. 1144–1152, Nov. 2007, doi: 10.1016/j.ijnonlinmec.2007.08.001.

[141] A. K. Onkar and D. Yadav, "Non-linear free vibration of laminated composite plate with random material properties," *J Sound Vib*, vol. 272, no. 3–5, pp. 627–641, May 2004, doi: 10.1016/S0022-460X(03)00387-0.

[142] Y. Y. Lee, H. Y. Sun, and J. N. Reddy, "Non-linear finite element modal approach for the large amplitude free vibration of symmetric and unsymmetric composite plates," *Int J Numer Methods Eng*, vol. 65, no. 1, pp. 45–61, Jan. 2006, doi: 10.1002/nme.1448.

[143] A. Shooshtari and S. Razavi, "A closed form solution for linear and nonlinear free vibrations of composite and fiber metal laminated rectangular plates," *Compos Struct*, vol. 92, no. 11, pp. 2663–2675, Oct. 2010, doi: 10.1016/j.compstruct.2010.04.001.

[144] A. Shooshtari and S. Razavi, "Nonlinear free and forced vibrations of anti-symmetric angle-ply hybrid laminated rectangular plates," *J Compos Mater*, vol. 48, no. 9, pp. 1091–1111, Apr. 2014, doi: 10.1177/0021998313482156.

[145] A. Houmat, “Nonlinear free vibration of a composite rectangular specially-orthotropic plate with variable fiber spacing,” *Compos Struct*, vol. 94, no. 10, pp. 3029–3036, Oct. 2012, doi: 10.1016/j.compstruct.2012.05.006.

[146] B. Adhikari and P. Dash, “Geometrically nonlinear free vibration analysis of laminated composite plates: A finite element assessment of a higher order non-polynomial shear deformation theory,” *Mechanics of Advanced Materials and Structures*, vol. 28, no. 2, pp. 200–211, Jan. 2021, doi: 10.1080/15376494.2018.1553259.

[147] S. Lore, S. Sarangan, and B. N. Singh, “Nonlinear free vibration analysis of laminated composite plates and shell panels using non-polynomial higher-order shear deformation theory,” *Mechanics of Advanced Materials and Structures*, vol. 29, no. 26, pp. 5608–5623, Oct. 2022, doi: 10.1080/15376494.2021.1959971.

[148] H. Ku, H. Wang, N. Pattarachaiyakoop, and M. Trada, “A review on the tensile properties of natural fiber reinforced polymer composites,” *Compos B Eng*, vol. 42, no. 4, pp. 856–873, Jun. 2011, doi: 10.1016/j.compositesb.2011.01.010.

[149] “MGS Laminasyon Epoksi Seti L160/H160 HEXION.” Accessed: Oct. 22, 2024. [Online]. Available: https://www.kompozitshop.com/mgs-laminasyon-epoksi-seti-l160h160

[150] G. Belingardi, M. P. Cavatorta, and D. Salvatore Paolino, “Repeated impact response of hand lay-up and vacuum infusion thick glass reinforced laminates,” *Int J Impact Eng*, vol. 35, no. 7, pp. 609–619, Jul. 2008, doi: 10.1016/j.ijimpeng.2007.02.005.

[151] “Standard Test Method for Tensile Properties of Polymer Matrix Composite Materials 1.” doi: 10.1520/D3039_D3039M-1.

[152] A. Chopra, *Dynamics of Structures, Global Edition*, 4th ed. Harlow: Pearson Education, 2015.

[153] R. Bellman and J. Casti, “Differential quadrature and long-term integration,” *J Math Anal Appl*, vol. 34, no. 2, pp. 235–238, May 1971, doi: 10.1016/0022-247X(71)90110-7.

[154] F. Tornabene and M. Bacciocchi, *Anisotropic Doubly-Curved Shells. Higher-Order Strong and Weak Formulations for Arbitrarily Shaped Shell Structures*. Società Editrice Esculapio, 2018. doi: 10.15651/978-88-938-5080-3.

[155] H. Kurtaran, “Large displacement static and transient analysis of functionally graded deep curved beams with generalized differential quadrature method,” *Compos Struct*, vol. 131, pp. 821–831, Nov. 2015, doi: 10.1016/j.compstruct.2015.06.024.

[156] M. S. Qatu, “Theories and analyses of thin and moderately thick laminated composite curved beams,” *Int J Solids Struct*, vol. 30, no. 20, pp. 2743–2756, 1993, doi: 10.1016/0020-7683(93)90152-W.

[157] T. Ye, G. Jin, X. Ye, and X. Wang, “A series solution for the vibrations of composite laminated deep curved beams with general boundaries,” *Compos Struct*, vol. 127, pp. 450–465, Sep. 2015, doi: 10.1016/j.compstruct.2015.03.020.

[158] T. Sakiyama, H. Matsuda, and C. Morita, “FREE VIBRATION ANALYSIS OF SANDWICH ARCHES WITH ELASTIC OR VISCOELASTIC CORE AND VARIOUS KINDS OF AXIS-SHAPE AND BOUNDARY CONDITIONS,” *J Sound Vib*, vol. 203, no. 3, pp. 505–522, Jun. 1997, doi: 10.1006/jsvi.1996.0900.

[159] L. Boccarusso *et al.*, “Design, Manufacturing, and Characterization of Hybrid Carbon/Hemp Sandwich Panels,” *J Mater Eng Perform*, vol. 31, no. 1, pp. 769–785, Jan. 2022, doi: 10.1007/s11665-021-06186-1.

[160] R. Murugan, R. Ramesh, and K. Padmanabhan, “Investigation of the mechanical behavior and vibration characteristics of thin walled glass/carbon hybrid composite beams under a fixed-free boundary condition,” *Mechanics of Advanced Materials and Structures*, vol. 23, no. 8, pp. 909–916, Aug. 2016, doi: 10.1080/15376494.2015.1056394.

[161] B. HARRAS, R. BENAMAR, and R. G. WHITE, “EXPERIMENTAL AND THEORETICAL INVESTIGATION OF THE LINEAR AND NON-LINEAR DYNAMIC BEHAVIOUR OF A GLARE 3 HYBRID COMPOSITE PANEL,” *J Sound Vib*, vol. 252, no. 2, pp. 281–315, Apr. 2002, doi: 10.1006/jsvi.2001.3962.

[162] M. Sathyamoorthy, “Non-linear vibration of rectangular plates,” *J Sound Vib*, vol. 58, no. 2, pp. 301–304, May 1978, doi: 10.1016/S0022-460X(78)80084-4.

[163] S. L. Lau, Y. K. Cheung, and S. Y. Wu, “Nonlinear Vibration of Thin Elastic Plates, Part 1: Generalized Incremental Hamilton’s Principle and Element Formulation,” *J Appl Mech*, vol. 51, no. 4, pp. 837–844, Dec. 1984, doi: 10.1115/1.3167734.

[164] R. Benamar, M. M. K. Bennouna, and R. G. White, “The Effects of Large Vibration Amplitudes on the Mode Shapes and Natural Frequencies of Thin Elastic Structures, Part II: Fully Clamped Rectangular Isotropic Plates,” *J Sound Vib*, vol. 164, no. 2, pp. 295–316, Jun. 1993, doi: 10.1006/jsvi.1993.1215.

[165] W. Han and M. Petyt, “Geometrically nonlinear vibration analysis of thin, rectangular plates using the hierarchical finite element method—II: 1st mode of laminated plates and higher modes of isotropic and laminated plates,” *Comput Struct*, vol. 63, no. 2, pp. 309–318, Apr. 1997, doi: 10.1016/S0045-7949(96)00346-X.

[166] K. N. Saha, D. Misra, G. Pohit, and S. Ghosal, "Large Amplitude Free Vibration Study of Square Plates under Different Boundary Conditions Through a Static Analysis," *Journal of Vibration and Control*, vol. 10, no. 7, pp. 1009–1028, Jul. 2004, doi: 10.1177/1077546304038101.

[167] G. Singh, K. Kanaka Raju, G. Venkateswara Rao, and N. G. R. Iyengar, "Non-linear vibrations of simply supported rectangular cross-ply plates," *J Sound Vib*, vol. 142, no. 2, pp. 213–226, Oct. 1990, doi: 10.1016/0022-460X(90)90553-C.

[168] T. Pirbodaghi, M. Fesanghary, and M. T. Ahmadian, "Non-linear vibration analysis of laminated composite plates resting on non-linear elastic foundations," *J Franklin Inst*, vol. 348, no. 2, pp. 353–368, Mar. 2011, doi: 10.1016/j.jfranklin.2010.12.002.

[169] J. F. Wang, J. P. Yang, S. K. Lai, and W. Zhang, "Stochastic meshless method for nonlinear vibration analysis of composite plate reinforced with carbon fibers," *Aerosp Sci Technol*, vol. 105, p. 105919, Oct. 2020, doi: 10.1016/j.ast.2020.105919.